FACHGEBIET STRÖMUNGSMECHANIK
TECHNISCHE UNIVERSITÄT MÜNCHEN

Direct and large-eddy simulation of flow around a circular cylinder at subcritical Reynolds numbers

Frederic Tremblay

Vollständiger Abdruck der von der Fakultät für Maschinenwesen der Technischen Universität München zur Erlangung des akademischen Grades eines

Doktor-Ingenieurs

genehmigten Dissertation.

Vorsitzender:	Univ. Prof. Dr.-Ing. Th. Sattelmayer
1. Prüfer der Dissertation:	Univ. Prof. Dr.-Ing. habil. R. Friedrich
2. Prüfer der Dissertation:	apl. Prof. Dr.-Ing. habil. H. Wengle, UniBw München

Die Dissertation wurde am 24.09.2001 bei der Technischen Universität München eingereicht und durch die Fakultät für Maschinenwesen am 20.12.2001 angenommen.

Abstract

DNS and LES of flow around a circular cylinder at subcritical Reynolds numbers are performed using a novel immersed boundary technique which allows the computation of flow around arbitrary bodies with cartesian grids. Results for transitional and turbulent flows agree well with experimental and numerical data of other authors, confirming the reliability of the method. New light is shed on the two quasi- statistically stable states of the mean streamwise velocity in the near wake. At high subcritical Reynolds numbers, the crossflow in the wake exhibits unexpectedly high levels of fluctuations, leaving room for extensive further research.

Zusammenfassung

Bei subkritischen Reynoldszahlen sind die Grenzschichten am querangeströmten Kreiszylinder laminar, und der Umschlag zur Turbulenz erfolgt in der abgelösten Scherschicht. Zur Vorhersage solcher Strömungen werden die inkompressiblen Navier-Stokes (NS)-Gleichungen, bzw. die tiefpass-gefilterten NS-Gleichungen direkt numerisch integriert. Dies geschieht auf kartesischen Gittern durch spezielle Randbehandlung. Vergleiche mit Messdaten bestätigen die Zuverlässigkeit der Methode. Momentane und statistische Strömungsgrößen werfen neues Licht auf die Struktur der körpernahen, rezirkulierenden Nachlaufströmung. Sie ist u.a. durch sehr hohe Quergeschwindigkeiten, vergleichbar der Anströmgeschwindigkeit, gekennzeichnet.

Acknowledgement

I would like to express my gratitude to the people who contributed over the last four years in making this work a success. Firstly Prof. Friedrich, my "Doktorvater". This german word illustrates well the role he played: providing many useful comments and acting as a guide along the path of knowledge. My colleagues Michael Manhart, Christophe Brun and Gary Evans also helped me to learn quite a lot during our countless conversations. But overall, their friendship has proven to be the most beneficial thing. Without the excellent technical support of the staff at the LRZ, the computations might still not be finished yet. Financial support is acknowledged in the framework of the EC project Alessia and in the form of a doctoral grant obtained from the FCAR. I also thank my family which, in spite of the long distance between Canada and Germany, always encouraged me. My final acknowledgement goes to my fiancée, Nancy Larochelle. Without her love and support, none of this would have been possible.

Contents

List of Figures

Nomenclature

Roman symbols

B	Blocking array
b_{ij}	Reynolds stress anisotropy tensor
C_D	Drag coefficient
C_{Dyn}	Dynamic approximation of the Smagorinsky constant.
C_L	Lift coefficient
C_p	Pressure coefficient
C_{PB}	Base pressure coefficient
C_S	Smagorinsky constant
D	Diameter of the cylinder
F_D	Drag force
F_L	Lift force
II, III	Second and third invariants of b_{ij}
k	Turbulent kinetic energy
k_Z	Wavenumber
L_{ij}	Leonard term
L_r	Recirculation length
l_{ref}	Characteristic length scale
N_x, N_y, N_z	Number of grid points in the x-, y- and z-direction
$\vec{n}$	Normal unit vector
$\vec{P}$	Position vector
p	Pressure
P_∞	Reference pressure
$\bar{p}$	Mean pressure
p'	Pressure fluctuation
Q	Second invariant of the velocity gradient tensor
$\bar{S}_{ij}$	Filtered strain rate tensor
T_{ij}	Subtest stress tensor
$\vec{u}$	Velocity vector
u, v, w	Velocity in the x-, y- and z-directions
$\bar{u}, \bar{v}, \bar{w}$	Mean velocity components

u', v', w'	Velocity fluctuations
U_∞	Reference velocity
u_{ref}	Characteristic velocity scale
$\bar{u_i}$	Low-pass filtered velocity
$\overline{u_i u_j}$	Reynolds stress tensor
v_K	Kolmogorov velocity scale
v_t	Tangential velocity

Greek symbols

α_p	Interpolation/extrapolation coefficient
γ_{dir}	Weight of direction dir
Δ	Filter width
δ_{99}	Boundary layer thickness
δ_{ij}	Kronecker delta
Δ_P	Pressure difference
Δt	Distance in time
Δx	Distance in space
$\Delta_x, \Delta_y, \Delta_z$	Grid spacing in the x-, y- and z-directions
ϵ_v, ϵ_p	Error in the velocity and the pressure field
η	Kolmogorov length scale
Θ_{sep}	Separation angle
μ	Dynamic viscosity
ν	Kinematic viscosity
ν_T	Turbulent eddy viscosity
ρ	Mass density
τ	Kolmogorov time scale
τ_{ij}	Subgrid scale stress tensor
ϕ_p	Interpolated/extrapolated variable
Ω_{ij}	Rotation tensor
ω_{St}	Strouhal frequency

Abbreviations

CFL	Courant-Friedrichs-Lewy number
CPU	Central processing unit
DNS	Direct numerical simulation
DES	Detached eddy simulation
LES	Large eddy simulation

RANS	Reynolds averaged Navier-Stokes
Re	Reynolds number
RMS	Root mean square
St	Strouhal number
SGS	Subgrid scale

1. Introduction

1.1 Basic concepts

1.1.1 Definition of turbulence

Fluid flows are encountered in many engineering applications. Most of the time, the fluid is in a state called turbulence. A definition of turbulence was tentatively proposed by Lesieur in [22] and reads :

- A turbulent flow is unpredictable, in the sense that a small uncertainty as to its knowledge at a given initial time will amplify so as to render impossible a precise deterministic prediction of its evolution.
- It increases mixing properties when compared to a flow in which only the molecular diffusion processes are present.
- It involves a wide range of spatial and temporal scales.

Let us have a closer look at this definition. Although all fluid flows correspond to fully deterministic phenomena, a particular characteristic of the state called turbulence is its exponential amplification of small perturbations caused by the non-linearity of the governing equations. Predicting a turbulent flow like in the atmosphere, for example, thus requires a perfect knowledge of its detailed state at an initial time. If we chose to consider the flow isolated from its surroundings, perfect knowledge of the conditions prevailing on its boundaries is also required. In the case of the flow in the atmosphere, it means for example that the energy input from the sun would have to be known for all instants. The sun being itself under the influence of its surroundings, we can continue this reasoning until we finally come to the conclusion that for a deterministic prediction of the atmospheric flow, perfect knowledge of the Universe would be required. It is very clear that this is not possible. Although predicting turbulence exactly is hopeless, it doesn't mean that science cannot extract useful information from turbulent flows given all uncertainties. An often cited metaphor is the so-called butterfly effect in

which a butterfly flying in Japan can cause a hurricane to devastate the Carribeans. This is very unlikely to happen in reality. Small perturbations, given enough time to amplify, might render a fully deterministic description in the time domain of turbulence impossible, but they leave mostly unchanged its dominating time and spatial length scales and its statistical description. This demonstrates that even in the presence of small uncertainties, relevant informations to engineering processes can be extracted from our predictions of turbulence.

The enhanced mixing properties of turbulence can easily be observed when pouring cream into a stirred cup of coffee. Proper mixing of chemical reagents is of capital importance for many engineering applications. For example, when fuel is injected into the combustion chamber of an airplane engine, mixing with air occurs and its efficiency determines the efficiency of the combustion process.

The last part of the definition mentions that in turbulent flows, a wide range of spatial and temporal scales is observed. Turbulence, although chaotic, is not a random process, but is organized in coherent structures which vary in size continuously from large to small. In the mean, kinetic energy is transferred from large to small scales by the break-up of the large structures. At the smallest scales, kinetic energy in transformed into heat by viscous dissipation.

1.1.2 Governing equations

The equations that describe the spatial and temporal evolution of a fluid flow have been known for a long time. In the case of a Newtonian fluid, characterized by a linear stress-strain relation and Fourier's heat conduction law they are called the Navier-Stokes equations. These equations consist of conservation laws for mass, momentum and energy. In this thesis, we consider only isothermal and incompressible fluids. Under these conditions, the Navier-Stokes equations are expressed as:

$$\nabla \cdot \vec{u} = 0 \tag{1.1}$$

$$\frac{\partial \vec{u}}{\partial t} + \vec{u} \cdot \nabla \vec{u} = -\frac{1}{\rho} \nabla p + \nu \nabla^2 \vec{u} \tag{1.2}$$

with $\vec{u}$ the velocity vector, ρ the fluid density, p the pressure and ν the kinematic viscosity.

1.1.3 Numerical simulation techniques

Since the governing equations for Newtonian fluid flows are well defined and their validity to describe high Reynolds number continuum flows is no longer a subject of serious debate in the community, one could think that the problem is now solved. Up to now, no mathematical tool can provide an analytical solution to this non-linear system of equations for turbulent flows. We must thus resort to numerical solutions in these cases. This generally means that the exact solution will not be known for all points in time and space, but rather on a set of discrete points that we call a grid and for certain discrete instants in time.

Direct Numerical Simulation

Let us call Δx and Δt the distance between to points in space and time in which the flow evolves. A Direct Numerical Simulation (DNS) is a computation in which Δx and Δt are comparable to the smallest scales present in the flow. Following dimensional analysis, we obtain the following relations for the length scale η, the velocity scale v_K and the time scale τ of the smallest turbulent structures which are known as the Kolmogorov scales :

$$\frac{\eta}{l_{ref}} = Re^{-\frac{3}{4}} \tag{1.3}$$

$$\frac{v_K}{u_{ref}} = Re^{-\frac{1}{4}} \tag{1.4}$$

$$\frac{\tau}{l_{ref}/u_{ref}} = Re^{-\frac{1}{2}} \tag{1.5}$$

with the Reynolds number defined as

$$Re = \frac{l_{ref} u_{ref}}{\nu} \tag{1.6}$$

where l and u are characteristic of the largest length and velocity scales of the flow considered and ν is the kinematic viscosity. From this consideration, it follows that the number of points in space needed for DNS of a turbulent flow is growing at a rate proportional to $Re^{\frac{9}{4}}$ when considering the three directions. The total number of time steps increases proportionally to $Re^{\frac{1}{2}}$. This makes the cost of performing a simulation increase with a factor of roughly Re^3. Even when using the most powerful computers available today, only modest Reynolds numbers can be attained. Spalart [43] tried to evaluate when it will be possible to achieve a Reynolds number of engineering

interest. By considering a computational power increase by a factor of 5 every 5 years, we will have to wait 80 years before such a flow can be solved as a "Grand Challenge Problem" and some more years before it becomes a routinely performed computation. Some alternatives are thus needed in the mean time.

Large Eddy Simulation

One way to overcome the high cost of DNS is to solve only for the largest scales of the flow and to model the smallest ones. The small scales are thought to behave in a more or less universal way, giving hope for deriving a simple and widely applicable model. Large Eddy Simulation (LES) is based on the definition of a filtering operation : a filtered (or large scale) variable, denoted by an overbar, is defined as

$$\bar{f}(x) = \int f(x)G(x,x')dx' \tag{1.7}$$

where G is a low-pass filter function. As long as turbulent flows are dominated by convective phenomena and are not influenced by the input of external energy at high frequency and low wavenumber (e.g. wall oscillations at high frequency), a spatial filter is sufficient to remove also the small temporal scales. If the filtering operation (1.7) is applied to the governing equations, and filtering commutes with differentiation, one obtains the filtered equations of motion in the following form:

$$\frac{\partial \bar{u}_i}{\partial x_i} = 0 \tag{1.8}$$

$$\frac{\partial \bar{u}_i}{\partial t} + \frac{\partial}{\partial x_j}(\bar{u}_i\bar{u}_j) = -\frac{1}{\rho}\frac{\partial \bar{p}}{\partial x_i} - \frac{\partial \tau_{ij}}{\partial x_j} + \nu\frac{\partial^2 \bar{u}_i}{\partial x_j \partial x_j} \tag{1.9}$$

The effect of the small scales appears through a subgrid scale (SGS) stress term

$$\tau_{ij} = \overline{u_i u_j} - \bar{u}_i\bar{u}_j \tag{1.10}$$

that must be modeled. Although much cheaper than DNS, large eddy simulations still require an important number of grid points and time steps and are thus limited to moderate Reynolds numbers. SGS modeling is the subject of extensive research in the turbulence community. A popular SGS model was proposed by Smagorinsky [42]. It takes the following form :

$$\tau_{ij} = -2\nu_T \bar{S}_{ij} + \frac{1}{3}\tau_{kk}\delta_{ij} \tag{1.11}$$

where ν_T is the eddy viscosity and $\bar{S_{ij}}$ is the filtered strain rate

$$\bar{S_{ij}} = \frac{1}{2}(\frac{\partial \bar{u_i}}{\partial x_j} + \frac{\partial \bar{u_j}}{\partial x_i}) \tag{1.12}$$

The value of ν_T is defined as:

$$\nu_T = C_s \Delta^2 |\overline{S}| \tag{1.13}$$

where $|\overline{S}| = (2S_{kl}S_{kl})^{1/2}$ and Δ is a filter width, usually related to the underlying grid. In our computations, we used $\Delta = (\Delta_x \Delta_y \Delta_z)^{1/3}$ with Δ_x, Δ_y and Δ_z the grid spacings in the x, y and z directions respectively. We set $C_s = 0.1$. Eddy viscosity based models assume that in the mean, turbulence dissipates energy through a cascade process and thus acts like additional viscosity. It is well known that the instantaneous cascade of energy is not a one-way process and that locally in time and space, backscatter effects occur which transfer energy from small to large scales. Although considerable efforts have been made to design more realistic SGS models, none has proved more resilient than the Smagorinsky model. Its low computational cost and beneficial properties of numerical stability are certainly partly responsible for its success. The fundamental challenge of SGS modeling is to provide information concerning the unresolved scales, which by definition is not contained in the resolved scales. However, the most important interactions between resolved and subgrid scales occur near the cutoff and a good estimate can be obtained from the smallest resolved scales.

Germano [13] proposed a technique to adjust locally in time and space the constant C_s found in the Smagorinsky model. Dynamic determination of the constant has proved beneficial by allowing the model to be more sensitive to the state of the flow. Better predictions can be obtained in regions of transition and re-laminarization for example. Better behavior in the near-wall region is also achieved. The starting point of the dynamic procedure is the following identity :

$$L_{ij} = T_{ij} - \hat{\tau_{ij}} \tag{1.14}$$

which provides a relation among the resolved turbulent stresses $L_{ij} = \widehat{\overline{u_i u_j}} - \hat{\bar{u}}_i \hat{\bar{u}}_j$. It is called the Leonard term and can be used to compute the subgrid scale stresses τ_{ij} from the subtest stresses T_{ij} obtained by applying an explicit test-filter to the Navier-Stokes equations. The hat is used for test-filtered variables. In our computation using the dynamic procedure, we applied a top-hat test-filter at twice the mesh size in the homogeneous y-direction. By using equation (1.11) and the test filter,

$$\hat{\tau_{ij}} = -2(C_{Dyn}\Delta^2 |\overline{S}| \bar{S_{ij}})\hat{} + \frac{1}{3}\hat{\tau_{kk}}\delta_{ij} \tag{1.15}$$

$$T_{ij} = -2C_{Dyn}\hat{\Delta}^2|\hat{\overline{S}}|\hat{\bar{S}}_{ij} + \frac{1}{3}T_{kk}\delta_{ij} \tag{1.16}$$

The operation $(....)\hat{}$ denotes a filtering procedure applied to the whole expression. Forming the expression

$$L_{ij} - \frac{1}{3}L_{kk}\delta_{ij} = -2C_{Dyn}\hat{\Delta}^2|\hat{\overline{S}}|\hat{\bar{S}}_{ij} + 2(C_{Dyn}\Delta^2|\overline{S}|\bar{S}_{ij})\hat{} \tag{1.17}$$

shows that it cannot directly be used to compute the coefficient C_{Dyn}. It forms an overdetermined system of equations, namely 6 with only one unknown. Lilly [23] proposed to solve this problem by minimizing the square of the error $E_{ij}E_{ij}$ where $E_{ij} = L_{ij} - \frac{1}{3}L_{kk}\delta_{ij} - C_{Dyn}M_{ij}$ and $M_{ij} = 2\hat{\Delta^2}|\hat{\overline{S}}|\hat{\bar{S}}_{ij} - 2(\Delta^2|\overline{S}|\bar{S}_{ij})\hat{}$. This gives a value for the constant :

$$C_{Dyn} = \frac{1}{2}\frac{L_{ij}M_{ij}}{M_{ij}M_{ij}} \tag{1.18}$$

When used this way, the model can provide negative values for C_{Dyn} which account for energy transfer from small to large scales. However, in LES this can cause undesirable instabilities. To overcome this problem, it is preferable to use homogeneous directions of the flow for averaging. The value of the constant then becomes:

$$C_{Dyn} = \frac{1}{2}\frac{< L_{ij}M_{ij} >}{< M_{ij}M_{ij} >} \tag{1.19}$$

where the brackets denote averaging in one or more homogeneous directions. Although the constant now behaves more smoothly in time and space, it can still produce negative values that we clip, i.e. we do not allow the eddy viscosity to become negative. More details about these models are found in Sagaut [39]. Further applications of these models are reported in Friedrich & Rodi [11].

Statistical models

To further reduce the cost of computing turbulent flows, one can analyze them through a statistical approach. Only the average effects are considered, i.e. the wavenumber information about the flow is lost. The flow to be solved can still be unsteady, on a timescale larger than the integral timescale of the turbulence spectrum, but it requires a much lower spatial and temporal resolution. The statistical approach implies the so-called Reynolds decomposition in which the variables are decomposed into mean and fluctuating parts. The Navier-Stokes equations are then ensemble averaged and

one obtains transport equations for the mean quantities which are similar to the Navier-Stokes equations, with the exception that additional terms are present, the Reynolds stresses. The modeling of these terms has been a subject of study for many decades and it is not within the scope of this thesis to give an extensive review of the different strategies employed, the reader can refer to [1] for a good review. We will only mention that the modeling of these terms has proved very challenging since not much information is contained in the resolved flow, and the tremendous loss of information has to be compensated by intelligent models.

Recently, Spalart [43] proposed a new approach to bridge the gap between RANS and LES. The observation that RANS modeling can predict boundary layers with roughly the same accuracy as LES (whatever the SGS model used) but at a much lower cost, led him to propose the DES (Detached Eddy Simulation) technique. In a DES, the attached boundary layers are solved using RANS models while in the separated flow regions LES is used, owing to its clear advantages in such regions over classical RANS methods. DES is a promising concept that could enable full scale engineering applications at high Reynolds number to be computed whithin the ressources available today or in the near future.

1.2 Motivation

The objective of this work is twofold, firstly to derive an efficient numerical method to compute turbulent flows in complex geometries [46]. Most of the codes in use today are written for body-fitted coordinate systems. The feasibility to compute flows over arbitrarily shaped bodies with cartesian grids is very attractive and of great practical importance since typically a cartesian code is anywhere between 10 and 50 times more economical in terms of both CPU time and memory requirements than a code solving the Navier-Stokes equations in curvilinear coordinates [27]. One can thus afford to do a computation with more grid points and still achieve appreciable savings in computational resources. Another important aspect is the complete elimination of the need to produce a body-fitted grid, a task that is not trivial and can consume an important amount of time. In the wake of a bluff body, cartesian cells are highly desirable because of the lower discretization errors compared to those introduced by non-orthogonal and sometimes misaligned cells with respect to the flow direction in body-fitted grids.

The most straightforward method to represent the no-slip condition on an immersed body surface within a cartesian grid is to apply zero velocity at

the cell-face which is the closest to the surface of the body. The difference between the actual and exact body geometry is at most half a cell. This was the method employed by Manhart and Wengle [29] among others. The drawback of this method is that it is only first order accurate. This drawback can be removed by modifying the discretization near the body in order to take into account the cells which are cut. While more accurate schemes were obtained in [56] for two-dimensional flows, the extension of the methods to 3D geometries is not easy because a cell can be cut in many different ways. Other researchers [10],[14],[31], make efforts to preserve the same discretization in all the domain, even including the cells inside the body. Forcing is applied at the location of the body in order to represent its effect on the fluid. A major issue encountered is the interpolation of the forcing over the grid that determines the accuracy of the scheme. Another approach [33] is called diagonal cartesian method on staggered grids. It is quite similar to the present approach, discussed in Chapter 2, where Dirichlet velocity boundary conditions are applied on each cell face located in the immediate vicinity of the body surface. The boundary conditions are applied in such a way that the physical location of the surface and its velocity are best represented. The cells beyond the body surface are excluded from the computation by using a masking array. The discretization remains the same for all cells. A similar approach was derived independently by Gullbrand et al. [15], but in the context of finite differencing on regular grids.

The second objective is to study the flow over a circular cylinder at subcritical Reynolds numbers. The recent publications by several authors of numerical simulations of the cylinder flow at $Re = 3900$ led us to chose this case for the validation of our immersed boundary method, preliminary results are published in [48] and [47]. Moreover, the ongoing controversy about U-shape or V-shape velocity profiles in the near wake made such simulations certainly desirable to further clarify this issue. Another discrepancy observed between numerical and experimental data remains unexplained so far by previous work on this case. A plateau in the mean streamwise velocity in the symmetry plane of the near wake is measured experimentally over a wide range of Reynolds numbers while it is remarkably absent from all the previous numerical simulations. More clarifications are thus needed on this point.

Flow at higher subcritical Reynolds number, namely $Re = 140000$, is also investigated [49] in the light of results obtained using DES [45] and LES [5] techniques. These results raised new questions about the effects of grid refinement. On coarse grids, typical for DES, an important overprediction of the mean recirculating region was noted. In the LES simulations of Breuer [5], "an astonishing outcome was that grid refinement did not automatically

lead to improved results for all quantities, where improvement is defined in this context in the sense of a better agreement with experiments". Given the recent results of flow around a circular cylinder at this regime, some more numerical experiments are highly useful.

1.3 Flow around a circular cylinder

Flow across a circular cylinder is one of the classical flow problems which are not understood in all details even after being subjet of research for several decades. Such flows exhibit many interesting phenomena. They are composed of three fundamental shear flows, namely a boundary layer, separated shear layers and a wake. An excellent review of the flow over cylinders can be found in [55].

1.3.1 Overview of the vortex shedding regimes

A suitable way to characterize the different modes appearing in cylinder flows is to refer to Figure 1.1 which plots the base pressure coefficient (taken at the back of the cylinder) against the Reynolds number. This figure is taken from [55]. The base pressure coefficient is defined as

$$C_{PB} = \frac{P_B - P_\infty}{\frac{1}{2}\rho {U_\infty}^2} \tag{1.20}$$

where P_B is the pressure at the back of the cylinder, P_∞ is the reference pressure, U_∞ the reference velocity and finally ρ is the mass density of the fluid.

Laminar steady regime ($Re < 49$)

This regime extends until point A in Figure 1.1. The wake shows a steady recirculation region composed of a pair of counter-rotating vortices. The recirculation length increases linearly with the Reynolds number, decreasing at the same time the base pressure coefficient.

Laminar vortex shedding

This mode spans in Figure 1.1 from point A up to B. The Reynolds number varies from 49 up to a value of 140-194. The base pressure coefficient shows

a strong deviation from the previous regime. Initially, an instability develops from the downstream region of the bubble. According to Monkewitz [32], the wake becomes absolutely unstable following a local linear parallel stability analysis at $Re = 25$. Different authors observed vortex shedding, however at critical Reynolds number between 30 and 40 only. The characteristic shedding frequency, the Strouhal number, increases with the Reynolds number. The time-averaged recirculation length is reduced and there is a consistent increase in the base pressure coefficient. The upper limit of this regime has a remarkable spreading in the literature (140 to 194). Recent results place the critical Reynolds number where three-dimensionality of the wake sets in, close to 194.

3D wake transition regime

This regime encompasses the region between points B and C of Figure 1.1. It shows two discontinuous changes in the base pressure coefficient as the Reynolds number increases. At the first discontinuity (Re=180-194), formation of pairs of streamwise vortices is observed. The size of this pair of vortices is about 3-4 diameters. This is the so-called mode A instability. At a higher Reynolds number (230-250) the flow gradually transfers its energy from mode A to mode B shedding, which is characterized by the same streamwise vortices, but with a wavelength of about 1 cylinder diameter. In both cases (modes A and B) local shedding phase dislocation along the span is observed.

Increasing disorder in 3D fine scales

From points C-D in Fig1.1, increasing disorder is observed in the fine 3D scales. This appears to produce a longer recirculation length and the consequent decrease of the base pressure coefficient.

Shear layer transition regime (D-E)

Between Reynolds number from 1000 to 200000, the base pressure coefficient increases again, the Strouhal number gradually decreases and the mean recirculation region is reduced. The transition to turbulence of the detached shear layers is caused by a Kelvin-Helmholtz instability, which is principally 2-dimensional [3]. The transition point moves upstream as the Reynolds number is increased. Three-dimensionality of the Kármán vortices appears.

It is important to note that the Reynolds number range up to $Re = 2 \cdot 10^5$ is called the sub-critical range since the flow around the entire periphery of the cylinder is laminar, and the transition to turbulence occurs only in the separated shear layers and in the wake.

Asymmetric reattachment regime (E-G)

In this regime, the base pressure and the drag coefficient are reduced dramatically. This is associated with a reattachment of the boundary layer after the first separation and the final turbulent separation which occurs much further downstream. This produces a reduced width of the wake, hence reduced drag. An interesting phenomenon occurs at point F of Figure 1.1 : the reattachment is observed at only one side of the cylinder, causing a high lift force.

Symmetric reattachment or supercritical regime (G-H)

In this regime, the flow is symmetric with a separation-reattachment bubble on each side of the cylinder. The base pressure coefficient reaches its smallest negative value. The flow is very sensitive to disturbances. Interesting experimental investigations in this region have been made by Schewe [41].

Boundary layer transition regime or post critical regime (H-J)

Following the appearence of turbulence in the wake and the separated free shear layers, the final stage is the transition to turbulence of the boundary layer at the surface of the cylinder itself. The transition point is moved further upstream as the Reynolds number is increased.

1.3.2 Previous numerical experiments

The flow over a circular cylinder has been extensively studied numerically. Two-dimensional computations are routinely carried out in order to validate new numerical schemes and the present study makes no exception to this rule, as will be discussed later. At a Reynolds number larger than around 250, it has long been recognized that two-dimensional computations are no longer capable of providing physically adequate values of the flow

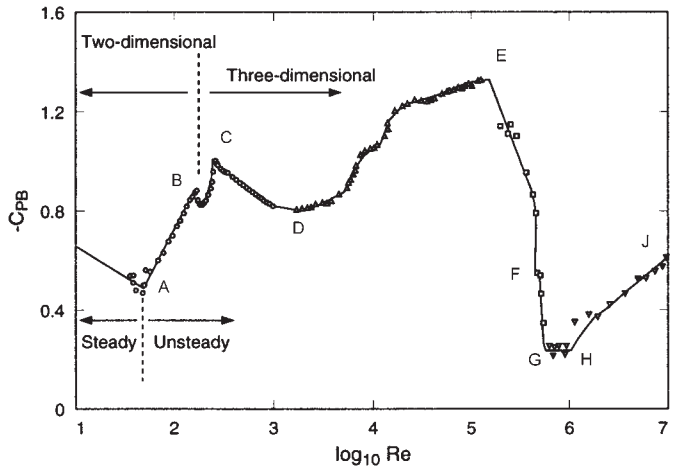

Fig. 1.1: Variation of base suction coefficient ($-C_{PB}$) over a large range of Reynolds numbers. Symbols show experimental data obtained by different researchers. Reproduced from [55]

parameters. As discussed in the previous section, the flow becomes three-dimensional and must be computed as such. Many three-dimensional studies of the cylinder flow have been carried out and for the sake of brevity, only the most important ones will be mentioned. High order spectral elements were used by Thompson et al.[44]. Both the modes A and B of the wake transition regime were detected. Karniadakis and Triantafyllou [19] investigated the flow around a circular cylinder for Reynolds numbers in the range from 225 to 500 using spectral/hp-element methods. The importance of the three-dimensional effects was demonstrated. Since a few years, investigations of the cylinder flow at higher Reynolds number have been performed. Beaudan and Moin [2] computed several LES at $Re = 3900$ with different grid resolutions and SGS models. They used O-type grids and high-order upwind-biased numerical schemes for the simulation of the compressible Navier-Stokes equations. The results were generally in good agreement with the experiments of Lourenco and Shi [24] and those of Ong and Wallace [35], but the Reynolds stresses were under-predicted a few diameters downstream and the one-dimensional power spectra of velocity fluctuations were heavily damped at high wave numbers. Also worth mentioning is the difference observed in the profile of the mean streamwise velocity in the very near-wake region. In their study, Beaudan and Moin did not notice important effects due to the SGS model applied. Mittal and Moin [30] used a second-order conservative central scheme and performed several LES of the flow past a cir-

cular cylinder at $Re = 3900$. In the spanwise direction, a spectral scheme was used. The results were generally in good agreement with those of Beaudan and Moin. Higher levels of the Reynolds stresses were, however, observed in [30] in the region downstream and more energy was contained at the high wavenumbers of the one-dimensional power spectra of the velocity fluctuations. It was concluded that the use of non-dissipative numerical schemes is a need for LES. In the very near-wake region, the results of Mittal and Moin confirmed those of Beaudan and Moin, but differed from the experiment of Lourenco and Shi. LES of the flow past a circular cylinder at $Re = 3900$ were also performed by Breuer [4] and Fröhlich et al.[12] using the same code, LESOCC, based on a finite volume formulation with collocated variable arrangement. The fluxes are discretized using second order central schemes. The study made by Breuer was more extended and included the use of different discretizations, most notably for the convective terms. Computations were performed without a model, with the Smagorinsky model and with the dynamic formulation of the Smagorinsky model. It was again shown that non-dissipative schemes were better for LES. The best results were obtained using the dynamic model in [4], although the influence of the SGS model was weak. In this study, it was reported that doubling the spanwise domain size while keeping the same resolution (thus doubling the number of grid points in this direction) did not affect the solution significantly. Kravchenko and Moin [20] revisited the flow around a circular cylinder at $Re = 3900$ with high order accurate numerical schemes based on B-splines. LES were performed for different grid resolutions with the dynamic SGS model. Their results were in good agreement with the previous studies in the very near wake. In the region downstream of 6 to 10 diameters, Kravchenko and Moin [20] obtained better agreement with the experimental data of Ong and Wallace [35]. Most notably, the fine turbulent scales were more energetic in the region downstream. Ma et al. [26] were able to perform a detailed study of the same case. Both DNS and LES were performed using spectral elements. Excellent agreement with the experimental data was obtained. Two distinct statistically converged states were observed in the very near wake region, corresponding to a U- and V- shape of the mean streamwise velocity profile. All previous studies converged to the first state mentioned above, while the experiment of Lourenco and Shi [24] showed the V-shape of the mean streamwise velocity profile. In Ma et al.[26] it is argued that this difference could be attributed to the extent of the spanwise flow domain chosen in the simulation. They got this idea when one of their computations using a spanwise length of πD converged to the U-shape and another computation using a spanwise length of $2\pi D$ converged to the V-shape. Most previous authors had used πD as the spanwise length, apart from Breuer [4] who obtained very

similar results with a spanwise domain size of πD and $2\pi D$, but on coarse grids.

In the LES studies of the flow around a cylinder at $Re = 3900$, the influence of the SGS model was found to be weak in comparison to the effect of the numerical schemes or the grid used. Higher Reynolds number simulations are needed to study the impact of SGS models. The Reynolds number 140000 appears to be a good candidate due to the availability of experimental data from Cantwell and Coles [7]. Wang et al.[51] performed LES of several bluff body wakes, including the circular cylinder. They used a QUICK scheme and very few grid points (less than 10^6). Although the mean drag coefficient and the Strouhal number were in fair agreement with the data of Cantwell and Coles, the mean velocity profiles and RMS of velocity fluctuations had significant deviations. Fröhlich et al.[12] performed an LES of the cylinder flow at $Re = 140000$ using the Smagorinsky SGS model. Fair agreement was obtained for the drag coefficient, back pressure coefficient, recirculation length, mean streamwise velocity and resolved shear stress in the very near wake region (1 diameter behind the cylinder). No results were presented for the region further downstream. A more detailed investigation was carried out recently by Breuer [5]. The dynamic and Smagorinsky SGS models were used along with different grid resolutions. Again in this study, no clear trend showing the superiority of one SGS model was found. Although in [5] the impact of the SGS model was stronger when compared to the same flow at $Re = 3900$, the effects of the grid spacing were shown to be much more important. Finer resolution did not lead automatically to improved results when compared to the experiment of [7]. This effect was also reported in the DES of Travin et al. [45], but not much confidence can be accorded to their results because of their gross overestimation (2 to 3 times) of the recirculation length reported by Cantwell and Coles [7].

2. Numerical method and validation tests

In this chapter we describe the numerical schemes employed to discretize the Navier-Stokes equations in time and space. The immersed boundary technique implemented in the code MGLET is discussed. Validation tests are conducted on well established flow problems in order to demonstrate the accuracy of the technique.

2.1 Characteristics of the Navier-Stokes code MGLET

We now present the numerical schemes that have been used in the work presented here. The code MGLET, used for all our computations, is a parallel finite volume solver for the incompressible Navier-Stokes equations on staggered cartesian non-equidistant grids. The pressure equation is derived by the projection method of Chorin [8]. The code MGLET has a long tradition in Large-Eddy-Simulation (LES) and Direct Numerical Simulation (DNS) (see eg. Werner and Wengle [53], Manhart and Wengle [29] and Manhart et al. [28]). A method to represent arbitrarily shaped bodies within cartesian grids has been developed and implemented in the code MGLET. It will be presented in details in the next section. The basic discretization schemes are now discussed.

2.1.1 Spatial discretization

The finite volume formulation starts from the integral form of the Navier-Stokes equations for incompressible fluids.

$$\frac{\partial}{\partial t}\int_\Omega \rho u_i d\Omega + \int_S \rho u_i \vec{u}\cdot\vec{n}dS - \int_S (\mu\, grad\, u_i - p)\vec{i_i}\cdot\vec{n}dS = 0 \qquad (2.1)$$

Over one control volume (cell), the volume and surface integrals are approximated numerically by the mid-point rule. The variables, velocities and pressure, are defined on a non-equidistant cartesian grid in staggered arrangement, see Figure 2.1. The control volumes surrounding the individual

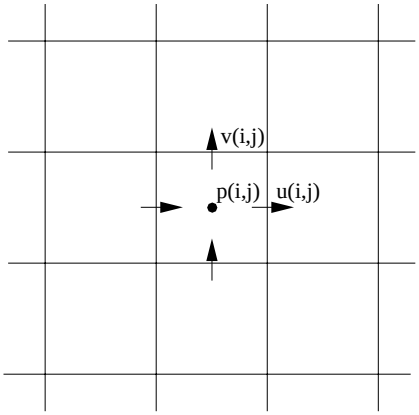

Fig. 2.1: Staggered variable arrangement used in the code MGLET

variables are thus different for each variable. The interpolation required for the convective terms are done by central approximation of second order accuracy. The first derivatives which are used in the diffusive terms are formulated by a second order central approximation.

2.1.2 Time integration

For the time advancement of the momentum equations, an explicit second-order (leap-frog) time step is used which is central with respect to the convective terms.

$$u^{n+1} = u^{n-1} + 2\Delta t \left[C\left(u^{n}\right) + D\left(u^{n-1}\right) - G\left(p^{n+1}\right) \right] \tag{2.2}$$

where C, D and G represent the discrete convection, diffusion and gradient operators in a symbolic way.

The leap-frog time step in combination with central spatial discretizations is unstable for the 1D convection-diffusion equation. Therefore, the diffusive term is taken at time level $n-1$ (Euler time step). Nevertheless, oscillations with a period $2\Delta t$ can still appear and have to be damped by an averaging step every 41 time steps. The advantages of the leap-frog time stepping in comparison to the Adams-Bashforth scheme consist in its efficiency in terms of lower number of operations and its larger domain of stability [52].

2.1.3 Solution of the Poisson equation

The pressure at the new time level p^{n+1} is evaluated by solving the Poisson equation

$$Div\left[G\left(p^{n+1}\right)\right] = \frac{1}{2\Delta t} Div\left(u^*\right) \tag{2.3}$$

where u^* is an intermediate velocity field, calculated by omitting the pressure term in equation 2.2. By applying the velocity correction

$$u^{n+1} = u^* - 2\Delta t G\left(p^{n+1}\right) \tag{2.4}$$

we arrive at the divergence-free velocity field u^{n+1} at the new time level.

The solution of the Poisson equation is done either in a direct way or iteratively when there is only 1 or no homogeneous direction to the flow. All the test cases in the present thesis used the iterative solver. It is based on the algorithm described in Hirt et al. [16]. Using the iteration counter i, the following 3 steps are performed for each control volume within the computational domain.

$$\Delta p^{i+1} = \Omega \frac{1}{2\Delta t} (Div(u^*))^i \cdot \frac{1}{1/\Delta x^2 + 1/\Delta y^2 + 1/\Delta z^2} \tag{2.5}$$

$$u_j{}^{i+1} = u_j{}^i + \Delta p^{i+1} \frac{2\Delta t}{\rho \Delta x_j} \tag{2.6}$$

$$p^{i+1} = p^i + \Delta p^{i+1} \tag{2.7}$$

the initial solution is $u^0 = u^*$ and $p^0 = p^n$. If equations (2.5) to (2.7) are applied to one cell, this cell then becomes divergence-free until its neighbours are treated. After sweeping through all the cells, the overall divergence is reduced and we can procede with the iteration $i + 1$. In order to speed up the convergence, a relaxation factor Ω is introduced in equation (2.5) which has a value of 1.5 to 1.7.

The advantage of this procedure over a Gauss-Seidl solver consists in the simple formulation of the boundary conditions which are required only for the velocities. The boundary conditions for the pressure follow implicitly from the boundary conditions for the velocities. All other properties like convergence and smoothing properties are similar to the Gauss-Seidl algorithm used in conjunction with successive over-relaxation.

2.2 Handling of arbitrarily shaped bodies

The first step is to obtain a representation of the surface of interest. A very versatile way of doing it is by using an unstructured mesh made of triangles. All geometries can be represented this way. Once the body is available, a preprocessing step is done. During this phase a masking array is initialized, which has values of one for cells within the flow and zero for cells belonging to the body. This array is used to block the pressure cells inside the body considered so that they do not contribute to the computation. Boundary conditions have to be applied to the velocity components at the interface between masked and unmasked pressure cells in order to have a well defined problem. In the second phase of the preprocessing step, these boundary conditions are defined as a linear function of the velocities computed within the domain. The coefficients weighting the computed velocities are determined and need no longer to be updated during the run.

2.2.1 Masking the pressure cells

Blocking pressure cells depends on whether the intersection between computational cells and triangles, representing the body surface, satisfies certain conditions which are described below. These conditions have to be simple and unique. We start specifying a triangle by its 3 vertex points (see Figure 2.2) :

$$\vec{P}_1 = (x_1, y_1, z_1)\,, \vec{P}_2 = (x_2, y_2, z_2)\,, \vec{P}_3 = (x_3, y_3, z_3)$$

They define a plane in which a point P lies, that is given by its position vector $\vec{P} = (x, y, z)$ and satisfies:

$$\left(\vec{P} - \vec{P}_1\right) \cdot \left(\left(\vec{P}_2 - \vec{P}_1\right) \times \left(\vec{P}_3 - \vec{P}_1\right)\right) = 0 \tag{2.8}$$

From eq.(2.8), we get the equation of the plane

$$a\,(x - x_1) + b\,(y - y_1) + c\,(z - z_1) = 0 \tag{2.9}$$

where

$$\begin{aligned} a &= (y_2 - y_1)(z_3 - z_1) - (z_2 - z_1)(y_3 - y_1) \\ b &= (z_2 - z_1)(x_3 - x_1) - (x_2 - x_1)(z_3 - z_1) \\ c &= (x_2 - x_1)(y_3 - y_1) - (y_2 - y_1)(x_3 - x_1) \end{aligned}$$

This plane may have up to three intersection points with coordinate lines passing through the cell center C (the pressure point) and these points may lie inside or outside the cell volume, see Figure 2.3. We call D_1, D_2 and D_3 the intersection points with the (x,y,z)-directions, respectively. Their coordinates are :

$$\begin{aligned} D_1 &= \left(\frac{-b(y_c - y_1) - c(z_c - z_1)}{a} + x_1, y_c, z_c \right) \\ D_2 &= \left(x_c, \frac{-a(x_c - x_1) - c(z_c - z_1)}{b} + y_1, z_c \right) \\ D_3 &= \left(x_c, y_c, \frac{-a(x_c - x_1) - b(y_c - y_1)}{c} + z_1 \right) \end{aligned}$$

where $C : (x_c, y_c, z_c)$ is the cell center. If one of these 3 points lies within the pressure cell and within the triangle, then this pressure cell is blocked out of the computational domain and does not contribute to the numerical solution. Verifying if a point lies in a triangle is done in the following way: Let us consider a point D that has been found to lie on the plane defined by a triangle (see Figure 2.4). The corresponding criterion implies the normal vectors:

$$\begin{aligned} \vec{n}_1 &= \left(\vec{P_1P_2} \times \vec{P_1P_3} \right) \times \vec{P_1P_2} \\ \vec{n}_2 &= \left(\vec{P_1P_3} \times \vec{P_1P_2} \right) \times \vec{P_1P_3} \\ \vec{n}_3 &= \left(\vec{P_2P_3} \times \vec{P_2P_1} \right) \times \vec{P_2P_3} \end{aligned}$$

The point D is inside the triangle if $\left(\vec{n}_1 \cdot \vec{d_1}\right)$, $\left(\vec{n}_2 \cdot \vec{d_2}\right)$ and $\left(\vec{n}_3 \cdot \vec{d_3}\right) \geq 0$. Once all the cells have been checked, we obtain a thin layer of blocked cells along the surface of the body. The interior of the body must also be blocked. This is easily done by a "painting" algorithm, i.e. the user specifies one cell which is in the flow field (open cell), and by iteratively marking the neighbours of the open cells unless they are blocked, we can paint the exterior of the body and thus the interior is easily identified.

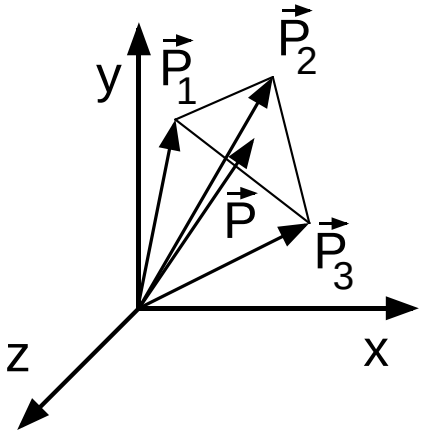

Fig. 2.2: Definition of a triangle

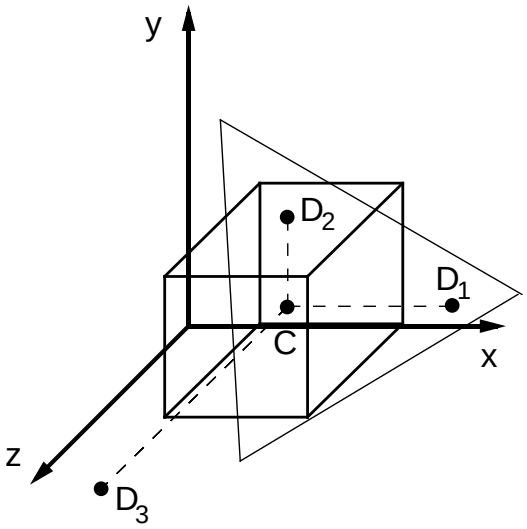

Fig. 2.3: Intersection of a triangle and a cell

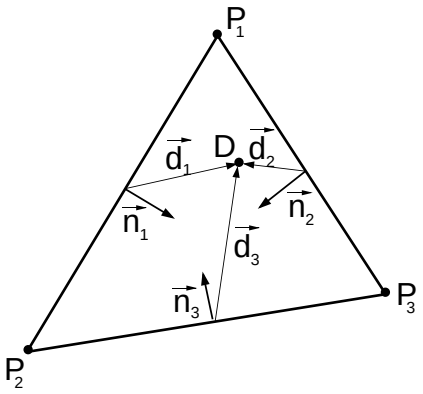

Fig. 2.4: A point lying in a triangle

2.2.2 Determining Dirichlet velocity boundary conditions

Once we have obtained the blocking array of the pressure cells, the blocking arrays of the velocities can be deduced in a straightforward manner. Each velocity component belonging to a blocked pressure cell is also blocked. In order to represent the effect of the body on the surrounding flow, a few layers (enough to have a complete stencil of the discretization at the first open cell) of blocked velocities are interpolated/extrapolated using the no-slip condition that prevails at the surface of the body. We use third order Lagrangian polynomials to achieve this goal.

In Figure 2.5, x_p is the location of the point to obtain an extrapolated variable, x_1 is the location of the surface of the body and x_2, x_3, x_4 are the positions of the neighbouring points. ϕ_p is the variable to be extrapolated (say a velocity component), ϕ_1 is the value at the wall which should be zero in case of a no-slip condition, ϕ_2, ϕ_3, ϕ_4 are the values taken from the neighbouring points.
The value of the extrapolated variable will be :

$$\phi_p = \sum_{i=1}^{4} \alpha_i \phi_i$$

where

$$\alpha_i = \prod_{j=1, j\neq i}^{4} \frac{(x_p - x_j)}{(x_i - x_j)}$$

We can define the distance Δ_k from the extrapolated point to the wall as $\Delta_1 = |x_p - x_1|$, e.g.. If the variable at a point can be extrapolated from more

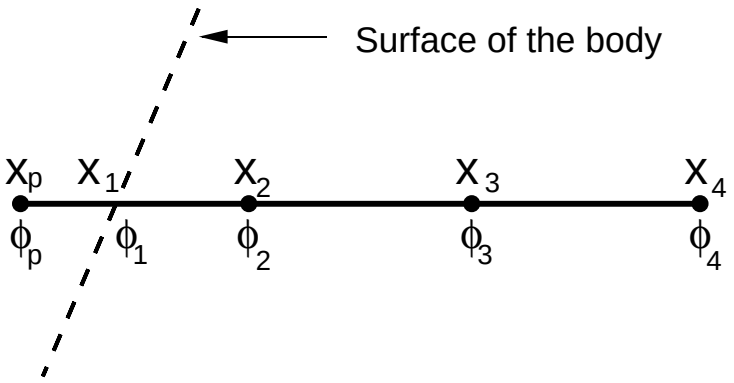

Fig. 2.5: Using computed velocities to determine the boundary conditions

than one direction, each direction is weighted by a multiplication factor γ_{dir}:

$$\gamma_{dir} = \frac{\beta_{dir}}{\sum_{k=1}^{Ndir} \beta_k}$$

where

$$\beta_{dir} = \frac{\prod_{k=1,k\neq dir}^{Ndir} \Delta_k}{\Delta_{dir}}$$

This formulation ensures that if a point is exactly on a wall, it will have the wall value. Also, the sum of the multiplication factors is always 1. From these simple formulas, all the coefficients needed to set the velocities at the surface of the body are determined and used during the actual computation.

2.2.3 Implementation in MGLET

To keep the number of indispensable modifications to the original version of MGLET to a minimum and to favor portability of the method eventually to other codes, we have adopted the following strategy. In the preprocessing step mentioned above, MGLET provides a grid along with an identification number related to it. The cartesian library then reads a geometry file containing an unstructured surface mesh describing the body considered. The blocking array and the interpolation/extrapolation stencils are then generated as described above. This information is accessible to MGLET via its identification number, allowing for computations on multiple grid like for example when using domain decomposition for parallelization.

The explicit time marching scheme makes it simple to implement Dirichlet boundary conditions for velocities. All the cells are treated in the same manner and once all the cells have been updated, the new boundary conditions are recomputed at the surface of the immersed boundary. The new Poisson equation solved now reads

$$Div\left[G\left(p^{n+1}\right)\right] = \frac{1}{2\Delta t} Div\left(u^*\right) B \tag{2.10}$$

where B is the blocking array, containing only 0 or 1 depending on whether a cell is blocked or within the flow respectively. The velocity correction step is now

$$u^{n+1} = u^* - 2\Delta t G\left(p^{n+1}\right) B \tag{2.11}$$

which ensures that blocked velocities will not be modified. After each time step, new velocity boundary conditions are recomputed and we can proceed with the next time step.

2.3 Validation tests

Validation tests were conducted in order to answer the following questions:

- Does the immersed boundary method presented above preserve second order numerical accuracy?
- Does it provide results comparable in accuracy to that of other codes in steady and unsteady laminar flows?
- Can it be used to predict complex 3D turbulent flows?

The following results provide an answer to these questions.

2.3.1 Cylindrical Couette flow

This test case was performed in order to evaluate whether the method preserves the second order accuracy of the code MGLET. This test case also demonstrates the possibility of handling surfaces with non-zero velocity boundary conditions. In this particular configuration, the inner cylinder has a diameter of 1 meter and is rotating while the outer one has a diameter of 6 meters and is kept at rest. The Reynolds number based on the rotation velocity of the inner cylinder is equal to 120. Four different equidistant grids were

used to compute the cylindrical Couette flow (which is a one-dimensional flow problem at low Reynolds numbers), the grid spacing $\Delta x_i = r_i - r_{i-1}$ was varied from 0.1m to 0.025m.

The analytical solution for the tangential velocity v_t is given by [50]

$$v_t = \frac{A}{r} + Br \tag{2.12}$$

The pressure p is

$$\frac{p}{\rho} = \frac{-A^2}{2}\frac{1}{r^2} + 2ABlogr + \frac{B^2}{2}r^2 + D \tag{2.13}$$

where A,B and D are constants to be determined using the boundary conditions. ρ is the density of the fluid and r the radial position.

The boundary conditions are

$$at \quad r = r_1 \quad : \quad v_{t_1} = \omega_1 r_1 \tag{2.14}$$
$$at \quad r = r_2 \quad : \quad v_{t_2} = \omega_2 r_2 \tag{2.15}$$
$$\tag{2.16}$$

where ω_i is the angular velocity of the cylinder.

We have set

$$r_1 = 0.5 \quad m \tag{2.17}$$
$$r_2 = 3.0 \quad m \tag{2.18}$$
$$\omega_1 = 0.6\pi \quad 1/s \tag{2.19}$$
$$\omega_2 = 0.0 \quad 1/s \tag{2.20}$$
$$\rho = 1.0 \quad kg/m^3 \tag{2.21}$$

for which we find

$$A = \frac{-\omega_1 r_1^2 r_2^2}{r_1^2 - r_2^2} \tag{2.22}$$

$$B = \frac{\omega_1 r_1^2}{r_1^2 - r_2^2} \tag{2.23}$$

The constant D in eq. (2.13) is an arbitrary offset for the pressure level that we set to 0.

The error ϵ at a position r_i is defined as

$$\epsilon_v(r_i) = v_t(r_i) - v_t^\star(r_i) \tag{2.24}$$

for the tangential velocity and

$$\epsilon_p(r_i) = p(r_i) - p^\star(r_i) \tag{2.25}$$

for the pressure where $v_t^\star$ and $p^\star$ are the numerical solutions. The RMS value of the error is defined as

$$\epsilon_{v_{rms}}^2 = \frac{1}{N}\sum_{i=1}^{N} {\epsilon_v}^2(r_i) \tag{2.26}$$

for the tangential velocity and

$$\epsilon_{p_{rms}}^2 = \frac{1}{N}\sum_{i=1}^{N} {\epsilon_p}^2(r_i) \tag{2.27}$$

for the pressure. N is the number of points in the numerical simulation. It is convenient to use the relative errors defined as

$$\epsilon_{v_{rel}} = \frac{\epsilon_{v_{rms}}}{\overline{v_t}} \tag{2.28}$$

and

$$\epsilon_{p_{rel}} = \frac{\epsilon_{p_{rms}}}{\overline{p}} \tag{2.29}$$

where $\overline{v_t}$ and $\overline{p}$ are respectively the mean tangential velocity and mean pressure:

$$\overline{v_t} = \frac{1}{N}\sum_{i=1}^{N} v_t(r_i) \tag{2.30}$$

$$\overline{p} = \frac{1}{N}\sum_{i=1}^{N} p(r_i) \tag{2.31}$$

Figures 2.6 and 2.7 show the radial distributions of the tangential velocity and the pressure. Very good agreement with the exact solution is obtained on the finer meshes while only a slight discrepancy is noted on the coarsest mesh. This shows that sufficiently accurate solutions can be obtained, and that the method is suited for surfaces having non-zero velocity.

Figure 2.8 shows the variation of the relative errors $\epsilon_{v_{rel}}$ and $\epsilon_{p_{rel}}$ as a function of the grid spacing. For a method to be second order accurate, the error has to be proportional to the square of the grid spacing, which is the case in this configuration.

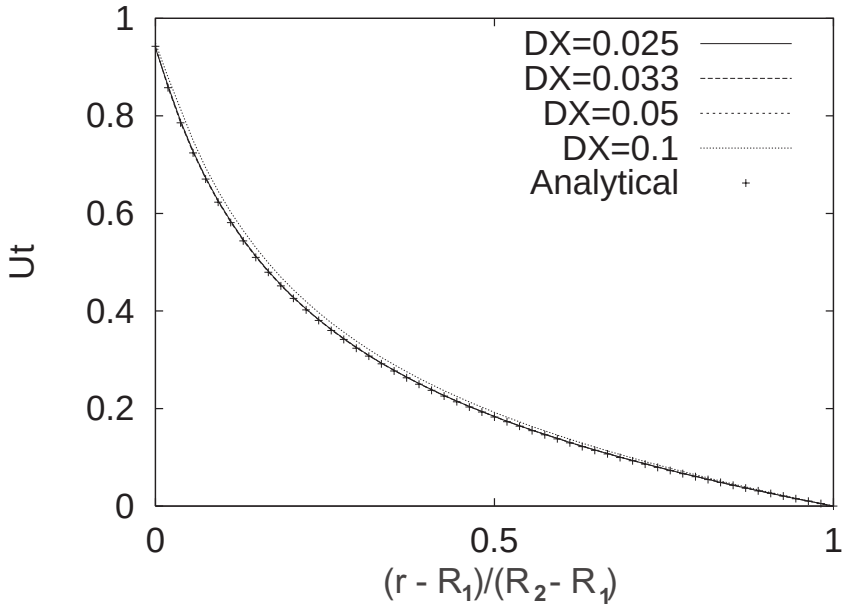

Fig. 2.6: Radial distribution of the tangential velocity in a laminar cylindrical Couette flow for different grid spacing

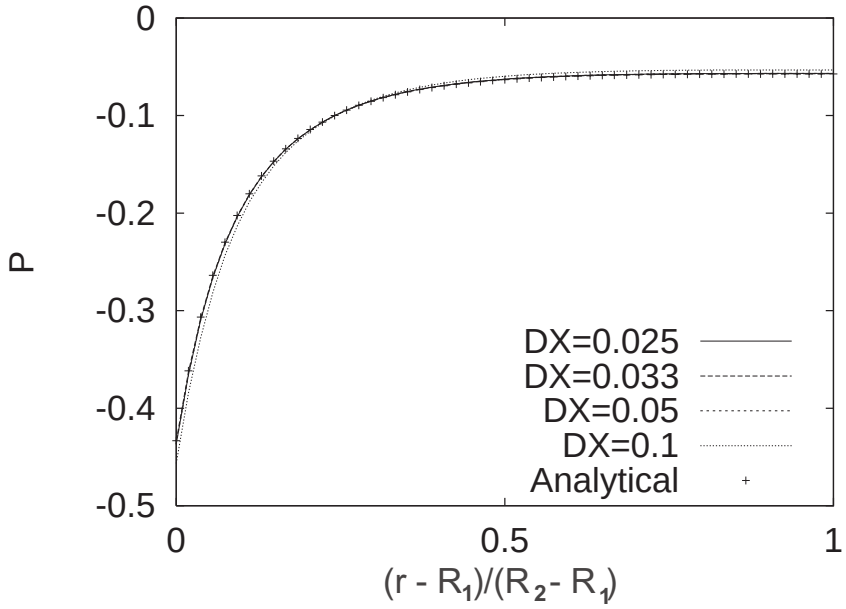

Fig. 2.7: Radial distribution of the pressure in a laminar cylindrical Couette flow for different grid spacing

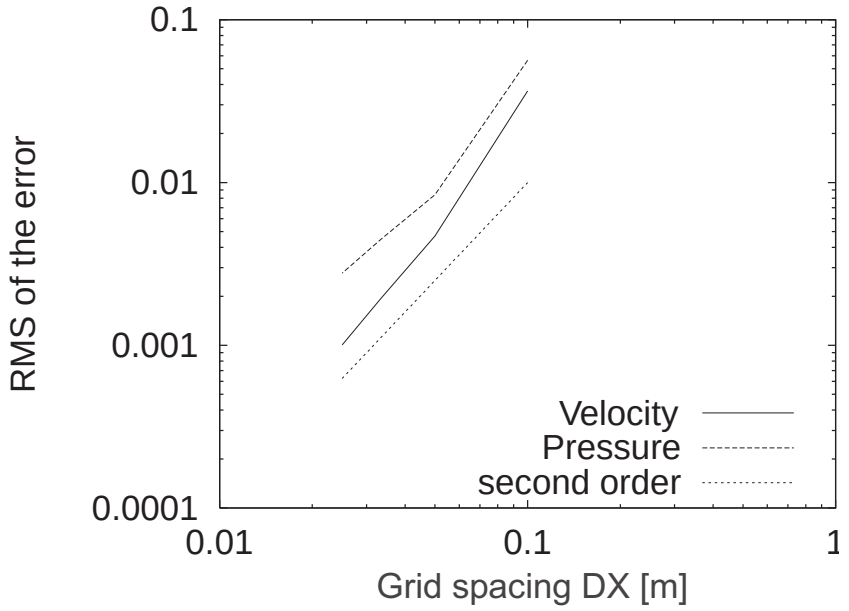

Fig. 2.8: RMS of the error as a function of grid spacing for the laminar cylindrical Couette flow

2.3.2 Circular cylinder between parallel plates

The next step is to compare our own results to those obtained by other authors. A steady and an unsteady laminar 2D test case have been computed. The configuration chosen is a cylinder with a circular cross-section mounted between 2 parallel plates with no-slip conditions on the plate and cylinder surfaces. The inflow condition for the velocities corresponds to fully developed laminar channel flow. A sketch of the geometry can be seen in Figure 2.9. The cylinder is not exactly centered between the plates, so that lift is produced. This configuration was studied by Schäfer et al.[40]. In their study, several codes using a wide variety of discretization schemes were employed to compute a steady state flow at $Re = 20$ and the unsteady flow at $Re = 100$.

The density ρ is set to 1.0 kg/m^3 and the viscosity $\nu = 0.001\ m^2/s$. H is the height of the channel ($0.41m$). The inflow velocity profile is set to

$$U(y) = 4U_m y(H - y)/H^2 \tag{2.32}$$

and

$$V(y) = 0 \tag{2.33}$$

where y varies from 0 to H, and U_m is the velocity in the center of the channel.

The Reynolds number is defined as

$$Re = \frac{\overline{U}D}{\nu} \tag{2.34}$$

where $D = 0.1m$ is the diameter of the cylinder and $\overline{U}$ is the mean inflow velocity $\overline{U} = 2U_m/3$.

The following parameters were computed by contributors to [40]. The values found were scattered between a lower and an upper bound. They are used for comparison with the present results.

$$C_D = \frac{2F_D}{\rho \overline{U}^2 D} \tag{2.35}$$

is the drag coefficient with F_D defined as

$$F_D = \int_S (\nu \frac{\partial v_t}{\partial n} n_y - P n_x) dS \tag{2.36}$$

The lift coefficient is defined as

$$C_L = \frac{2F_L}{\rho \overline{U}^2 D} \tag{2.37}$$

F_L is defined as

$$F_L = -\int_S (\nu \frac{\partial v_t}{\partial n} n_x + P n_y) dS \tag{2.38}$$

S is the surface of the cylinder, n its unit normal vector pointing outward, with x-component n_x and y-component n_y. v_t is the tangential velocity to the cylinder surface.

$$\Delta P = P_f - P_b \tag{2.39}$$

is the pressure difference between the front (pressure P_f) and the back (pressure P_b) of the cylinder.

Specific to the steady case, the recirculation length L_r is computed. It corresponds to the position where the streamwise velocity changes sign along the symmetry line behind the cylinder. In the unsteady case ($Re = 100$), the lift, drag and pressure difference vary in time due to the vortex shedding. We present the maximum values achieved. The Strouhal number is defined as

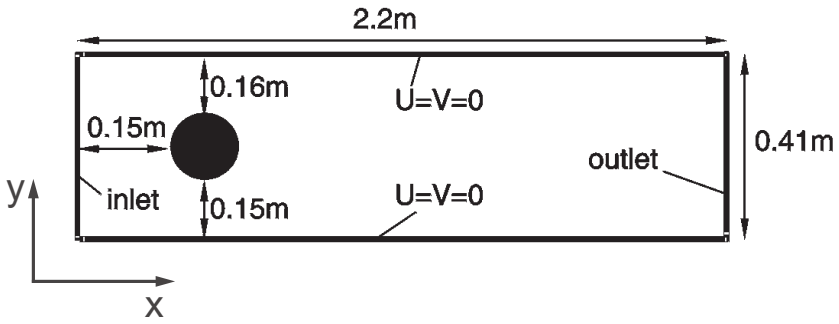

Fig. 2.9: Geometry of the 2D laminar test case

$$St = \frac{\omega_{st} D}{\overline{U}} \tag{2.40}$$

where ω_{st} is the frequency of the vortex shedding.

For the steady case, we used 3 different grids. The grids have equidistant spacings in the direction normal to the channel plates, with respectively 20, 30 and 40 cells per diameter of the cylinder. In the streamwise direction, the grids were slightly stretched in the front and in the back of the cylinder, but kept equidistant across the cylinder with the same spacings as their respective normal direction.

The results are presented in Table 2.1. We note the asymptotic convergence of the solution toward the results found in [40] as we increase the resolution around the cylinder.

We also used 3 grids to compute the unsteady flow at $Re = 100$. The same approach as for the steady flow was used to generate the first two grids, while the last one used stretching in both directions to achieve better resolution near the cylinder with fewer cells. We used 20, 40 and 60 cells to discretize the diameter of the cylinder. The results are presented in Table 2.2. We note again the asymptotic convergence of our solution towards the accepted lower and upper bounds found in [40] with the use of smaller grid spacing across the cylinder.

From these two validation tests, we conclude that our results are in good agreement with computations done with other codes and methods, the results of which were scattered between the lower and upper bounds and often beyond the limits.

Dimensions	Cells	C_D	C_L	L_r	ΔP
270x82	22 140	5.587	0.0115	0.0831	0.1162
330x123	40 590	5.572	0.0109	0.0839	0.1170
420x164	68 880	5.570	0.0109	0.0841	0.1172
	lower bound	5.57	0.0104	0.0842	0.1172
	upper bound	5.59	0.0110	0.0853	0.1176

Tab. 2.1: Parameters for the steady flow over a cylinder between parallel plates ($Re = 20$)

Dimensions	Cells	C_{Dmax}	C_{Lmax}	St	ΔP_{max}
440x82	36 080	3.27	0.8820	0.299	2.426
880x164	144 320	3.23	0.987	0.302	2.486
700x200	140 000	3.22	1.000	0.302	2.496
	lower bound	3.220	0.9900	0.2950	2.460
	upper bound	3.240	1.0100	0.3050	2.500

Tab. 2.2: Parameters for the unsteady flow over a cylinder between parallel plates ($Re = 100$)

2.3.3 Turbulent pipe flow

In order to demonstrate the applicability of the method to 3D turbulent flows, we computed the fully developed flow in a circular pipe at $Re_\tau = 180$ directly, resolving all turbulent scales. We compare our results to the results obtained using a code [18] for helical as well as cylindrical coordinates. The grid was chosen so that the closest point is at around $y^+ = 0.5$ away from the wall and that there are approximatively 10 points below $y^+ = 10$ at a position with the coarsest resolution, located at $\Theta = 45$ degrees. In the middle of the pipe, the grid spacing is $\Delta y^+ = 5.0$. The grid can be seen in Figure 2.10, only one quarter of the pipe is shown. Our conservative decisions give rise to a grid which has 256x256 points in a cross section normal to the pipe axis. In the streamwise direction, the grid spacing is $\Delta x^+ = 7.0$ and 256 points are used.

No slip is applied by our immersed boundary technique at the surface of the pipe and periodicity is used in the streamwise direction. The simulation was started from an initial uniform streamwise velocity with superposed random fluctuations in all velocities. After an initial transient period, statistics were gathered for $Tu_\tau/R = 10$, where u_τ is the friction velocity and R is the radius

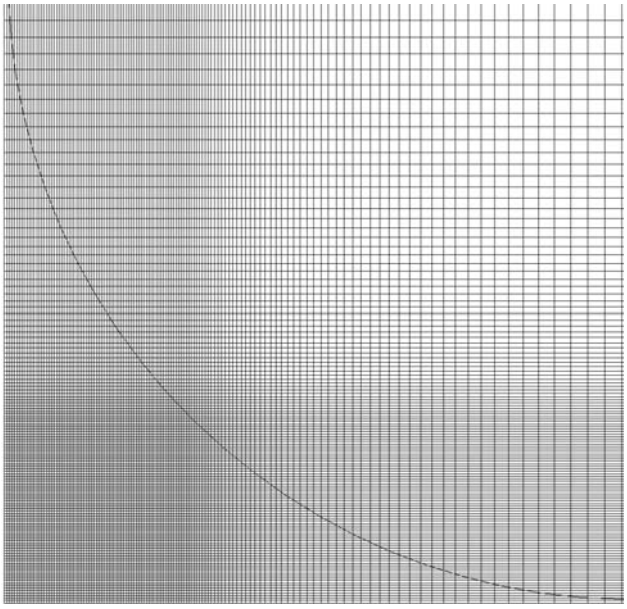

Fig. 2.10: Grid used for the computation of turbulent pipe flow, only one quarter of the pipe shown

of the pipe. The streamwise direction is the only homogeneous direction that can be used to enhance the statistical sampling.

The mean streamwise velocity profile is presented in Figure 2.11. Our results are in excellent agreement with those of [18]. The RMS values of velocity fluctuations are presented in Figures 2.12 and 2.13. Near the wall, our results show no artefacts resulting from our treatment of the boundary. A slight difference is noted in the magnitude of the peaks. The difference is overall small and can be partly attributed to a lack of statistical samples. In our case, we did not benefit from the circumferential direction, which is homogeneous in a cylindrical, but not in a cartesian coordinate system, to enhance the statistics. On the other hand, using a cartesian grid removes the singularity at the centreline associated with a cylindrical coordinate system.

We must confess that the method works more efficiently in flow situations around bodies, since there is less overhead of blocked cells (e.g. flow around a circular cylinder or an airfoil). In our computation of the pipe flow one can notice in Figure 2.10 that the regions where the grid is most refined lie outside of the computational domain. In any case, the DNS results obtained with the present method are in good agreement with previous DNS data, which confirms the suitability of the present technique for DNS of turbulent flows.

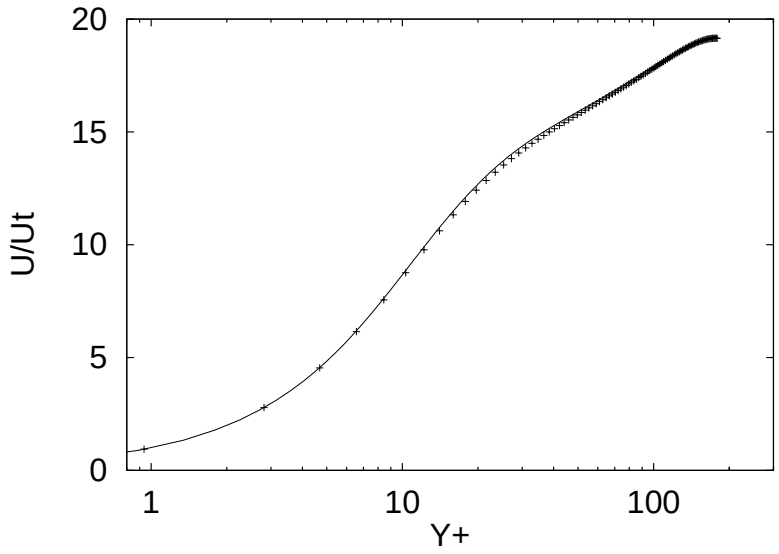

Fig. 2.11: Turbulent pipe flow ($Re_\tau = 180$): Mean axial velocity profile. Lines: cartesian method, Symbols: cylindrical code [18].

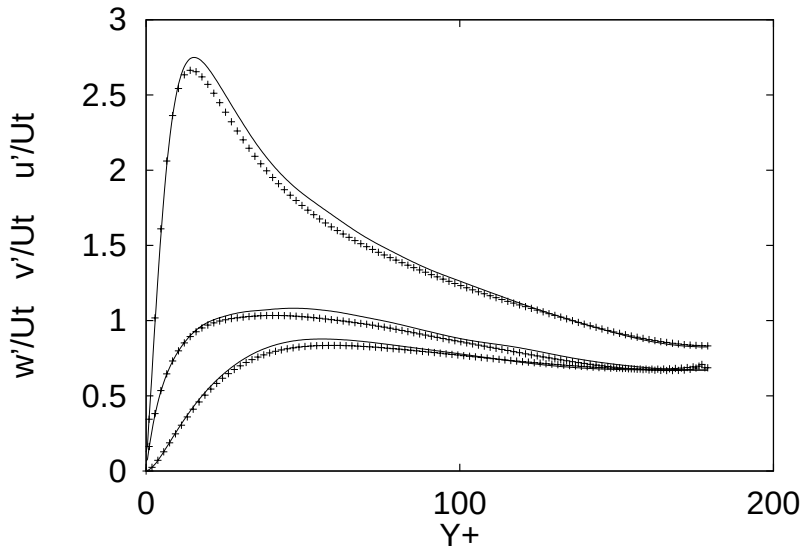

Fig. 2.12: Profiles of the RMS velocity fluctuations in turbulent pipe flow ($Re_\tau = 180$). Lines: cartesian method, Symbols: cylindrical code [18].

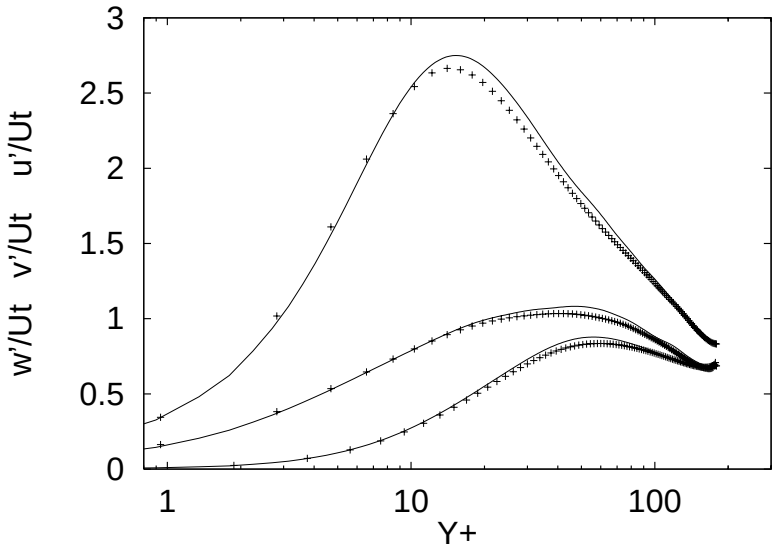

Fig. 2.13: Profiles of RMS velocity fluctuations in turbulent pipe flow ($Re_\tau = 180$). Semi-logarithmic plot. Lines: cartesian method, Symbols: cylindrical code [18].

3. DNS of the flow around a circular cylinder at Re = 3900

In this chapter, a DNS of the flow around a circular cylinder at $Re = 3900$ is presented. Results are compared to numerical and experimental data obtained by other authors.

3.1 Computational details

3.1.1 Resolution issues

Our computational domain is shown in Figure 3.1. It extends over 20 diameters D in the streamwise x-direction, with the center of the cylinder being $5D$ downstream of the inflow plane. In the normal y-direction, the domain size is also $20D$. The spanwise extent of the domain was chosen to be $L_z = \pi D$, which corresponds to the size used by most previous authors. The boundary conditions prescribed in the present simulation are a uniform unperturbed inflow velocity U_∞ and periodicity of the velocity components in the spanwise direction. A zero-gradient outflow condition holds at $x = 15D$. Instead of using uniform inflow velocity, Kravchenko and Moin [21] prescribed potential flow velocities. The streamwise potential flow velocity in the symmetry plane at $x/D = -5$ differs from U_∞ by only 1%. We presume this difference to have a negligible effect on the overall flow structure. On the horizontal planes, i.e $y = -10D$ and $y = +10D$, periodicity in y-direction is enforced. We will see later that this boundary condition has a minor impact on the solution in the form of a slight blockage effect. The initial conditions for the velocities are a uniform streamwise flow with no perturbation in the other directions. The pressure is set to zero in the whole domain at the initial time. The total number of cells N_x, N_y, N_z in (x,y,z)-directions is 706x594x112. In the attached boundary layer on the cylinder, a minimum grid spacing of $0.004D$ was used to ensure a proper resolution. In the square DxD which contains the cylinder 150x190 cells were used in the streamwise and the normal directions, respectively. Figures 3.2 and 3.3 show the grid spacing used

as a function of the position in the computational domain in the streamwise x-direction and the vertical y-direction, respectively. On Figure 3.3 only the upper half is shown, the lower half is symmetric. Coarse grids can be used in the regions in front and in the y-direction away from the cylinder where the flow is quasi-uniform and no gradients need to be resolved. The grid in the neighbourhood of the cylinder has been chosen in such a way that the laminar boundary layer is properly resolved. An estimate of the boundary layer thickness is obtained, adopting the flat plate boundary formula

$$\frac{\delta_{99}}{x} \approx \frac{5.0}{\sqrt{Re_x}} \tag{3.1}$$

$$Re_x = \frac{u_\infty x}{\nu} \tag{3.2}$$

and assuming curvature effects small. With $x = \pi D/2$, the boundary layer thickness at the zenith of the cylinder is:

$$\frac{\delta_{99}}{D} \approx 0.1 \tag{3.3}$$

According to figures 3.2 and 3.3, there are at least 10 grid points within the boundary layer at $\Theta = 45$ degrees, measured from the front stagnation point. This seems us to form an adequate resolution.

3.1.2 Statistical sampling and computational costs

The simulation was run with a constant time step size of $\Delta t = 0.001 D/U_\infty$ which ensured that the maximum Courant number is small enough (CFL=0.25) to guarantee a stable computation. It is not always advantageous to chose the largest time step allowed by the numerical schemes. The iterative Poisson solver used in the code MGLET needs larger number of iterations to converge when the initial guess is further away from the desired solution. This means that when the time step size is increased, it takes longer to advance the complete fields over one time step. On the other hand, setting a very small time step size reduces the CPU time required for one time step, but in terms of physical time duration $T = D/U_\infty$, it takes more time steps and thus more CPU time. In between, there exists an optimal time step that provides the most physical time TU_∞/D for a given CPU effort. Our time step was chosen according to this consideration.

After about $T = 25 D/U_\infty$ problem times, the vortices behind the cylinder started to be shed downstream. We waited for an additional $T = 75 D/U_\infty$

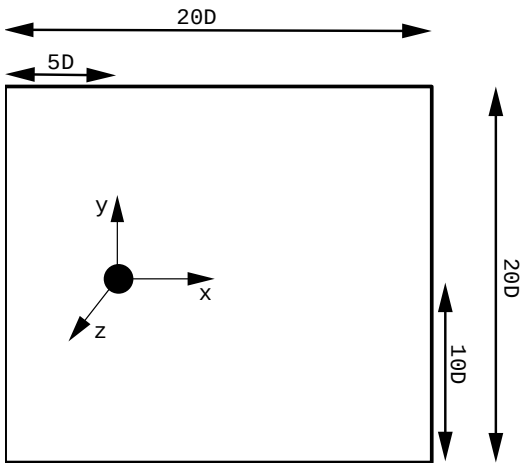

Fig. 3.1: The computational domain

or about 15 shedding cycles before starting the statistical averaging. The variables were spanwise and time averaged during a period of $T = 300D/U_\infty$, or about 60 shedding cycles. One sample was taken every 10 time steps. The components of the Reynolds stress tensor were computed from the relation:

$$< u'_i u'_j >=< u_i u_j > - < u_i >< u_j > \tag{3.4}$$

where the brackets denote time and spanwise averaging.

The computations were performed on the Fujitsu VPP700 of the Leibniz Rechenzentrum (LRZ) in Munich. The architecture of the VPP700 allows two levels of code optimization. The finer level is the use of the vector unit of the processors. The most inner loop should not contain any recursive reference of the variables. This translates for example in the use of a red-black algorithm within the iterative Poisson solver in the code MGLET which is similar in principle to the Gauss-Seidl algorithm. The coarser level of optimization is the use of domain decomposition with inter-node communication. 8 nodes were used in parallel with domain decomposition in the spanwise direction. MPI communication was used to exchange the variables located on the boundaries of the domain's partitions. The average total performance was about 6.5 Gflops or 810 Mflops per node. The total memory consumption reached about 9.6 GBytes. 10 seconds were needed to perform one time step. The total number of time steps was $4 \cdot 10^5$. 8900 CPU hours were needed to carry out the whole simulation, all 8 nodes summed together, or 46 computing days in wall clock time.

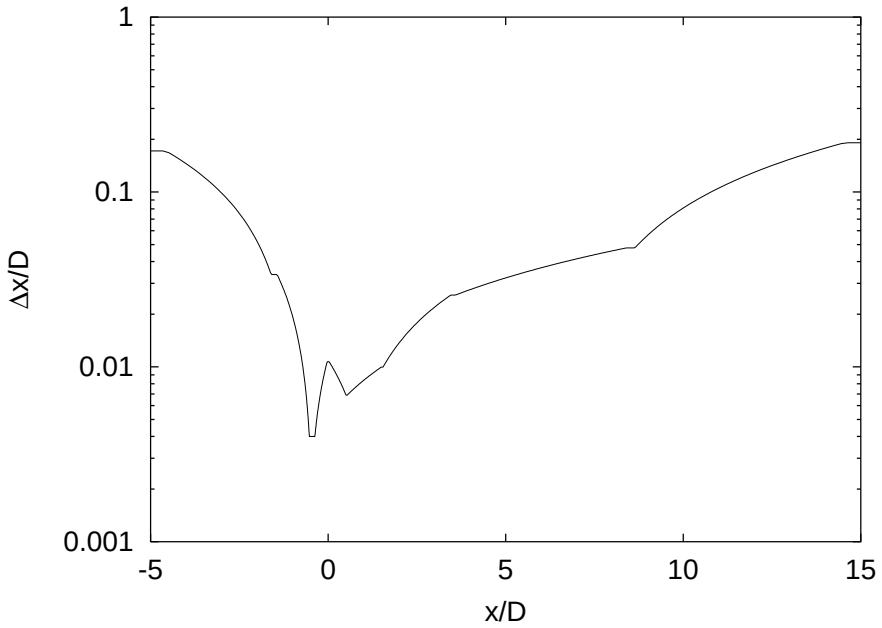

Fig. 3.2: Grid spacing Δx as a function of the position x

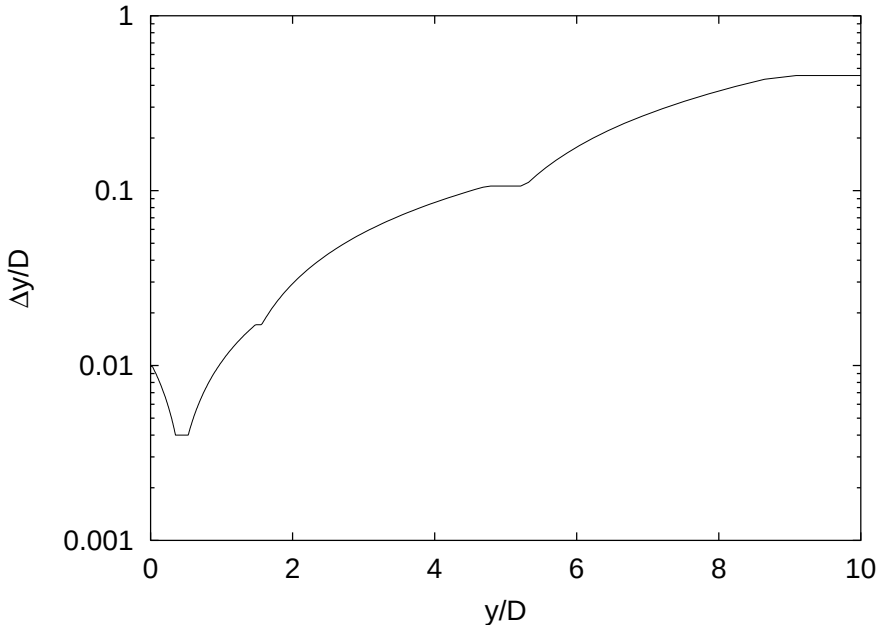

Fig. 3.3: Grid spacing Δy as a function of the position y

3.2 Instantaneous flow field

Based on flow visualization results, Perry et al.[36] had suggested a mechanism for the Kármán vortex street formation in the near wake region. They also pointed out, consistently with Cantwell and Coles' findings [7], that the vortex shedding process is Reynolds number independent. The present results confirm the vortex formation mechanism and demonstrate it with the help of the Q-criterion. Q is defined in eq. (3.5) and represents the second invariant of the velocity gradient tensor. It is also related to the Laplacian of the pressure. Figure 3.4 shows the time evolution of the vortex street formation and the vortex shedding phenomenon. At the initial time (upper left), a vortex is formed in the upper half of the wake. While it propagates downstream ($t = T/7 - 2T/7$), it draws the shear layer on the lower half across the wake. This gives rise to a new vortex on the lower side ($t = 3T/7 - 4T/7$) which becomes stronger and travels downstream and in turn draws the upper free shear layer into the wake ($t = 5T/7 - 6T/7$) to complete the cycle with the generation of a vortex in the upper part of the wake.

Figures 3.5, 3.6 and 3.7 show isosurfaces of constant pressure fluctuations. Large vortical structures are easily identified. A complex arrangement of streamwise vortices (braids) links the Kármán vortices shed from successive cycles together. The spanwise spacing of these streamwise vortices is of the order of one cylinder diameter, in agreement with the B-mode secondary instability of the Kármán vortex street [55]. Stretching of the streamwise vortices occurs between the counter-rotating pair of newly formed primary (Kármán) vortices which enhance their strength. A self-sustainable cycle of formation of streamwise vortices is created by this mechanism. Also worth mentioning is the presence of vortices in the free shear layers, as seen in Figure 3.7 in the top shear layer. These Kelvin-Helmholtz vortices result from the instability of the shear layer which leads to transition to turbulence.

Figures 3.8 and 3.9 show isosurfaces of constant positive and negative spanwise velocity fluctuations. The highly three-dimensional nature of the wake is well illustrated. Streamwise bands of spanwise velocity fluctuations of opposite sign indicate the presence of the aforementioned streamwise vortices. The general shape of the Kármán street can be nicely observed on the side view, Figure 3.9.

Small vortical structures are well shown when using Hunt's Q-criterion (Hunt et al. [17]).

$$Q = \frac{1}{2}(\Omega_{ij}\Omega_{ij} - S_{ij}S_{ij}) = \frac{1}{2\rho}\frac{\partial^2 p}{\partial x_i \partial x_i} \tag{3.5}$$

where

$$\Omega_{ij} = \frac{1}{2}(\frac{\partial U_i}{\partial x_j} - \frac{\partial U_j}{\partial x_i}) \tag{3.6}$$

and

$$S_{ij} = \frac{1}{2}(\frac{\partial U_i}{\partial x_j} + \frac{\partial U_j}{\partial x_i}) \tag{3.7}$$

In Figure 3.10, isosurfaces of constant value of Q are shown, together with isosurfaces of constant pressure fluctuations. The highly organized nature of turbulence in coherent structures is noticed in the near wake region. The primary vortex plays a pivotal role in the transition process of the shear layers by feeding perturbations from further downstream back to the shear layers via the recirculation region. From visual inspection of a time sequence of frames like in Figure 3.4, we see that the structures fed to the shear layers by the primary Kármán vortices are elongated in the streamwise direction. This certainly results from the stretching caused by the counter rotating rollers. The Kelvin-Helmholtz vortices are also visible from the Q-criterion, and in addition, streamwise vortices linking two consecutive occurences of the Kelvin-Helmholtz vortices can be observed. They are similar to the ones present in the Kármán vortex street.

3.3 First and second order statistics

After an initial transient period of about 100 time units based on the free-stream velocity and the cylinder diameter, statistics of first and second order were gathered for $T = 300D/U_\infty$ and the 112 planes perpendicular to the spanwise direction were used as realizations. Drag and back pressure coefficients, the separation angle Θ_{sep}, the recirculation length L_r and the Strouhal number St, see eq. (2.40), were computed and are presented in Table 3.1. The drag coefficient C_D has been defined in eqs. (2.35-2.36) for laminar flow. If the velocity and pressure are replaced by their statistical mean values, this definition holds here. The back pressure coefficient reads:

$$C_{P_b} = \frac{\bar{p_b} - p_\infty}{\frac{1}{2}\rho {U_\infty}^2} \tag{3.8}$$

The separation angle Θ_{sep} is defined at the point of zero wall vorticity. The recirculation length, finally, is given as the distance between the rear stagnation point and the point on the symmetry plane where the mean streamwise velocity changes sign.

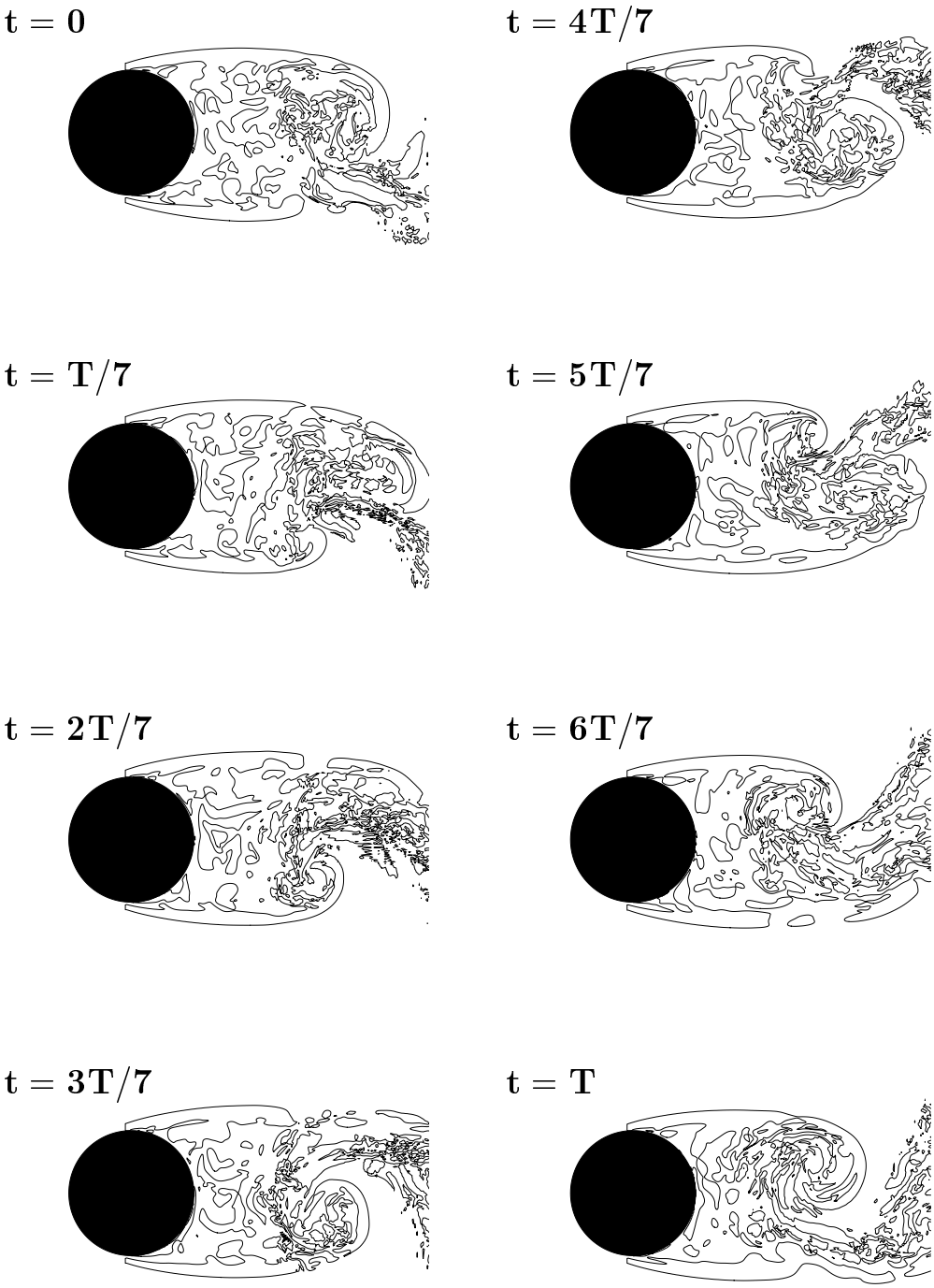

Fig. 3.4: Time evolution of the contour lines of the second invariant of the velocity gradient tensor $Q = 0.0001$ over one vortex shedding period $T = D/(U_\infty St)$.

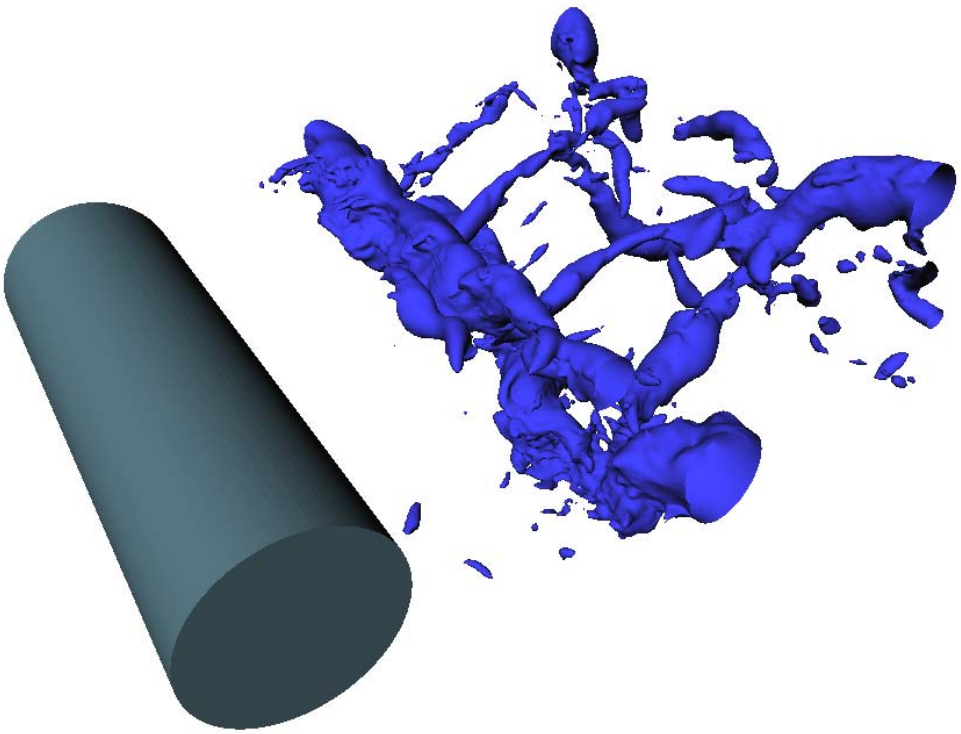

Fig. 3.5: Isosurfaces of pressure fluctuations $P'/\frac{1}{2}\rho U_\infty^2 = -0.5$, perspective view.

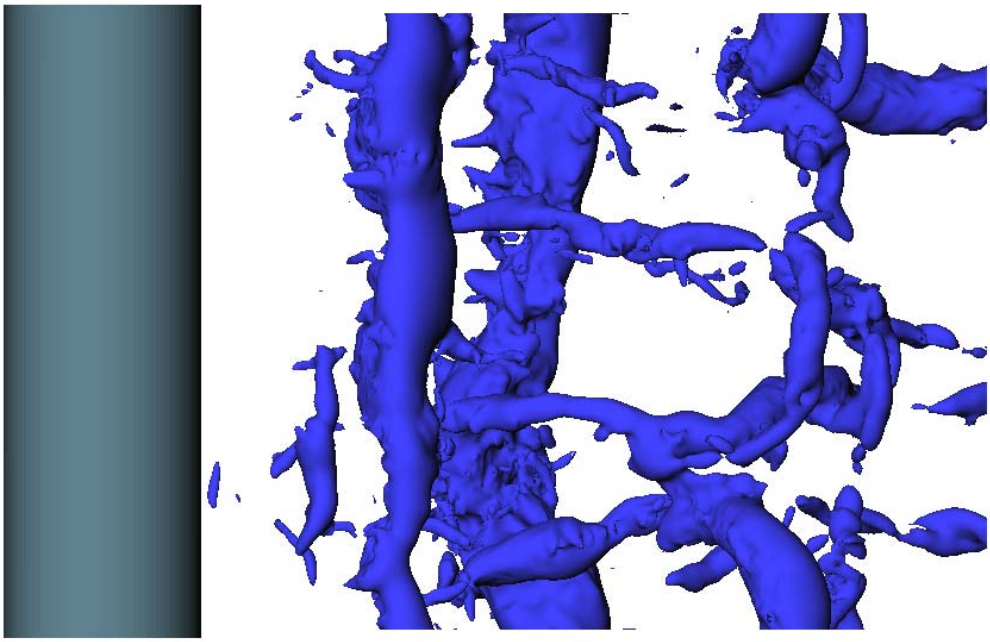

Fig. 3.6: Isosurfaces of pressure fluctuations $P'/\frac{1}{2}\rho U_\infty^2 = -0.5$, top view.

Fig. 3.7: Isosurfaces of pressure fluctuations $P'/\frac{1}{2}\rho U_\infty^2 = -0.5$, side view.

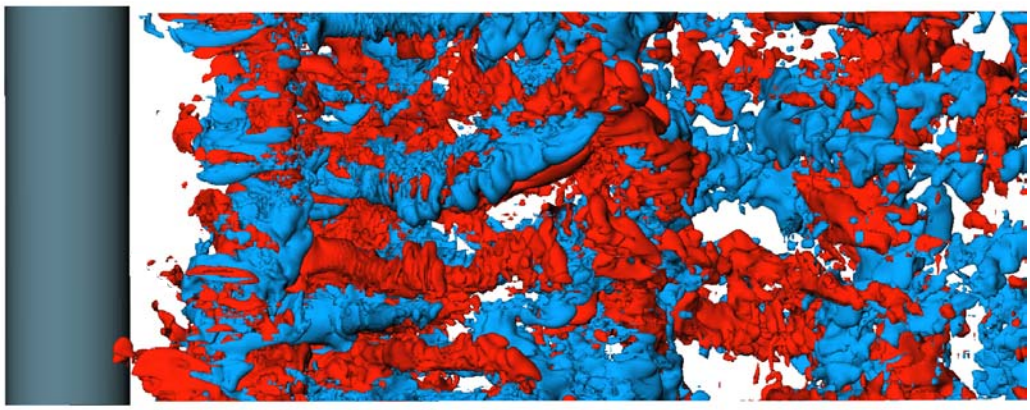

Fig. 3.8: Isosurfaces of spanwise velocity fluctuations $V'/U_\infty = \pm 0.2$, top view.

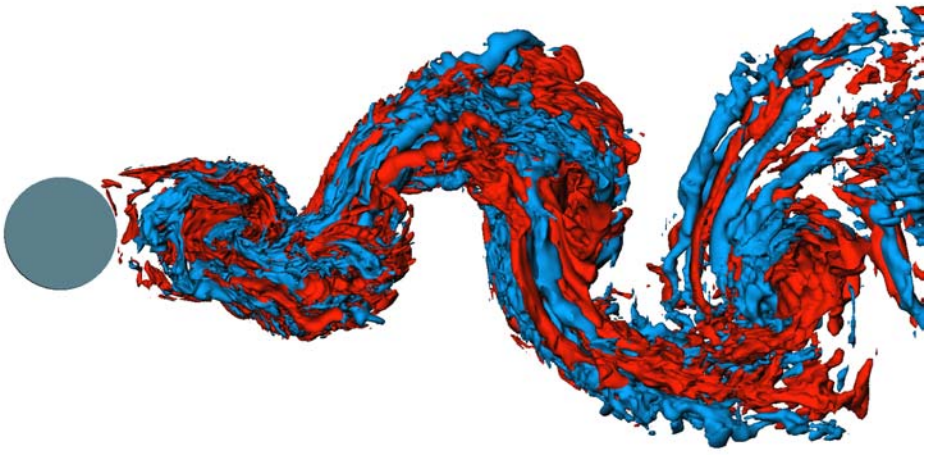

Fig. 3.9: Isosurfaces of spanwise velocity fluctuations $V'/U_\infty = \pm 0.2$, side view.

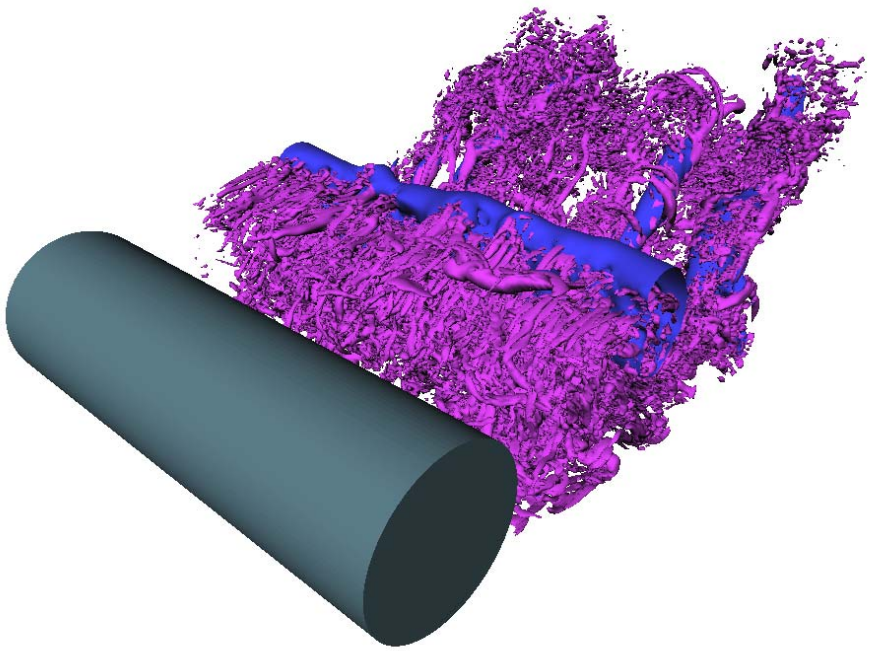

Fig. 3.10: Isosurfaces of pressure fluctuations $P'/\frac{1}{2}\rho U_\infty^2 = -0.5$, (darker gray), and of the second invariant of the velocity gradient tensor $Q = 25.0$, (lighter gray).

Data from	C_D	C_{Pb}	Θ_{sep}	L_r/D	St
exp	0.99 ± 0.05	-0.88 ± 0.05	86 ± 2	1.4 ± 0.1	0.215 ± 0.005
DNS [26], Case I	-	-0.96	-	1.12	0.203
Present DNS	1.03	-0.93	85.7	1.30	0.220

Tab. 3.1: Mean flow parameters from DNS and experiments.

We note the excellent agreement of our simulation when compared to the experiments. All the parameters are within the experimental accuracy. The data of Ma et al. [26] shows a smaller recirculation region which leads to a lower back pressure coefficient, a trend that is consistent.

Figure 3.11 shows the mean and instantaneous streamlines of the flow. The latter being obtained from the projection of the velocity field onto a 2D plane. In the mean, a nearly perfectly symmetric recirculation bubble is observed. No secondary recirculation is noted. The mean flow is distorted by the presence of the cylinder only in a small area around the cylinder, which confirms the validity of the boundary conditions used far from the cylinder in our computation. When looking at the instantaneous streamlines, we note a small secondary recirculation at the lower side of the cylinder. A strong vortex is also observed, originating from the upper side. The region of disturbed flow is obviously more extended in the instantaneous than in the mean flow, especially in the wake region.

Figure 3.12 presents contour lines of the mean streamwise velocity, the mean vertical velocity and the mean pressure, respectively from top to bottom. The number of samples used for averaging seems sufficient, excellent symmetry being observed. The recirculation length is easily identified by the change from dashed to solid contour lines of the mean streamwise velocity along the centreline of the wake. We note that the minimum pressure appears in the region of maximum backward flow within the recirculation bubble.

Figure 3.13 shows contour lines of the RMS velocity fluctuations in the streamwise, vertical and spanwise directions from top to bottom, respectively. Interestingly, two distinct maxima are observed on each side of the cylinder in the streamwise velocity fluctuations. The one occuring in the shear layer is the strongest. Its location corresponds well to the location where the wake vortex formation is initiated as discussed above and observed on Figure 3.4. The second peak is slightly downstream from the first one and closer to the symmetry line. It represents a relative maximum. The location of this peak seems to correspond to the location where the vortex migrates after the initial phase of its formation and where it grows in strength before

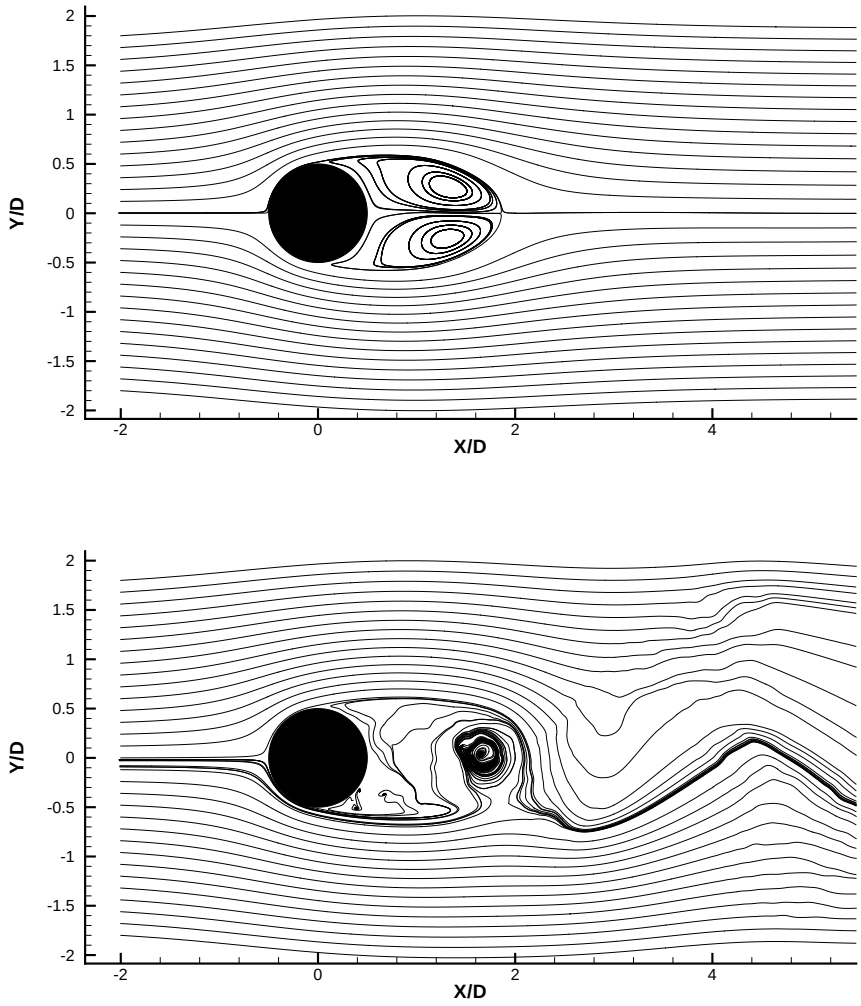

Fig. 3.11: Mean and instantaneous streamlines of the flow near the cylinder, the latter being obtained from the projection of the instantaneous velocity field onto a 2D plane.

being convected downstream. On the contour plot of the vertical velocity fluctuations, a maximum appears slightly downstream of the recirculation bubble. The spanwise velocity fluctuations are smaller in magnitude than those in the other directions. A maximum is observed in the recirculation region, just upstream of the closing of the bubble, indicating a high level of three-dimensionality in this area.

In order to validate our results we use data available both from numerical simulations and from experiments of other authors. The experimental data is the PIV measurements of Lourenco and Shih [24], published in [2], and the hot-wire experiment of Ong and Wallace [35]. The hot-wire device cannot be used in recirculating flows. Hence the data is available only downstream of the recirculation zone, i.e. $x/D > 3.00$. We also compare our results with the numerical simulations of Ma et al. [26]. Their DNS was conducted with spectral elements as discussed in Chapter 2. The data presented here are those of Case I in [26]. This case corresponds to a flow domain with a size in spanwise direction of $2\pi D$ which was resolved by 128 Fourier modes. The number of triangular elements in the (x,y)-plane was 902. Each element was filled with Jacobi polynomial modes of order 10. Hence, this case represented the highest spatial resolution case of all the runs discussed in [26].

Figure 3.14 presents the mean pressure coefficient distribution along the surface of the cylinder. The angle $\Theta = 0$ corresponds to the front stagnation point while $\Theta = 180$ correponds to the back of the cylinder. Only the pressure distribution on the upper half of the cylinder is shown, the other side is symmetric. We compare our results to those of the experiment of Norberg [34], carried out at a Reynolds number ($Re = 4020$) very close to the present one. The overall agreement is good. The location of the minimum pressure coefficient and the extent of the region along the back of the cylinder where the pressure coefficient is practically constant are well predicted.

In Figure 3.15, the mean streamwise velocity along the centreline of the cylinder is shown. We notice a good prediction of the recirculation length and its strength, reflected by the minimum velocity achieved. The rate of recovery of the flow is also well predicted. Our data matches the one of Ong and Wallace [35] in the region further downstream. There is no explanation for the apparent discrepancies observed between the experiments of Lourenco and Shih [24] and Ong and Wallace [35] around $x/D = 3.0$. A plateau appears in the data of Lourenco and Shih [24] while the trend in the near-wake is unknown for the hot-wire experiment of Ong and Wallace [35]. Similar plateaus were also observed in the experiments of Prasad and Williamson [37] at Reynolds numbers of 230, 260, 4473 and 5427. Although observed

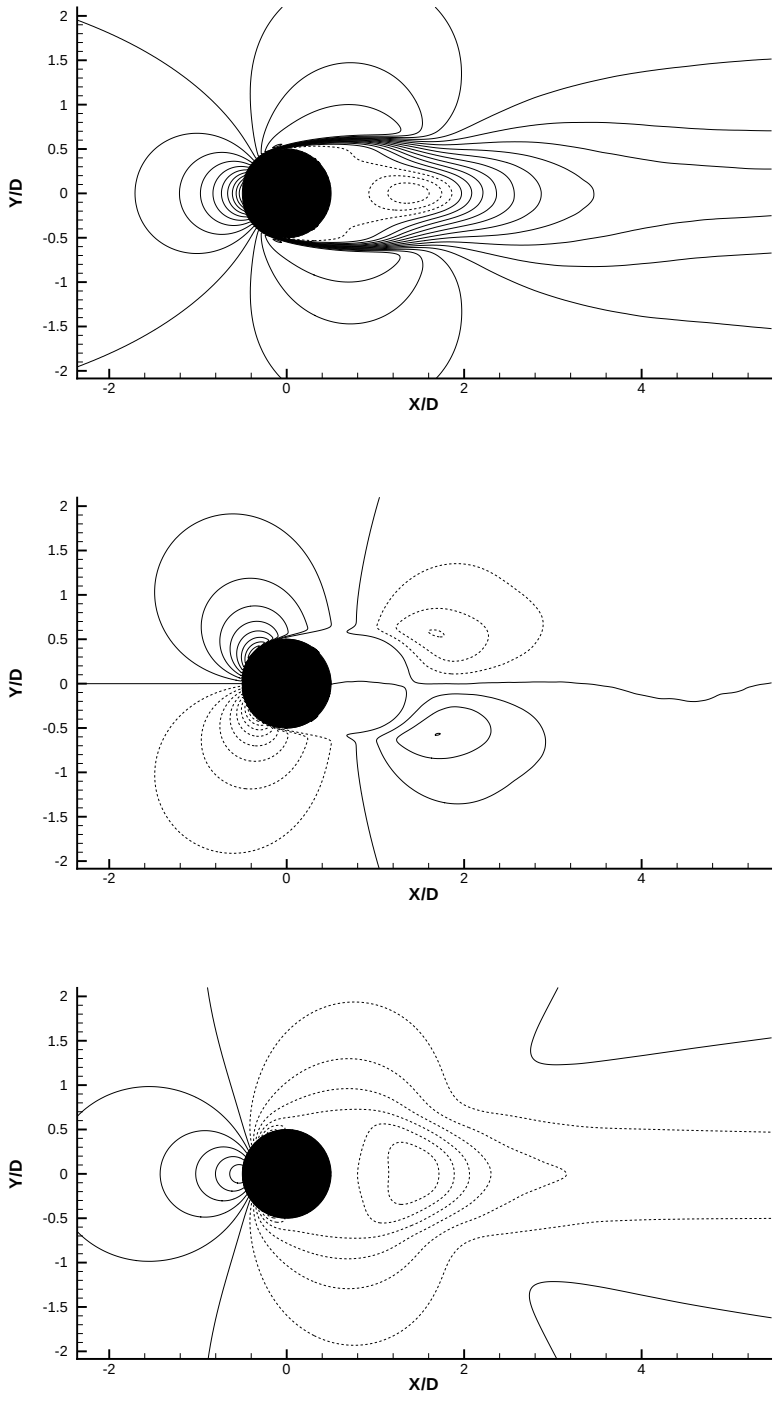

Fig. 3.12: Contours of mean streamwise velocity, vertical velocity and pressure from top to bottom. Streamwise velocity : $\bar{u}/U_\infty = -0.2$ to 1.4, 17 levels. Vertical velocity: $\bar{v}/U_\infty = -1.3$ to 1.3, 27 levels. Pressure : $\bar{p}/(0.5\rho U_\infty^2) = -1.4$ to 1, 13 levels.

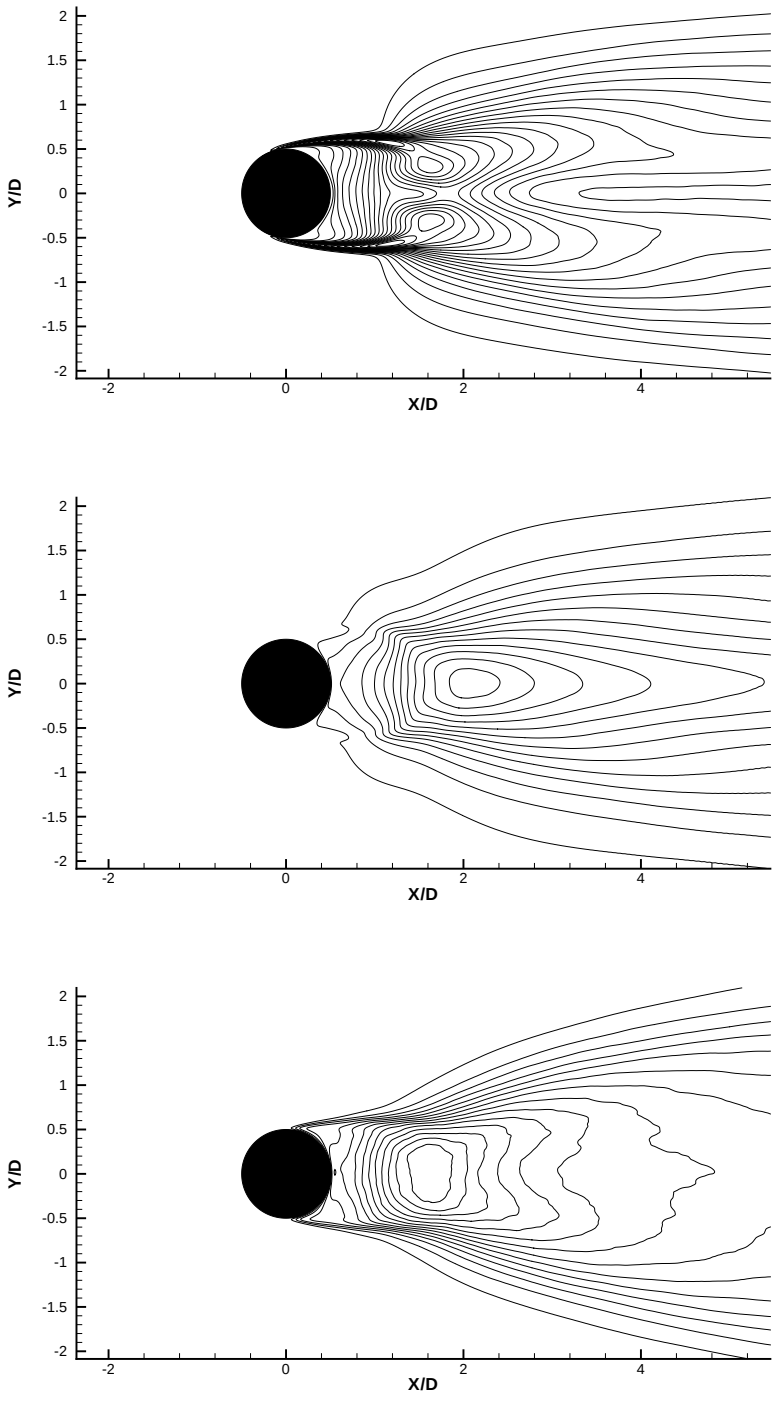

Fig. 3.13: Contours of the RMS streamwise, vertical and spanwise velocity fluctuations from top to bottom. Streamwise velocity fluctuations: $u'/U_\infty = 0$ to 0.7, 29 levels. Vertical velocity fluctuations: $v'/U_\infty = 0$ to 1.0, 21 levels. Spanwise velocity fluctuations: $w'/U_\infty = 0$ to 0.4, 21 levels.

experimentally, this plateau has never been predicted in any of the numerical simulations of the cylinder flow at $Re = 3900$ we know of. This leaves an open question that needs to be investigated. It is tempting to conjecture that a large scale phenomenon in the spanwise direction could be responsible for the appearance of the plateau. A possible candidate is the so-called vortex dislocation first described by Williamson [54]. Vortex dislocations are large scale phenomena occuring when the frequency of the Kármán vortex shedding goes out of phase along the span of the cylinder. Vortex dislocations appear naturally in the wake's 3D transition regime and at higher Reynolds number or can be caused by end-effects in experiments. Dislocations have a strong three-dimensional effect on the wake and hence could be partly responsible for the discrepancies between the measured and simulated streamwise velocity profiles.

Figures 3.16, 3.17 and 3.18 show vertical profiles of the mean streamwise velocity at streamwise locations ranging from $x/D = 1.06$ to $x/D = 10.0$. The agreement is generally good. We note a slight blockage effect due to the boundary conditions at $y/D \pm 10$ which leads to a 3% increase of the streamwise velocity $3D$ away from the cylinder. In the regions further downstream we note a reduced quality of the DNS data of Ma et al. [26] near the symmetry plane of the wake. This might be due to the fact that the data set provided was not sampled over a sufficiently long period of time. On the other hand the present DNS data also deviate from the experimental data in the free-stream region. Further simulations would be needed to clarify the effect of the boundary conditions there.

Figures 3.19, 3.20 and 3.21 show vertical profiles of the mean vertical velocity at the same downstream locations. Our simulation agrees well with the data of Ma et al. [26] except after $x/D \geq 3.00$. The experimental data of Lourenco and Shih [24] do not seem reliable for this quantity, it lacks the basic properties of symmetry and a zero value on the centreline.

Figures 3.22, 3.23 and 3.24 present vertical profiles of the variance of the streamwise velocity fluctuations at the locations described above. Good agreement is observed between all numerical data sets. Downstream of the near wake Ma et al.'s data are certainly not stable enough. The experimental data of Ong and Wallace [35] generally reveal lower amplitudes. In view of the relatively close agreement between the two DNS data sets, one is tempted to question the experimental acuracy.

Figures 3.25, 3.26 and 3.27 show vertical profiles of the variance of the vertical velocity fluctuations. Again, good agreement is observed between the numerical simulations, although in the region more downstream, we predict

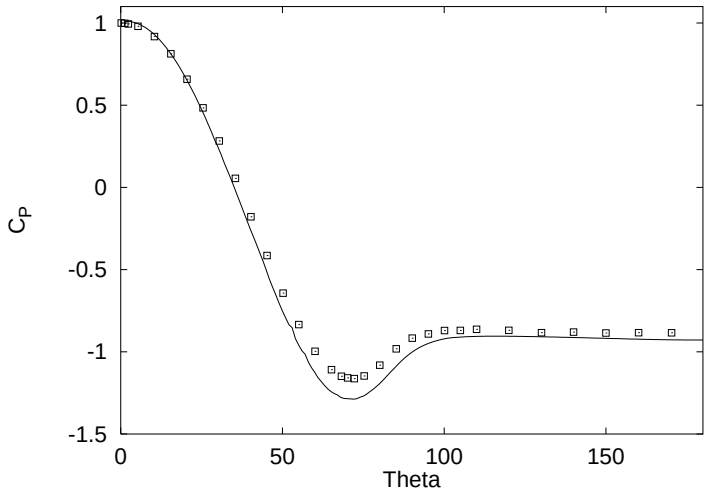

Fig. 3.14: Distribution of the pressure coefficient along the surface of the cylinder. —— Present DNS, Symbols : Experiment of Norberg.

higher values than the experiment and the simulation of Ma et al. [26].

In Figures 3.28, 3.29 and 3.30, the profiles of the shear stress $\overline{uv}$ are presented at the same locations as used in the previous plots. Strikingly good agreement is obtained at locations $x/D = 1.06$ and 1.54 with the data of Lourenco and Shih [24]. At the locations more downstream, the agreement is still quite good.

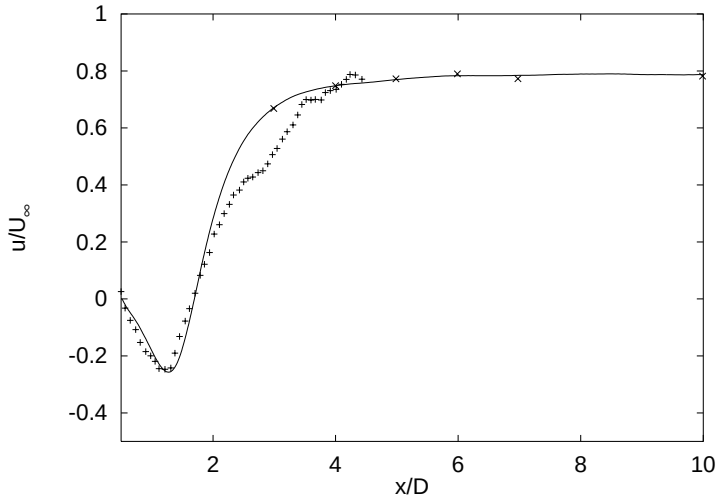

Fig. 3.15: Mean streamwise velocity along the centreline of the cylinder. —— Present DNS, + Lourenco and Shih [24], x Ong and Wallace [35]

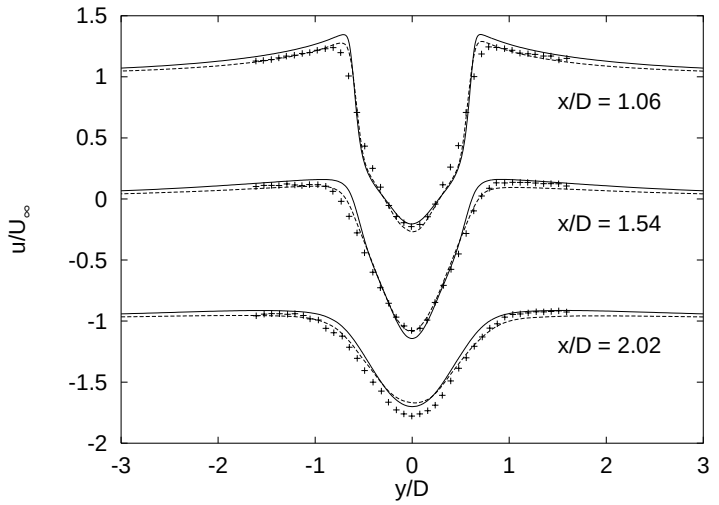

Fig. 3.16: Vertical profiles of the mean streamwise velocity at $x/D = 1.06$, 1.54 and 2.02. —— Present DNS, – – – – Ma et al. [26] , + Lourenco and Shih [24]

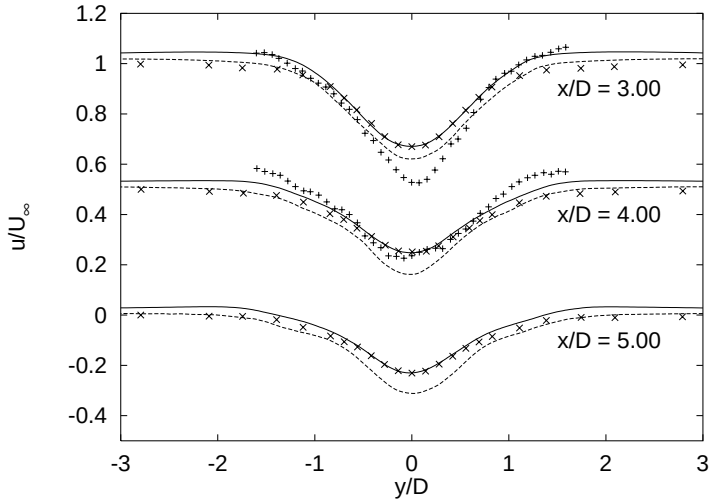

Fig. 3.17: Vertical profiles of the mean streamwise velocity at $x/D = 3.00$, 4.00 and 5.00. —— Present DNS, – – – – Ma et al. [26] , + Lourenco and Shih [24], x Ong and Wallace [35]

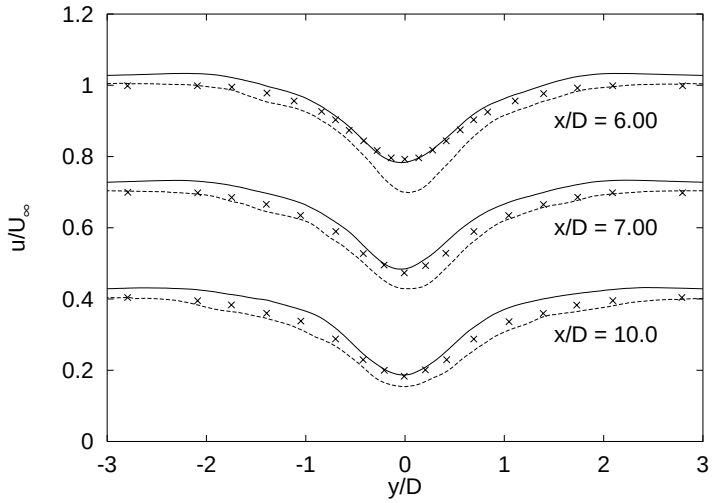

Fig. 3.18: Vertical profiles of the mean streamwise velocity at $x/D = 6.00$, 7.00 and 10.0. —— Present DNS, – – – – Ma et al. [26] , x Ong and Wallace [35]

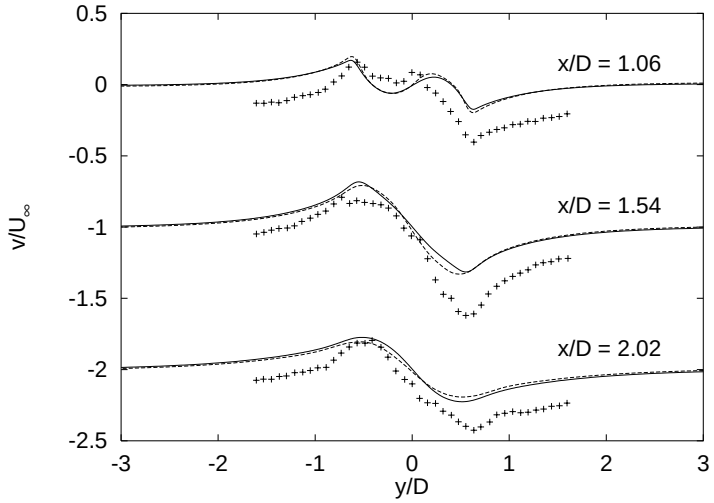

Fig. 3.19: Vertical profiles of the mean vertical velocity at $x/D = 1.06$, 1.54 and 2.02. —— Present DNS, – – – – Ma et al. [26] , + Lourenco and Shih [24]

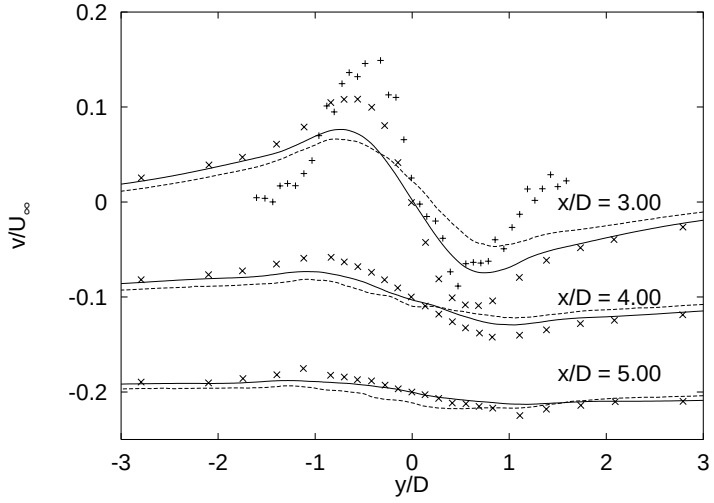

Fig. 3.20: Vertical profiles of the mean vertical velocity at $x/D = 3.00$, 4.00 and 5.00. —— Present DNS, – – – – Ma et al. [26] , + Lourenco and Shih [24], x Ong and Wallace [35]

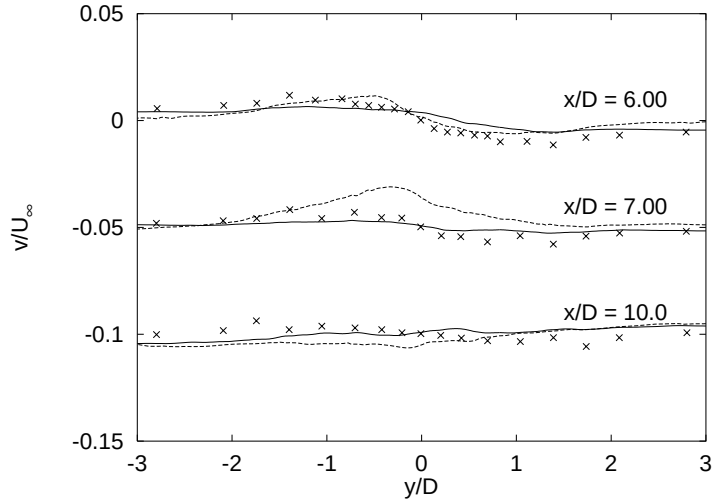

Fig. 3.21: Vertical profiles of the mean vertical velocity at $x/D = 6.00$, 7.00 and 10.0. —— Present DNS, − − − − Ma et al. [26] , x Ong and Wallace [35]

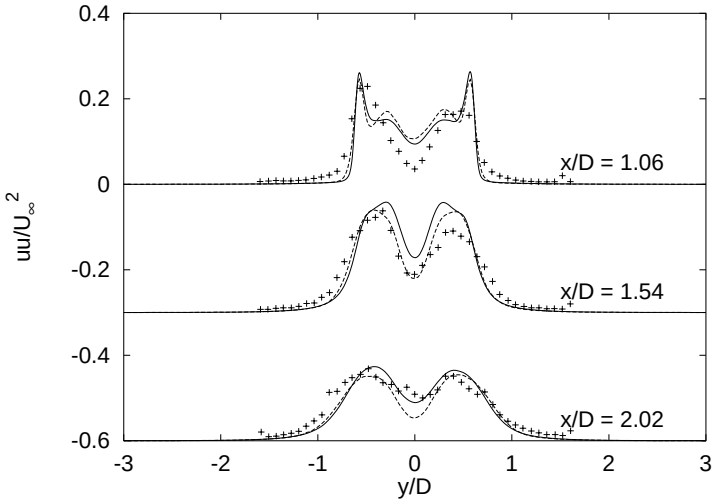

Fig. 3.22: Vertical profiles of the variance of the streamwise velocity fluctuations at $x/D = 1.06$, 1.54 and 2.02.—— Present DNS, − − − − Ma et al. [26], + Lourenco and Shih [24]

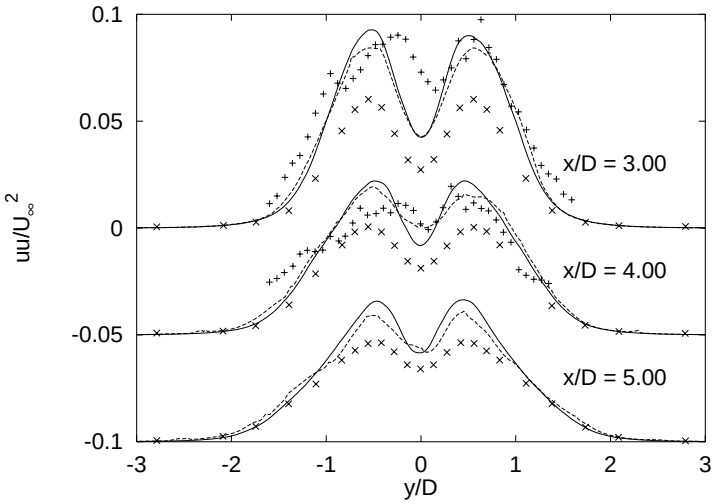

Fig. 3.23: Vertical profiles of the variance of the streamwise velocity fluctuations at $x/D = 3.00$, 4.00 and 5.00. —— Present DNS, – – – – Ma et al. [26] , + Lourenco and Shih [24], x Ong and Wallace [35]

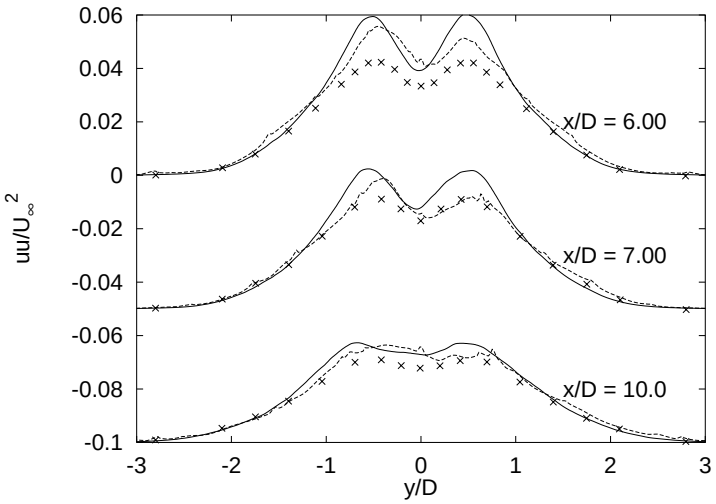

Fig. 3.24: Vertical profiles of the variance of the streamwise velocity fluctuations at $x/D = 6.00$, 7.00 and 10.0. —— Present DNS, – – – – Ma et al. [26] , x Ong and Wallace [35]

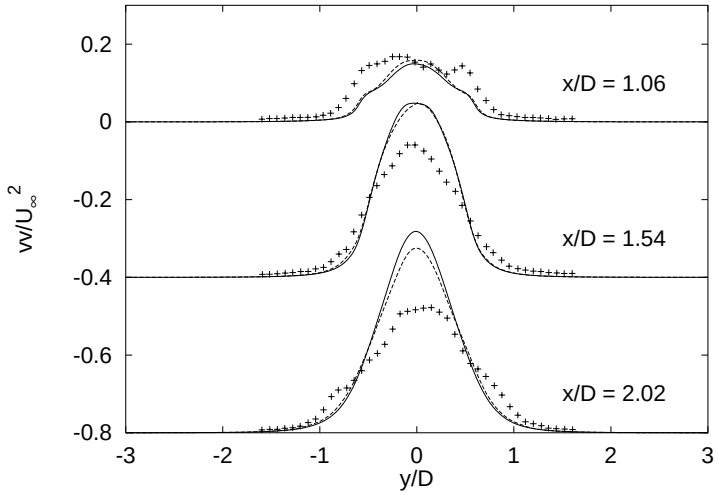

Fig. 3.25: Vertical profiles of the variance of the vertical velocity fluctuations at $x/D = 1.06$, 1.54 and 2.02. —— Present DNS, – – – – Ma et al. [26] , + Lourenco and Shih [24]

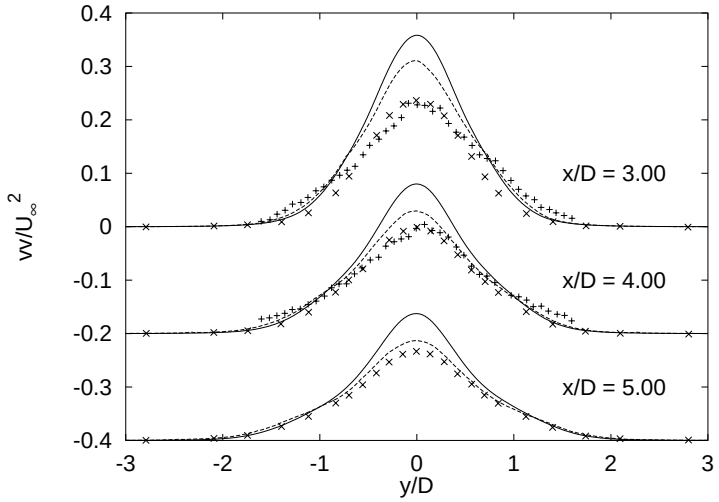

Fig. 3.26: Vertical profiles of the variance of the vertical velocity fluctuations at $x/D = 3.00$, 4.00 and 5.00. —— Present DNS, – – – – Ma et al. [26] , + Lourenco and Shih [24], x Ong and Wallace [35]

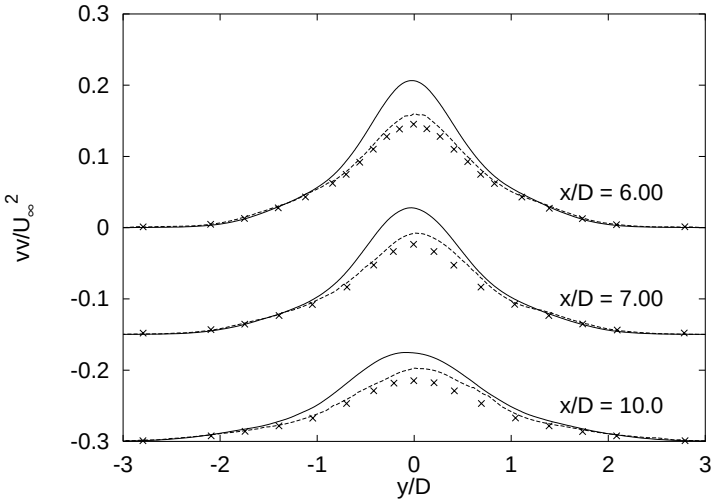

Fig. 3.27: Vertical profiles of the variance of the vertical velocity fluctuations at $x/D = 6.00$, 7.00 and 10.0. —— Present DNS, – – – – Ma et al. [26] , x Ong and Wallace [35]

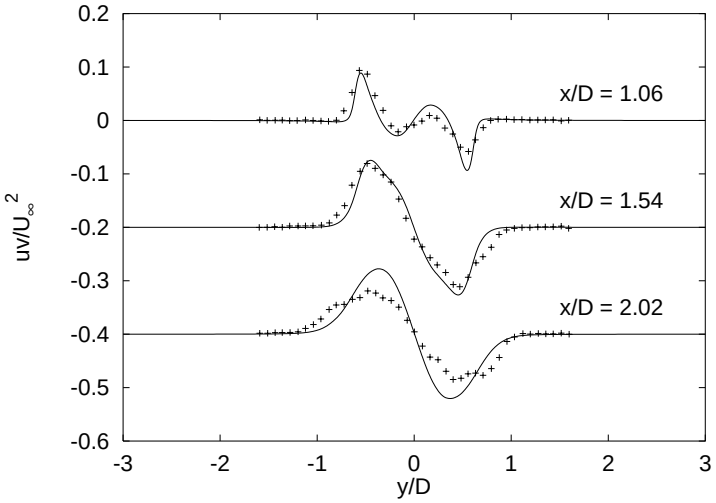

Fig. 3.28: Vertical profiles of the shear stress $\overline{uv}$ at $x/D = 1.06$, 1.54 and 2.02. —— Present DNS, – – – – Ma et al. [26] , + Lourenco and Shih [24]

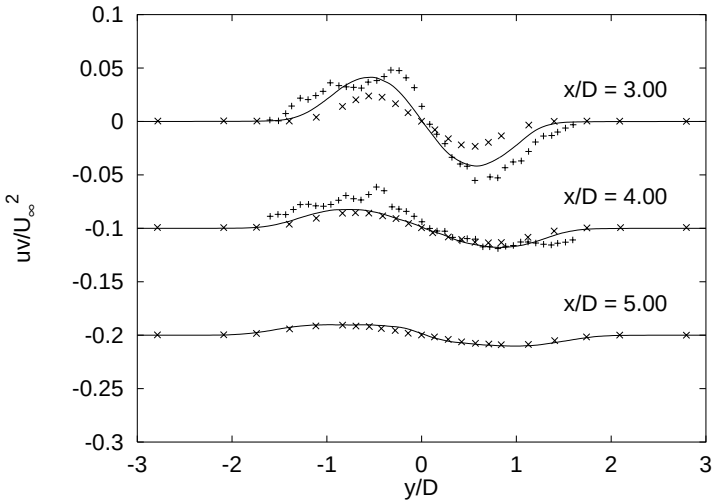

Fig. 3.29: Vertical profiles of the shear stress $\overline{uv}$ at $x/D = 3.00$, 4.00 and 5.00. —— Present DNS , + Lourenco and Shih [24], x Ong and Wallace [35]

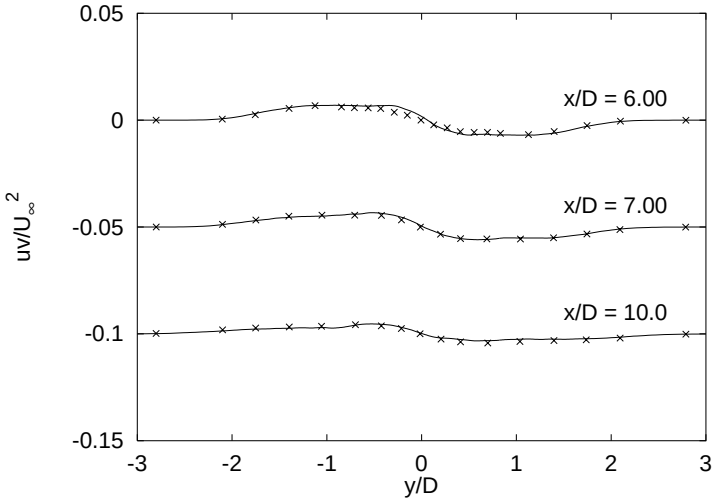

Fig. 3.30: Vertical profiles of the shear stress $\overline{uv}$ at $x/D = 6.00$, 7.00 and 10.0. —— Present DNS, x Ong and Wallace [35]

It is interesting to have a look at the behavior of the second and third invariants of the anisotropy of the Reynolds stress tensor since this tensor and its invariants play an important role in algebraic Reynolds stress modeling. If we define the anisotropy tensor as:

$$b_{ij} = \frac{\overline{u_i u_j}}{2k} - \frac{1}{3}\delta_{ij} \tag{3.9}$$

where $2k = \overline{u_i u_i}$ and δ_{ij} is the Kronecker delta, the second and third invariants read

$$II = -\frac{b_{ij}b_{ji}}{2} \tag{3.10}$$

$$III = \frac{b_{ij}b_{jk}b_{ki}}{6} \tag{3.11}$$

In a plot of II vs III, all possible states of a turbulent flow are constrained to lie in the triangular region shown in Figure 3.31. For a detailed presentation of how this triangle is obtained, the reader is referred to [25]. The point O corresponds to isotropic 3D turbulence, point P represents 2D isotropic turbulence, and finally point Q corresponds to 1D turbulence. Segment 0P is given by the equation $III = -2(-II/3)^{3/2}$ and corresponds to axisymmetric turbulence. Starting from 3D isotropic turbulence, one diagonal component of the Reynolds stress tensor gradually tends toward 0. On segment OQ given by eq. $(III = 2(-II/3)^{3/2})$ we also find axisymmetric turbulence. Segment PQ $(1/9 + 3III + II = 0)$ denotes 2D turbulence. From point P to point Q, one of the two non-zero diagonal components of the Reynolds stress tensor tends to zero. Figures 3.32 to 3.38 show plots of II vs III along vertical coordinates taken at downstream locations ranging from $x/D = 1.06$ to $x/D = 7$. A few selected points are highlighted with symbols in order to help situate the reader. The points chosen are A at $y/D = 2$, B at $y/D = 1$, C at $y/D = 0.5$ and finally G at $y/D = 0$ which lies on the centreline of the wake. Figure 3.32 shows II vs III along a vertical coordinate taken at $x/D = 1.06$. Point A is outside of the wake and although very small Reynolds stresses are observed, the vertical Reynolds stress $\overline{vv}$ dominates slightly over $\overline{uu}$ while $\overline{ww}$ is several orders of magnitude smaller. Complex behavior of the curve is noted between A and D. The curve goes through various stages before it enters the axisymmetric segment OQ and finally reaches quasi-isotropic turbulence on the centreline. In the region further downstream, outside of the mean recirculation bubble where the flow exhibits fully developed turbulence, i.e. $x/D > 2.02$, Figures 3.34 to 3.38 show a very similar behavior of II vs III near the centreline (point D) where the turbulence is axisymmetric.

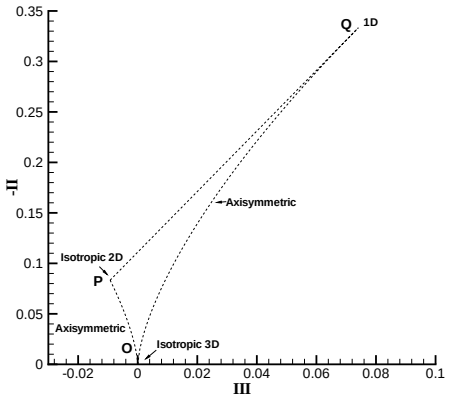

Fig. 3.31: Domain of possible states of $-II$ vs III, the second and third invariants of the anisotropy of the Reynolds stress tensor.

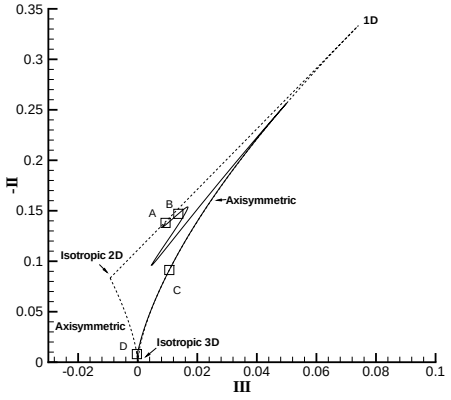

Fig. 3.32: Plot of $-II$ vs III, the second and third invariants of the anisotropy of the Reynolds stress tensor. Values taken along a vertical cut through the wake at $x/D = 1.06$. The symbols serve to highlight the following locations : A $y/D = 2$, B $y/D = 1$, C $y/D = 0.5$, D $y/D = 0$.

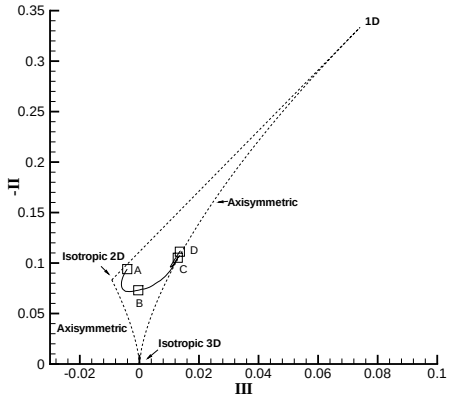

Fig. 3.33: Plot of $-II$ vs III, the second and third invariants of the anisotropy of the Reynolds stress tensor. Values taken along a vertical cut through the wake at $x/D = 2.02$. Symbols as on Figure 3.32.

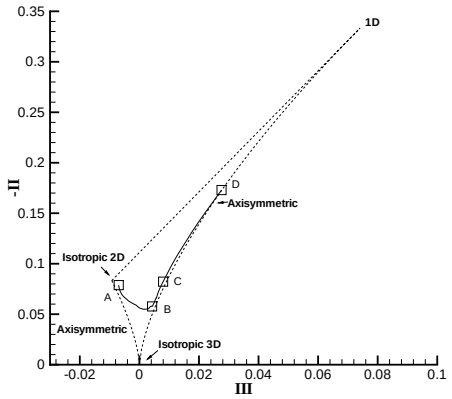

Fig. 3.34: Plot of $-II$ vs III, the second and third invariants of the anisotropy of the Reynolds stress tensor. Values taken along a vertical cut through the wake at $x/D = 3.00$. Symbols as on Figure 3.32.

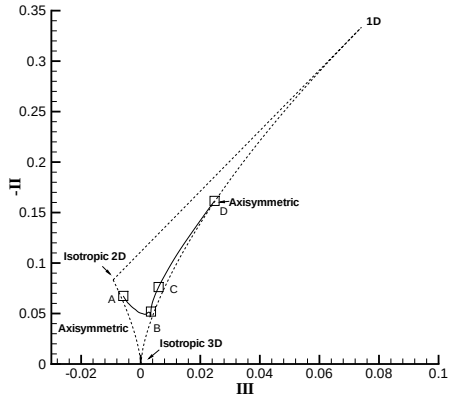

Fig. 3.35: Plot of $-II$ vs III, the second and third invariants of the anisotropy of the Reynolds stress tensor. Values taken along a vertical cut through the wake at $x/D = 4.00$. Symbols as on Figure 3.32.

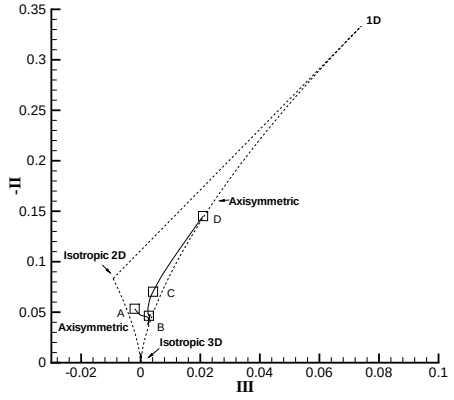

Fig. 3.36: Plot of $-II$ vs III, the second and third invariants of the anisotropy of the Reynolds stress tensor. Values taken along a vertical cut through the wake at $x/D = 5.00$. Symbols as on Figure 3.32.

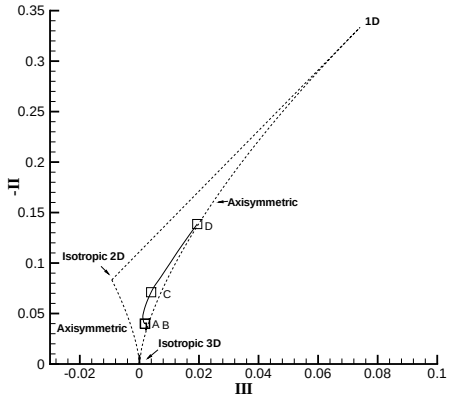

Fig. 3.37: Plot of $-II$ vs III, the second and third invariants of the anisotropy of the Reynolds stress tensor. Values taken along a vertical cut through the wake at $x/D = 6.00$. Symbols as on Figure 3.32.

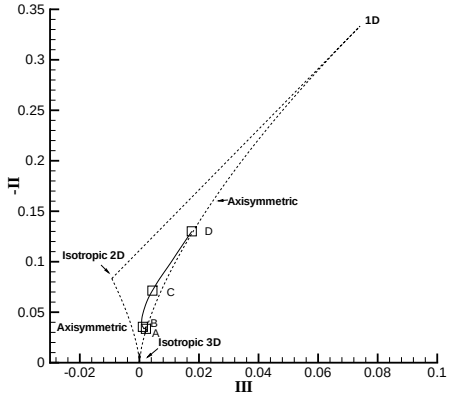

Fig. 3.38: Plot of $-II$ vs III, the second and third invariants of the anisotropy of the Reynolds stress tensor. Values taken along a vertical cut through the wake at $x/D = 7.00$. Symbols as on Figure 3.32.

3.4 Frequency spectra

To gain further insight into the turbulence structure in the wake of the cylinder, frequency spectra are computed from the DNS data. Over a period of time $T = 90D/U_\infty$, 8490 samples were gathered along the centreline of the cylinder at 4 downstream locations, $x/D = 3.00$, $x/D = 5.00$, $x/D = 7.00$ and $x/D = 10.0$. Frequency spectra of velocity fluctuations were computed via the Lomb periodogram technique [38]. All points in the spanwise direction were treated as independant realizations and used to average the spectra. The spectra are compared to those obtained experimentally by Ong and Wallace [35].

At $x/D = 3.00$, Figures 3.39 and 3.40 show the frequency spectra of the streamwise and vertical velocity fluctuations, respectively. At the lower frequencies, the level of energy is predicted in accordance with the experiment while at the higher frequencies a slightly higher level is seen. The experiments might have had difficulties to capture the highest frequencies. In Figure 3.40, the strong peak at the Strouhal frequency is well reproduced. A second weaker peak at $\omega/\omega_{St} = 3.0$ appears on both sets of data. It should be kept in mind that the primary frequency which is due to vortex shedding appears at twice the Strouhal frequency in the streamwise velocity fluctuations (Fig. 3.39). In both figures, an extended inertial range where energy cascades following a $-5/3$ slope is observed.

Figures 3.41 and 3.42 show the frequency spectra at $x/D = 5.00$. Very good agreement is observed with the experiment. In Figure 3.42, the two peaks are still visible. Again the spectra show an extended inertial range.

Figures 3.43 and 3.44 present the frequency spectra at $x/D = 7.00$. Again the agreement is good. The inertial range now encompasses a reduced portion of the spectrum.

Finally, in Figures 3.45 and 3.46 the frequency spectra are plotted at the last position, $x/D = 10.0$. At the higher frequencies, the DNS now shows lower level of energy. This most certainly results from an underresolution of the simulation in this area. It is estimated that 20 to 50 grid points per diameter would be needed to properly resolve all the flow features. In any case, one can conservatively conclude that up to $x/D = 7.00$, our DNS data is reliable.

One-dimensional wavenumber power spectra were also computed in the homogeneous spanwise direction. They provide valuable informations about the resolution requirements in this direction. The spectra of velocity fluctuations have been obtained by Fourier transforming the instantaneous velocity

components and multiplying Fourier coefficients with their complex conjugate and summing over all these products. Time averaging of the spectra was performed to obtain smooth curves. Figures 3.47 and 3.48 show the spectra for different streamwise positions of the streamwise and vertical velocity fluctuations, respectively. Between 2.5 and 3 orders of magnitude of energy decay is observed from the low to the high wavenumbers.

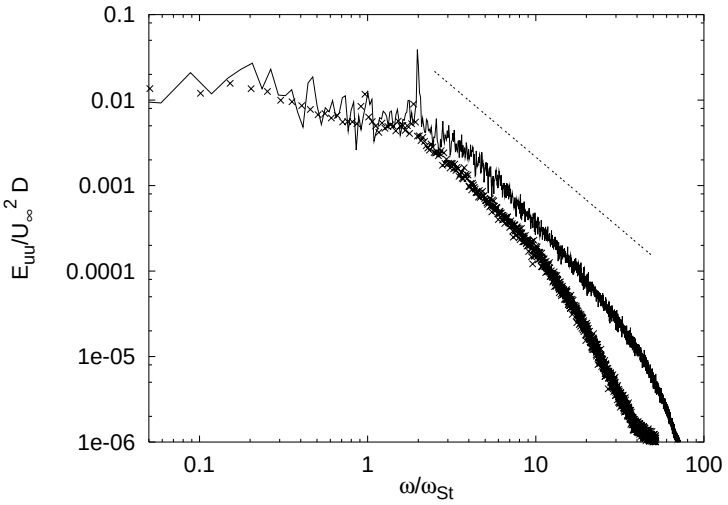

Fig. 3.39: Frequency spectrum of the streamwise velocity fluctuations at $x/D = 3.00$. ——— Present DNS, x Ong and Wallace [35]

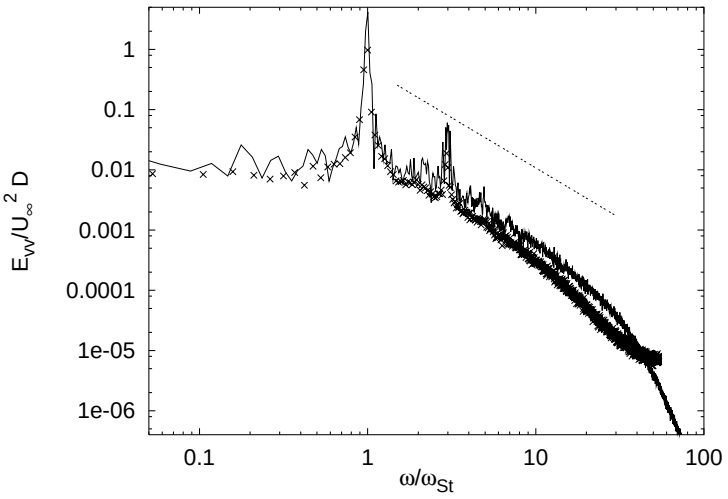

Fig. 3.40: Frequency spectrum of the vertical velocity fluctuations at $x/D = 3.00$. ——— Present DNS, x Ong and Wallace [35]

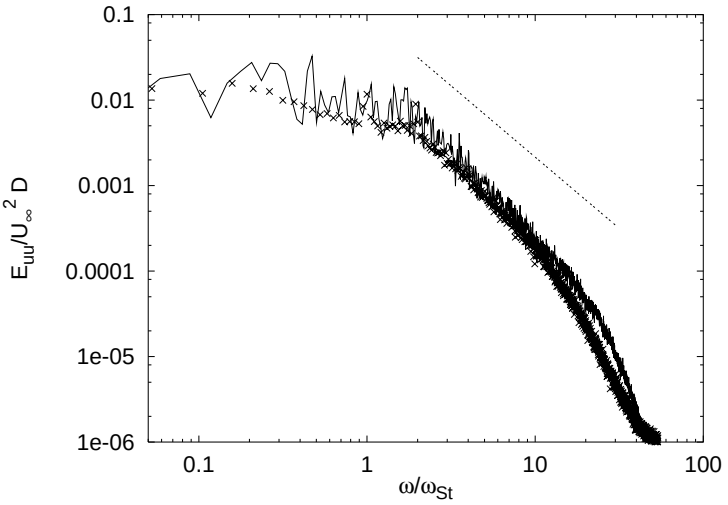

Fig. 3.41: Frequency spectrum of the streamwise velocity fluctuations at $x/D = 5.00$. —— Present DNS, x Ong and Wallace [35]

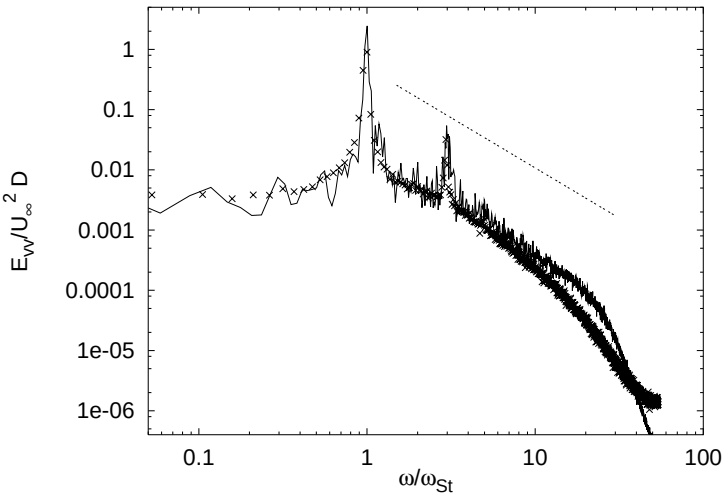

Fig. 3.42: Frequency spectrum of the vertical velocity fluctuations at $x/D = 5.00$. —— Present DNS, x Ong and Wallace [35]

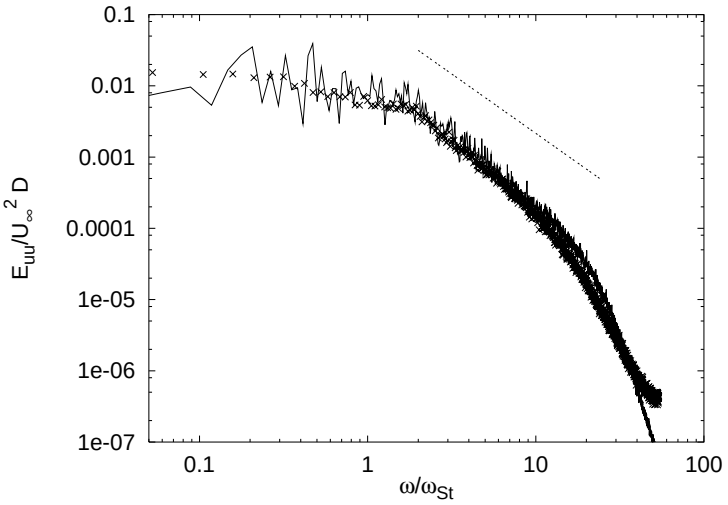

Fig. 3.43: Frequency spectrum of the streamwise velocity fluctuations at $x/D = 7.00$. ——— Present DNS, x Ong and Wallace [35]

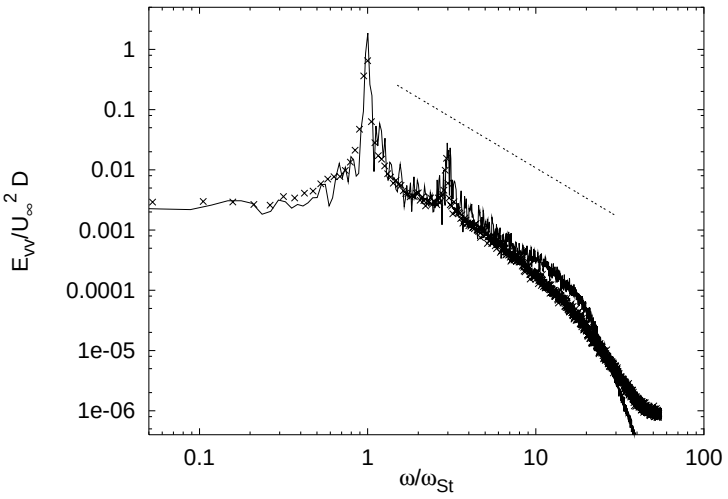

Fig. 3.44: Frequency spectrum of the vertical velocity fluctuations at $x/D = 7.00$. ——— Present DNS, x Ong and Wallace [35]

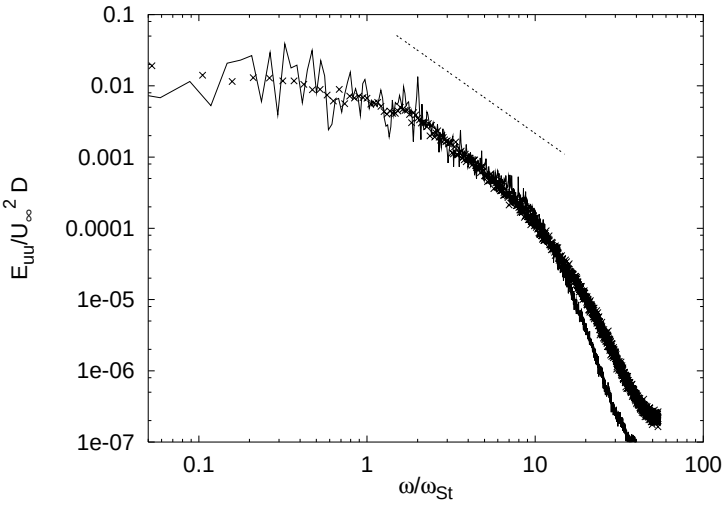

Fig. 3.45: Frequency spectrum of the streamwise velocity fluctuations at $x/D = 10.0$. —— Present DNS, x Ong and Wallace [35]

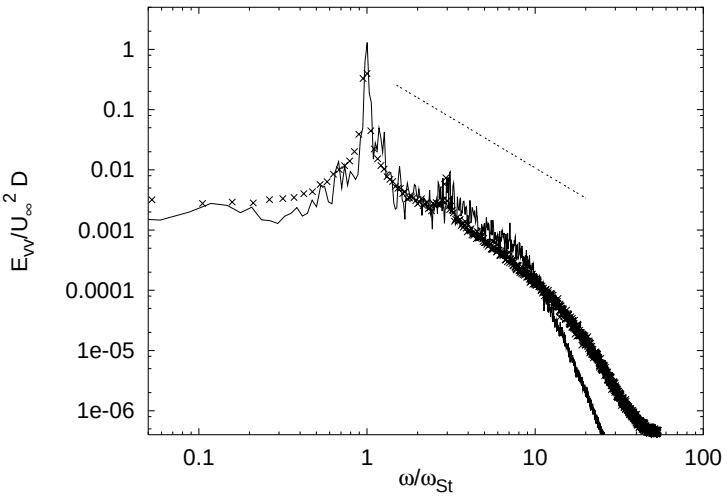

Fig. 3.46: Frequency spectrum of the vertical velocity fluctuations at $x/D = 10.0$. —— Present DNS, x Ong and Wallace [35]

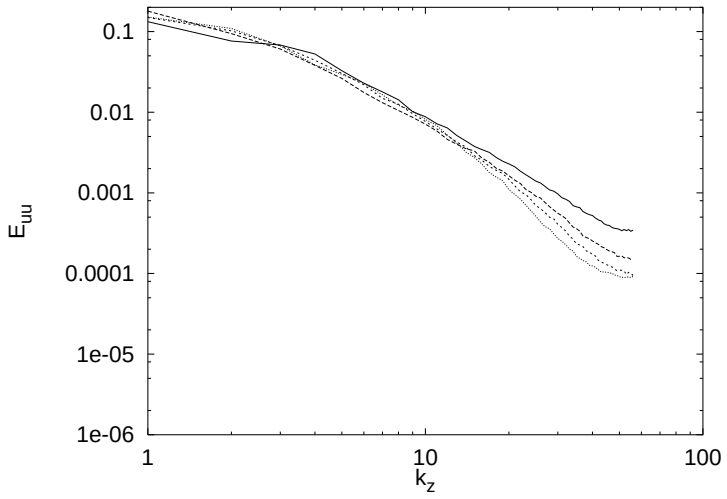

Fig. 3.47: 1D wavenumber spectra of the streamwise velocity fluctuations in the spanwise direction. —— $x/D = 3.00$, – – – – $x/D = 5.00$, - - - - $x/D = 7.00$, ····· $x/D = 10.0$

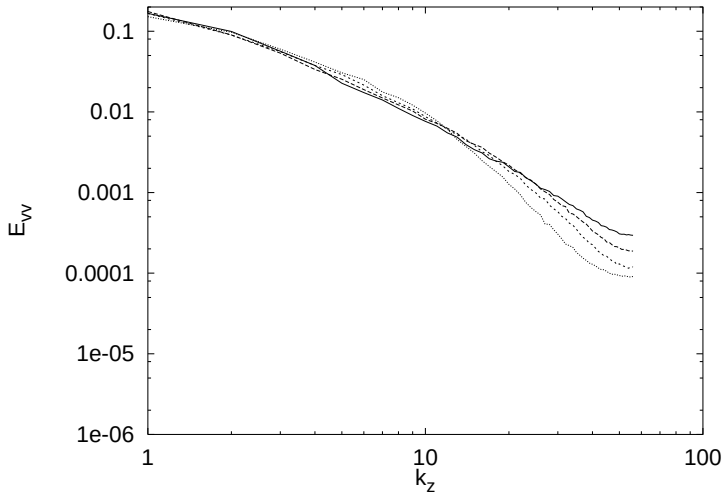

Fig. 3.48: 1D wavenumber spectra of the vertical velocity fluctuations in the spanwise direction. —— $x/D = 3.00$, – – – – $x/D = 5.00$, - - - - $x/D = 7.00$, ····· $x/D = 10.0$

4. LES of the flow around a circular cylinder at Re = 3900

In this chapter, LES results of the flow around a circular cylinder at $Re = 3900$ are reported for different SGS models and grid resolutions. They are compared to DNS data presented in the previous chapter. In addition, comparisons with numerical simulations and experiments, performed by other authors, are also provided and discussed in detail.

4.1 Computational details

The computational domain and boundary conditions were set identically equal to those of the DNS presented in the previous chapter and are repeated here. The computational domain is 20 diameters D long in the streamwise x-direction, with the center of the cylinder being $5D$ downstream of the inflow plane. In the normal y-direction, the domain size is also $20D$. The spanwise extent of the domain was chosen to be $L_z = \pi D$, which corresponds to the size used by most previous authors. The boundary conditions prescribed in the present simulations are a uniform, unperturbed inflow velocity and periodic velocity components in the normal and spanwise directions. A zero-gradient outflow condition holds at $x = 15D$.

Recently, Ma et al. [26] pointed out the fact that a small spanwise computational domain like πD or a high dissipation LES favor U-shape rather than the V-shape streamwise velocity profiles that were also observed in PIV-experiments of Lourenco anf Shih [24] in the near wake ($x/D = 1.06$). We will show later that such a discrepancy in the near wake region is largely explained by differences in the prediction of the mean recirculation bubble which are sometimes due to an insufficient averaging time.

Two meshes with different resolutions, $7.7 \cdot 10^6$ (case LES1) and $2.4 \cdot 10^6$ (case LES2) cells have been used to investigate the grid independence of the solution. The total number of cells N_x, N_y, N_z in (x,y,z)-directions is summarized in Table 4.1. This table also contains the number of cells D_x,

Case	N_xxN_yxN_z	D_xxD_y	$(\frac{\Delta x_{i+1}-\Delta x_i}{\Delta x_i}) \times 100$	$(\frac{\Delta y_{j+1}-\Delta y_j}{\Delta y_j}) \times 100$
LES1	376x320x64	100x100	1.4	2.5
LES2	250x200x48	60x70	3.1	5.6
Present DNS	706x594x112	150x190	0.5	1.4

Tab. 4.1: Computational parameters

D_y taken to discretize the square DxD which contains the cylinder. The last two columns represent the grid stretching factors. The corresponding data of the DNS presented earlier are included for comparison.

Three different computations were performed. In LES1, the Smagorinsky sgs model was used with a coefficient of 0.1 and a length scale $\Delta = (\Delta_x \Delta_y \Delta_z)^{1/3}$, but no wall damping (LES1 smago). For comparison, the dynamic Smagorinsky model of Germano et al. [13] with Lilly's modification [23] was applied on grid LES1 (LES1 dyn). On grid LES2, only the Smagorinsky model was used (LES2 smago). Both models are described in Chapter 1.

4.2 Instantaneous flow field

Figure 4.1 shows instantaneous isosurfaces of a specific pressure fluctuation ($P'/0.5\rho {U_\infty}^2 = -0.5$) for DNS and LES1 smago computations. The large vortical structures (rollers) and the braids, are easily identified. The LES simulation is able to capture such phenomena, but looses the finer scales as can be seen from the DNS data. Further in the wake, Figure 4.2, the Kármán vortex street is mostly two-dimensional.

In Figure 4.3, instantaneous isosurfaces of a specific value of Q are shown, together with isosurfaces of a pressure fluctuation. It is encouraging to note the similarities of this figure with Figure 3.10, which shows the same quantities but for the DNS. The same streamwise structures in the near wake are present, but bigger in the LES when compared to the DNS, an effect of the difference in spatial resolution.

4.3 First and second order statistics

All the flow statistics of the LES and DNS have been accumulated over 300 problem times tU_∞/D which corresponds to approximately 60 vortex shedding cycles. In Table 4.2, the comparison of flow parameters starts

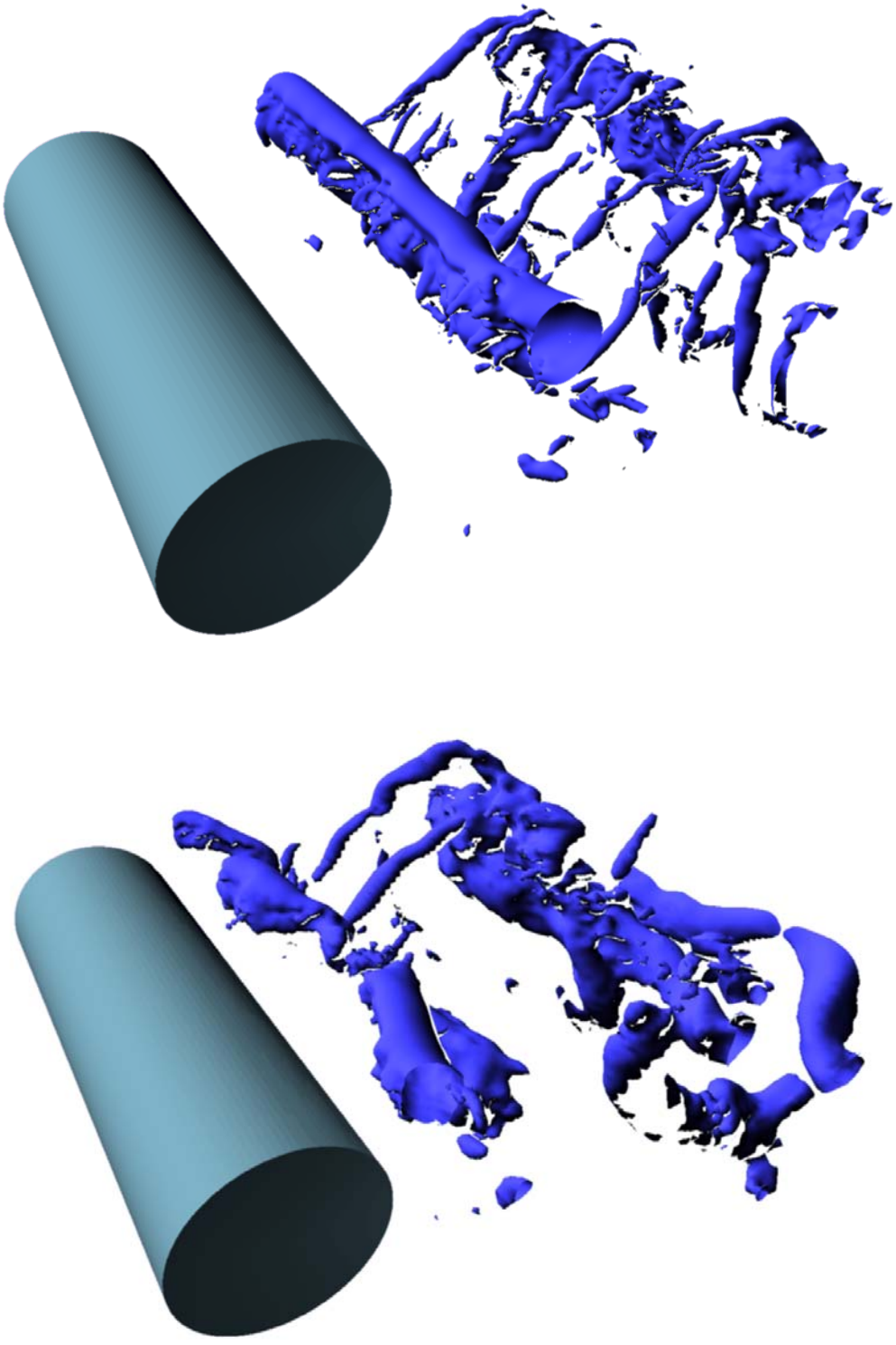

Fig. 4.1: Isosurfaces of a specific pressure fluctuation ($P'/0.5\rho {U_\infty}^2 = -0.5$), (top/bottom: DNS/LES1 smago). Perspective view.

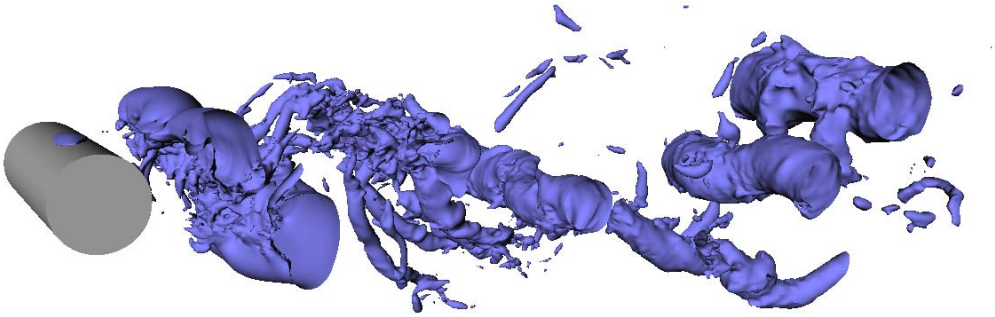

Fig. 4.2: Isosurfaces of a specific pressure fluctuation ($P'/0.5\rho {U_\infty}^2 = -0.5$), (LES1 smago)

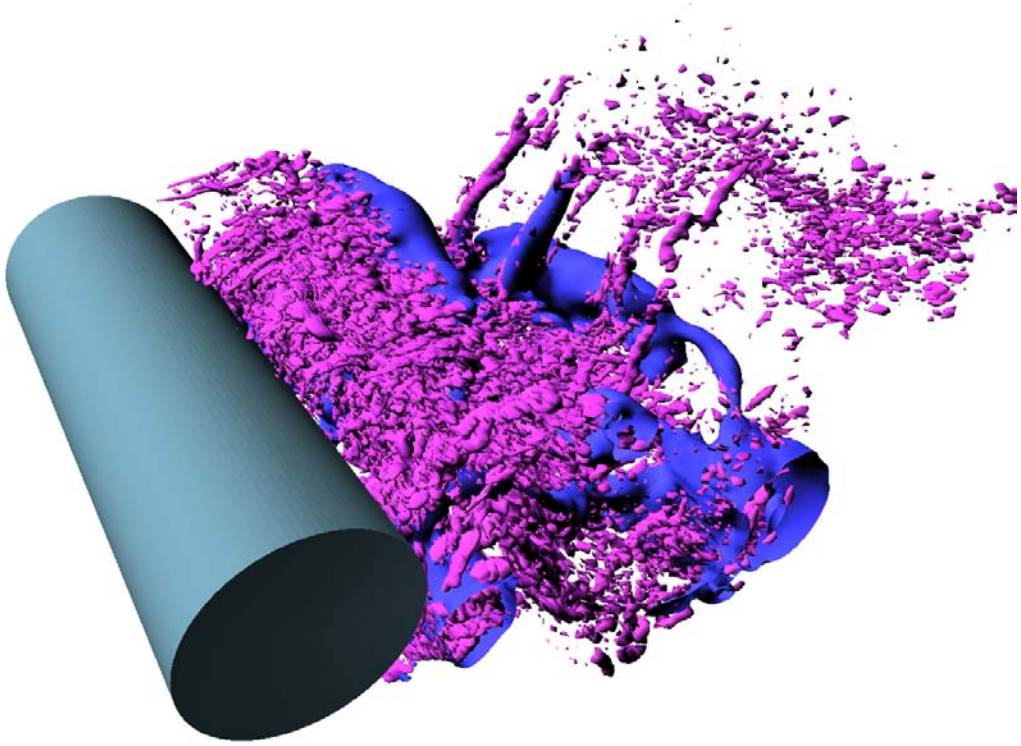

Fig. 4.3: Isosurfaces of a specific pressure fluctuation $P'/\frac{1}{2}\rho U_\infty^2 = -0.5$, darker gray, and of $Q = 25.0$, lighter gray. (LES1 smago).

Data from	C_D	C_{Pb}	Θ_{sep}	L_r/D	St
exp	0.99 ± 0.05	-0.88 ± 0.05	86 ± 2	1.4 ± 0.1	0.215 ± 0.005
DNS [26], Case I	-	-0.96	-	1.12	0.203
Present DNS	1.03	-0.93	85.7	1.30	0.220
Kravchenko(LES)	1.04	-0.94	88.0	1.35	0.210
LES1 smago	1.14	-0.99	87.3	1.04	0.210
LES1 dyn	1.15	-0.98	86.5	1.02	0.215
LES2 smago	1.31	-1.13	90.0	0.81	0.210

Tab. 4.2: Mean flow parameters from DNS/LES and experiments (taken from [20],[21])

with the mean drag coefficient C_D, the base pressure coefficient C_{Pb}, then proceeds to the separation angle Θ_{sep}, the length of the mean recirculation region and the Strouhal shedding frequency St. Three different LES, the LES of Kravchenko and Moin [21], case 2, the DNS of Ma et al. [26], case I, and our own DNS are contrasted. The coarse grid computation together with the Smagorinsky model (LES2 smago) provides the poorest results. On the fine grid, the difference between both sgs models is unimportant. The separation angle and the shedding frequency agree well with the experimental data. For the drag coefficient and the base pressure coefficient the agreement is fair. The length of the mean recirculation region, L_r, however, appears to be too small.

Figure 4.4 shows the streamlines of the mean velocity field. We again notice the shortening of the recirculation length obtained by our LES computations as compared to the DNS result. Also worth mentioning is a secondary recirculation bubble which was seen only on an instantaneous flow field in the DNS, but now appears in the mean for the LES. A correlation is observed between the strength of the secondary recirculation and the length of the primary recirculation which is affected by the decrease in resolution on one side and the amount of low-pass filtering on the other. Similar secondary recirculations were reported in the LES studies of Breuer [4] and Fröhlich et al. [12]. Experimental studies reported that such regions occur around $Re = 5000$, which is physically consistent with the present simulations which predicted earlier transition of the shear layers accompanied by shorter recirculation bubbles and lower base pressure coefficients. These trends are typical for Reynolds numbers higher than 3900.

Figure 4.5 compares isolines of the mean streamwise velocity of the DNS, LES1 dyn and LES2 smago. We note once again the shorter recirculation bubble of the two LES computations. Shorter shear layers are also noted.

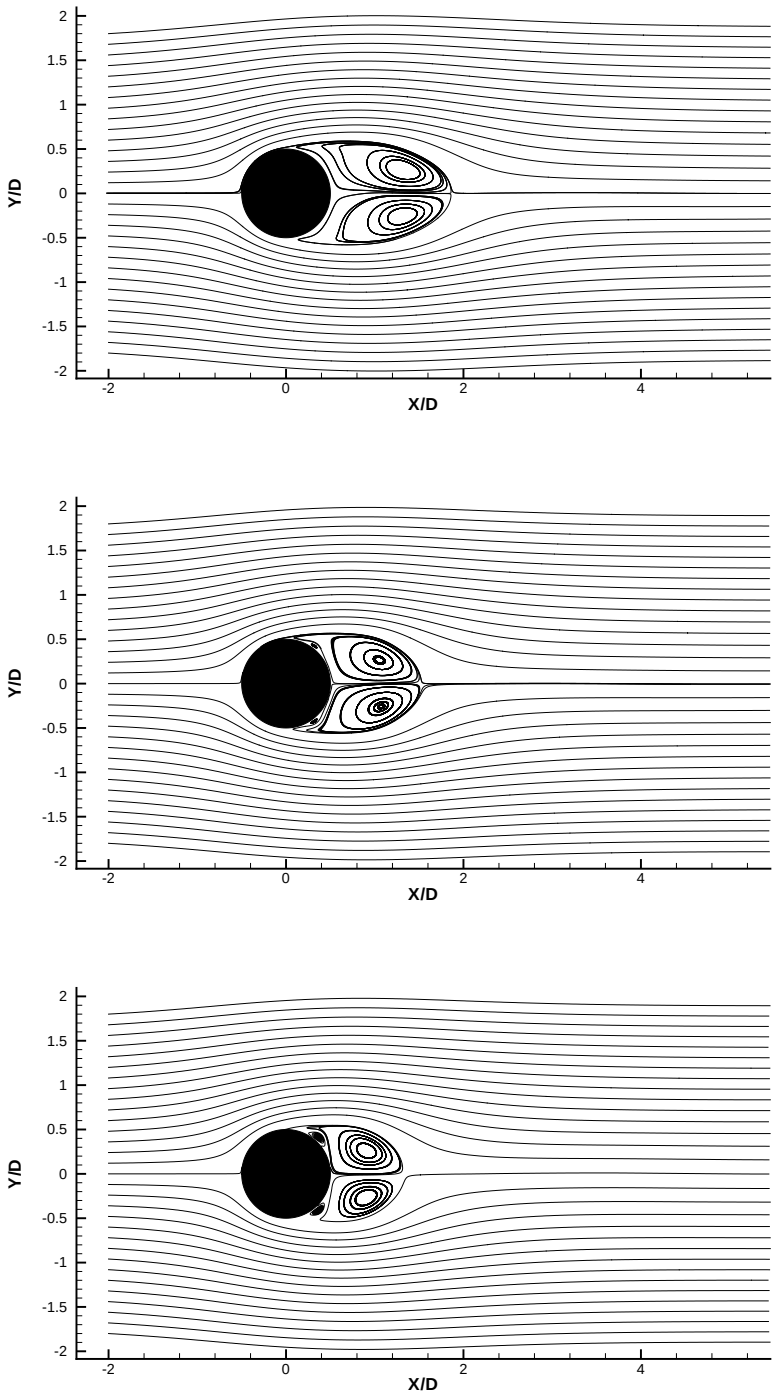

Fig. 4.4: Mean streamlines of the flow around the cylinder. Top: DNS, Middle: LES1 dyn, bottom LES2 smago.

In the LES, the formation length of the wake vortices is also shorter as illustrated by Figure 4.6 which shows contour lines of the RMS streamwise velocity fluctuations. The two peaks associated with the vortex formation, as shown in the previous chapter, are closer to the cylinder. The peaks present in the vertical and spanwise velocity fluctuations, as seen in Figures 4.7 and 4.8, are shifted closer to the cylinder, which is also a consequence of the shorter recirculation regions obtained in the LES. Wiggles resulting from the use of coarse grids are clearly visible in Figure 4.7.

Figure 4.9 presents the distribution of the pressure coefficient along the surface of the cylinder. LES1 dyn and LES1 smago provide very similar solutions, in fair agreement with the DNS and with the experiment of Norberg [34]. LES2 smago is in good agreement with the other numerical simulations on the front part of the cylinder, but gives a lower pressure coefficient toward the rear of the cylinder.

Figure 4.10 shows the mean streamwise velocity in the symmetry plane of the cylinder wake. The maximum backflow velocity is fairly well predicted in all cases, especially by the DNS. The underprediction of the recirculation length L_r by all LES runs is obvious and has been documented in Table 4.2. The plateau in the data of Lourenco and Shih [24] for $x \geq 3D$ has already been discussed in the previous chapter. Figures 4.11 to 4.13 show the mean streamwise velocity profiles taken along vertical coordinates through the wake at positions ranging from $x/D = 1.06$ to 10. In the near wake, (Figure 4.11), at $x/D = 1.06$, the LES predicts more pronounced V-shape profiles than the DNS. Downstream of $x/D = 3.0$, see Figures 4.12 and 4.13, the recovery of the centreline velocity is retarded for the LES data, especially for LES2 smago. The results of LES1 dyn and LES1 smago are nearly identical and both show fair agreement with the DNS data. In Figures 4.14 to 4.16, the mean vertical velocity profiles taken at the same positions as described above, are shown. The overall agreement is good for computations LES1 dyn and LES1 smago, while LES2 smago gives the poorest predictions.

The variance of the streamwise velocity fluctuations is shown in Figures 4.17 to 4.19. Although at $x/D = 1.06$, Figure 4.17, all the LES data predict higher peaks, at the locations downstream the overall agreement with the experiment is quite acceptable. We note no clear superiority of one of the two computations LES1 dyn and LES1 smago. The Smagorinsky model gives slightly better predictions in the near wake, i.e. $x/D = 1.54$, 2.02, while more downstream the dynamic model behaves somewhat better. The variances of the vertical velocity fluctuations are presented in Figures 4.20 to 4.22. After exhibiting much higher peaks than the DNS at $x/D = 1.06$

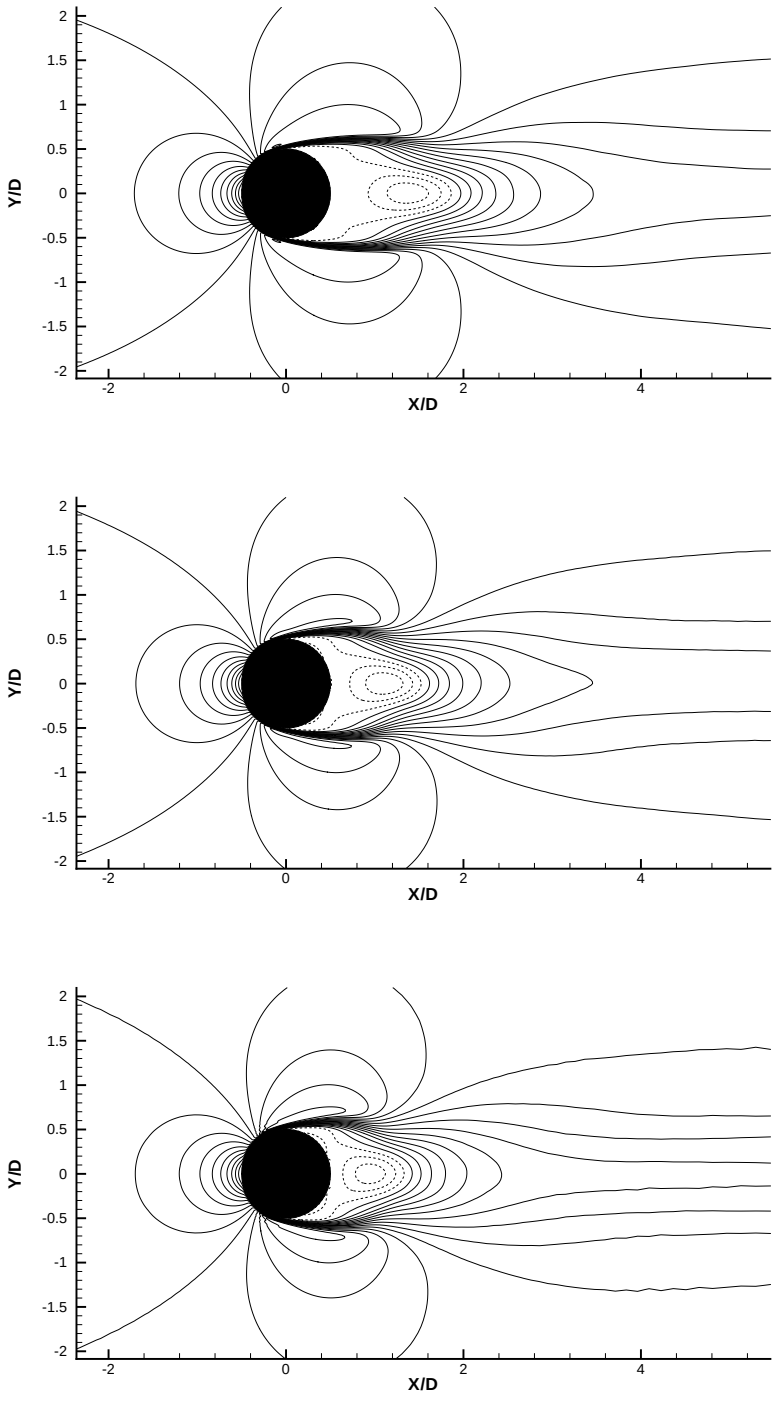

Fig. 4.5: Contours of mean streamwise velocity. Top: DNS, Middle: LES1 dyn, bottom LES2 smago. $\bar{u}/U_\infty = -0.2$ to 1.4, 17 levels.

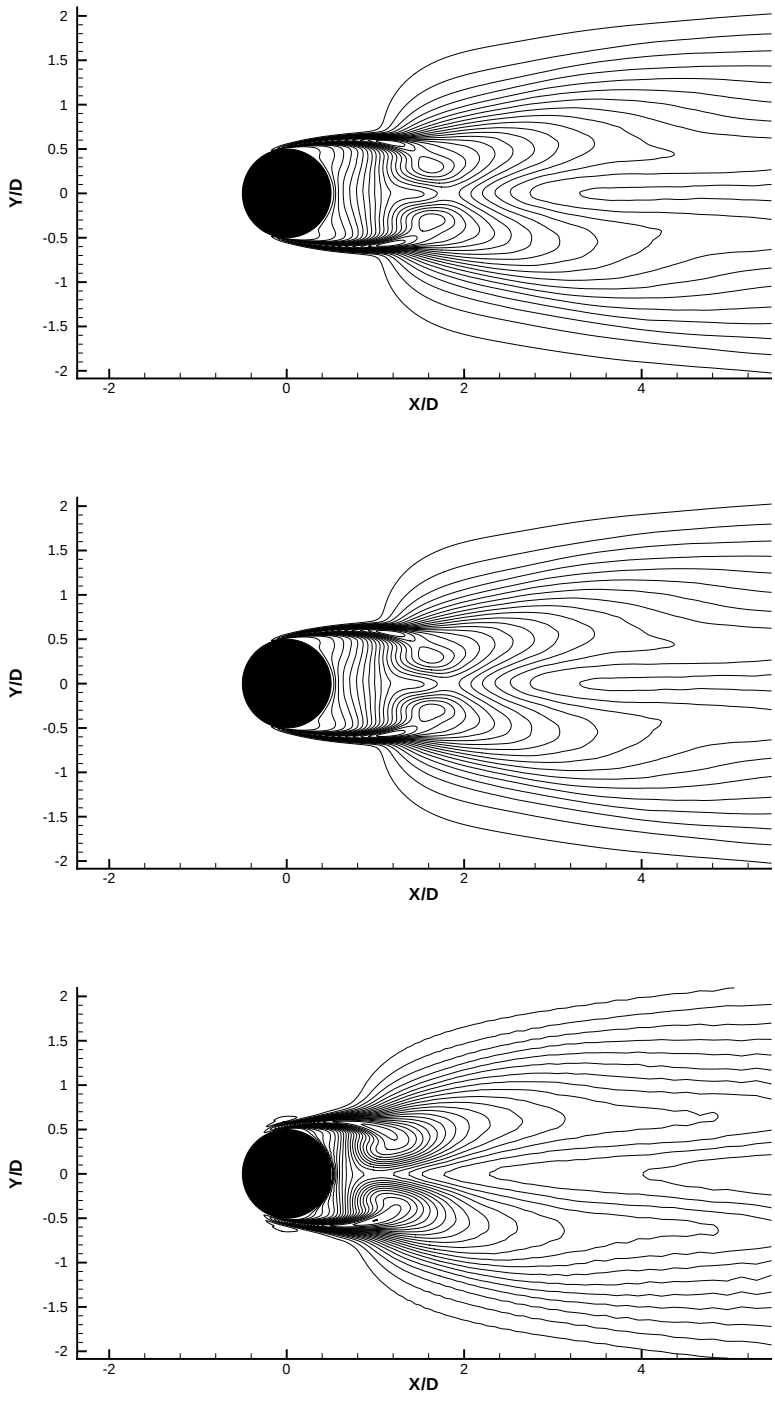

Fig. 4.6: Contours of RMS streamwise velocity fluctuation. Top: DNS, Middle: LES1 dyn, bottom LES2 smago. $u'/U_\infty = 0$ to 0.7, 29 levels.

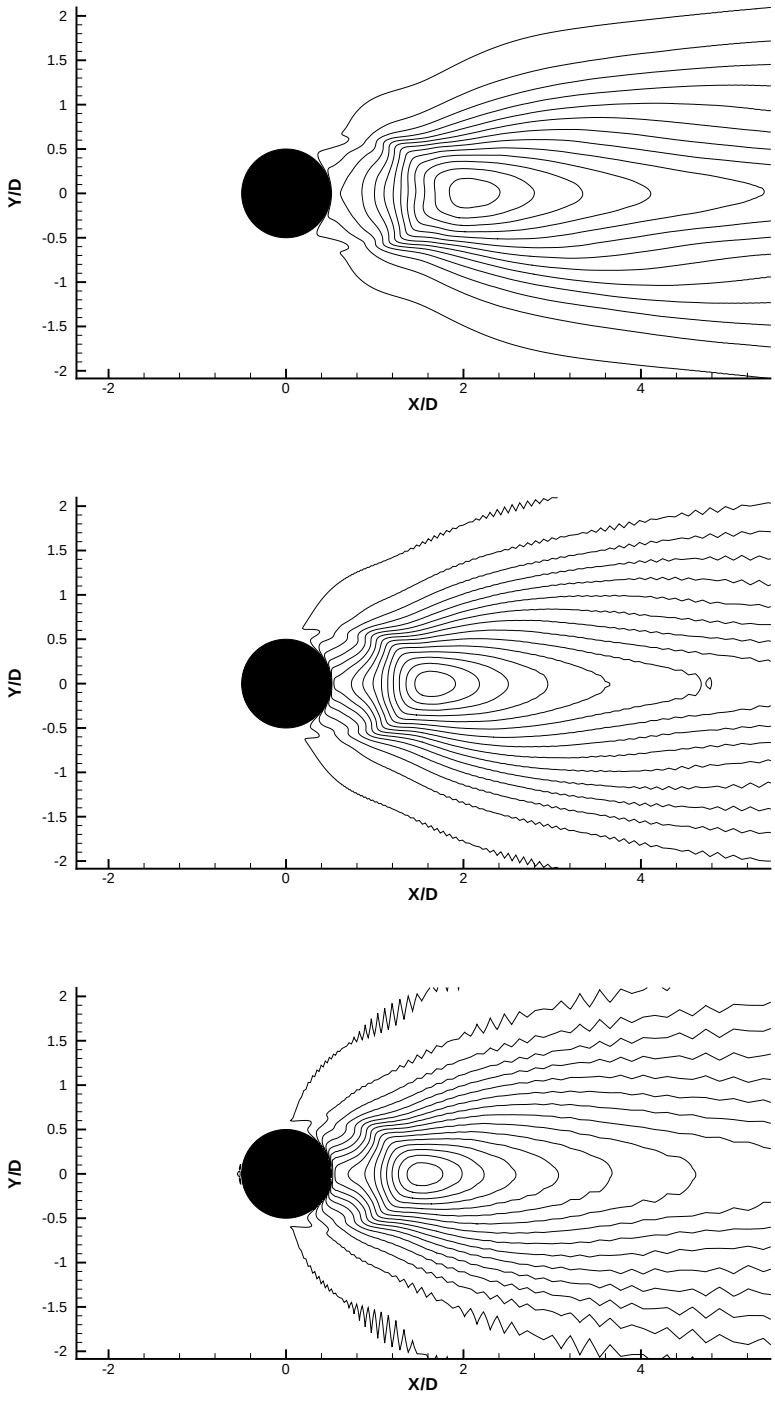

Fig. 4.7: Contours of RMS vertical velocity fluctuation. Top: DNS, Middle: LES1 dyn, bottom LES2 smago. $v'/U_\infty = 0$ to 1.0, 21 levels.

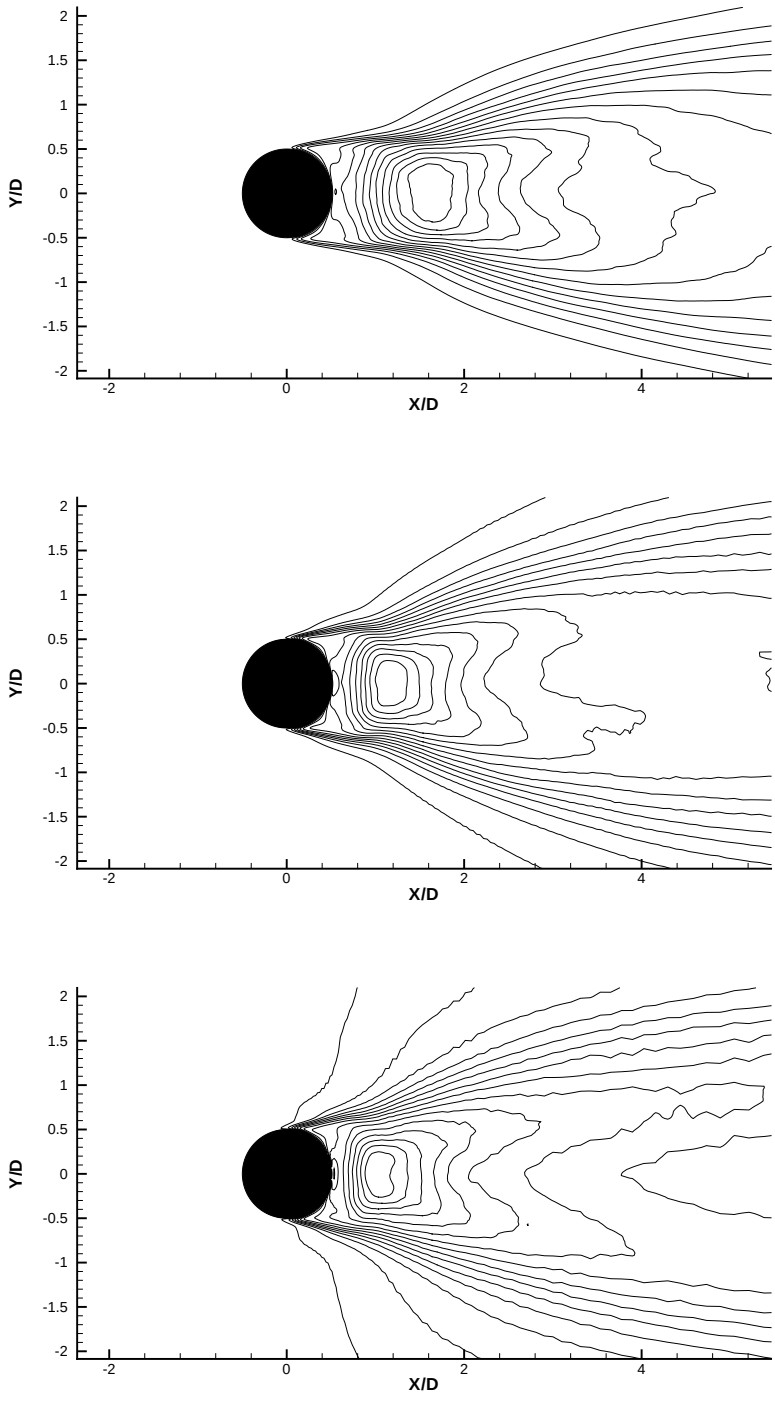

Fig. 4.8: Contours of RMS spanwise velocity fluctuation. Top: DNS, Middle: LES1 dyn, bottom LES2 smago. $w'/U_\infty = 0$ to 0.4, 21 levels.

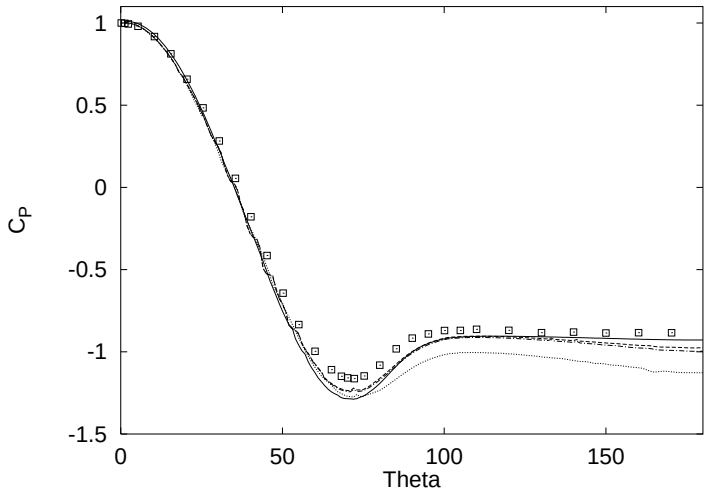

Fig. 4.9: Distribution of the pressure coefficient along the surface of the cylinder. —— DNS, — · — LES1 smago, – – – – LES1 dyn, ····· LES2 smago, + experiment of Lourenco and Shih [24], Symbols are the experiment of Norberg

and $x/D = 1.54$, all LES come closer to the DNS on the centreline $y/D = 0$ further downstream. The width of the wake, however, is overpredicted by all LES, LES2 smago showing once again the poorest results. We note in Figure 4.21 the excellent agreement between LES1 dyn and DNS in the mid-wake. This is practically the only plot where a significant difference is observed between LES1 dyn and LES1 smago.

Vertical profiles of the Reynolds shear stress $\bar{uv}$ are shown in Figures 4.23 to 4.25. At $x/D = 1.06$ and $x/D = 1.54$, all LES computations show higher peaks than the DNS and the experiment. Further downstream, all the LES data provide good predictions, most probably due to a compensation of model and resolution effects. At $x/D = 2.02$, the excellent agreement of LES2 smago with the experiment is merely a coincidence. Overall LES1 dyn and LES1 smago provide the best predictions.

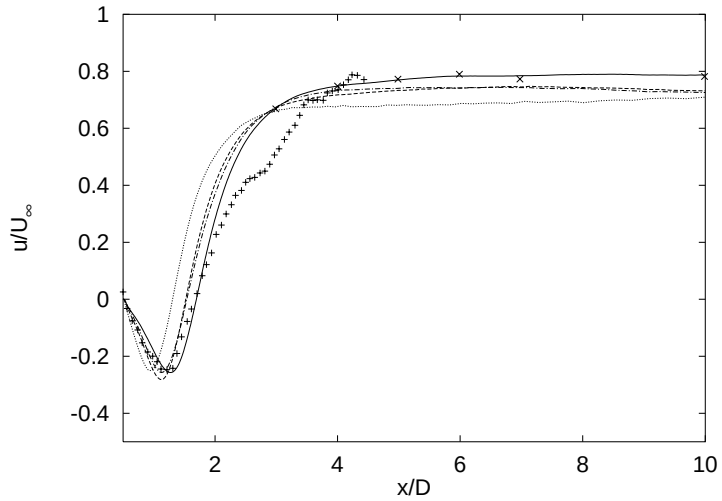

Fig. 4.10: Mean streamwise velocity along the centreline of the cylinder. Symbols: —— DNS, — · — LES1 smago, – – – – LES1 dyn, · · · · · · · LES2 smago, + experiment of Lourenco and Shih [24], x experiment of Ong and Wallace [35].

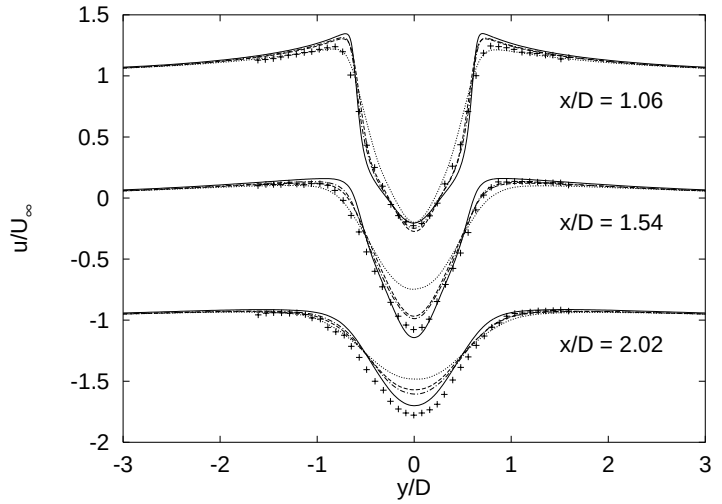

Fig. 4.11: Vertical profiles of mean streamwise velocity at $x/D = 1.06$, 1.54 and 2.02. Symbols as in Figure 4.10

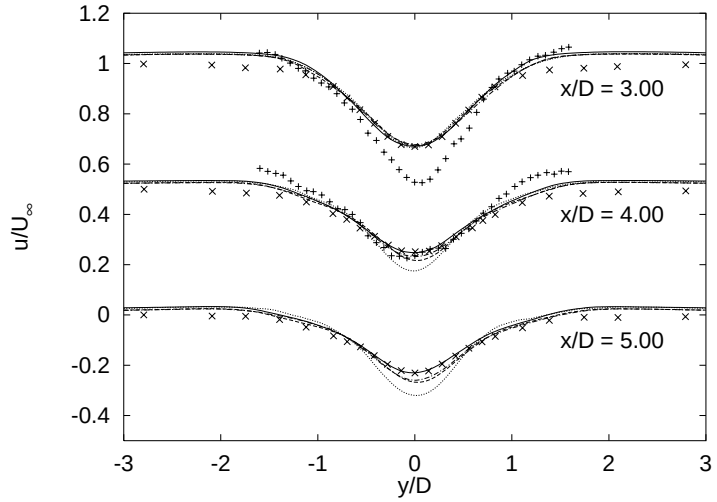

Fig. 4.12: Vertical profiles of mean streamwise velocity at $x/D = 3.00$, 4.00 and 5.00. Symbols as in Figure 4.10

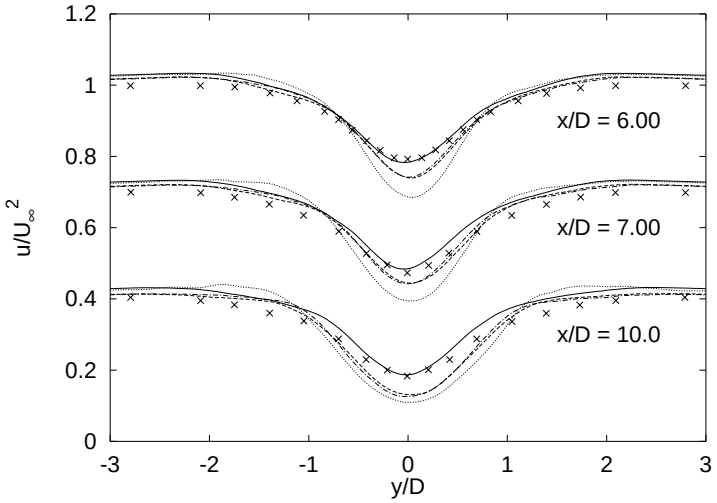

Fig. 4.13: Vertical profiles of mean streamwise velocity at $x/D = 6.00$, 7.00 and 10.0. Symbols as in Figure 4.10

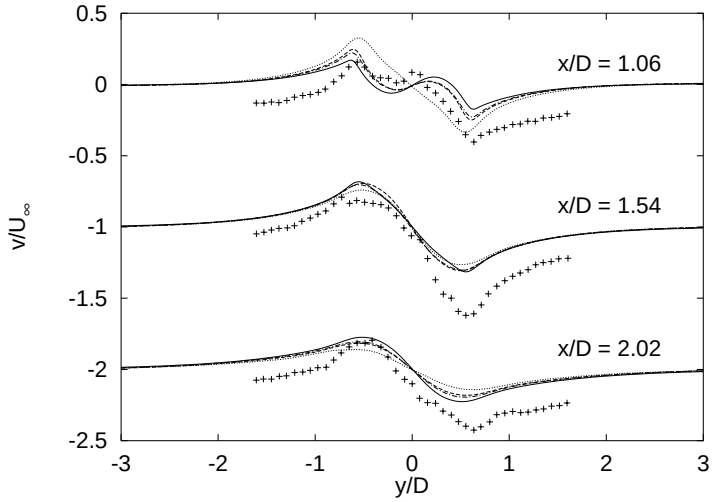

Fig. 4.14: Vertical profiles of mean vertical velocity at $x/D = 1.06$, 1.54 and 2.02. Symbols as in Figure 4.10

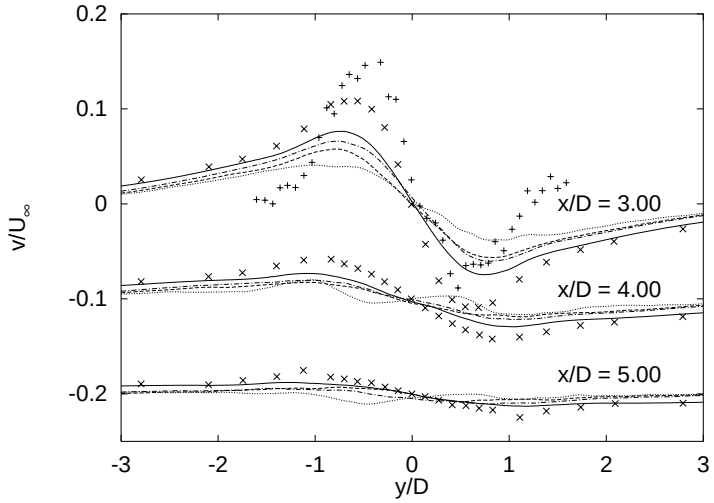

Fig. 4.15: Vertical profiles of mean vertical velocity at $x/D = 3.00$, 4.00 and 5.00. Symbols as in Figure 4.10

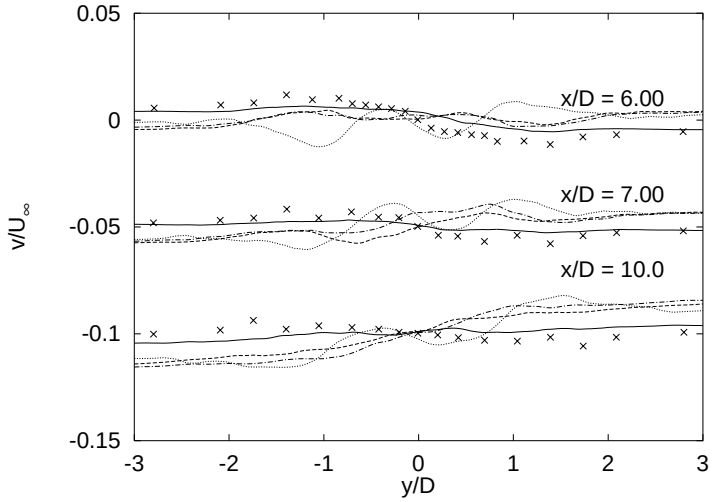

Fig. 4.16: Vertical profiles of mean vertical velocity at $x/D = 6.00$, 7.00 and 10.0. Symbols as in Figure 4.10

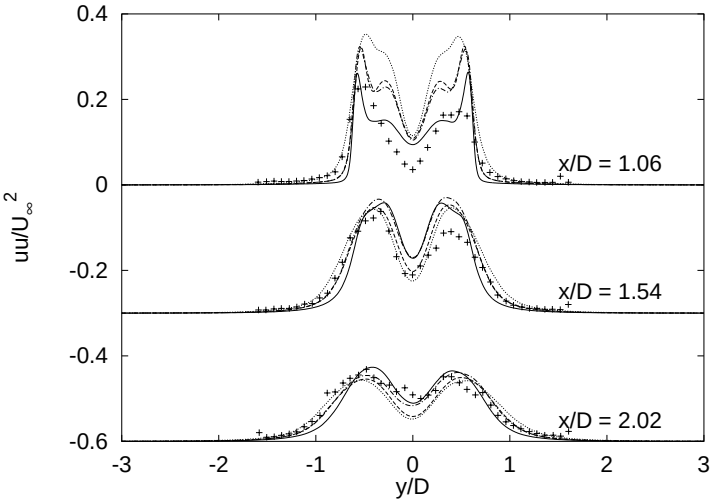

Fig. 4.17: Vertical profiles of the variance of the streamwise velocity fluctuations at $x/D = 1.06$, 1.54 and 2.02. Symbols as in Figure 4.10

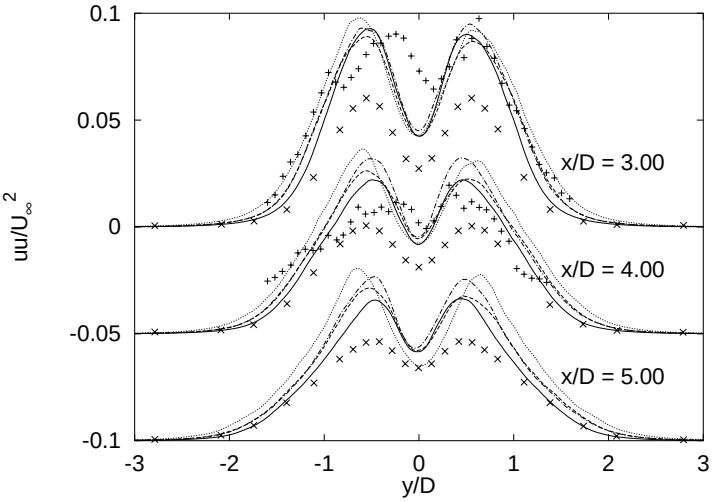

Fig. 4.18: Vertical profiles of the variance of the streamwise velocity fluctuations at $x/D = 3.00$, 4.00 and 5.00. Symbols as in Figure 4.10

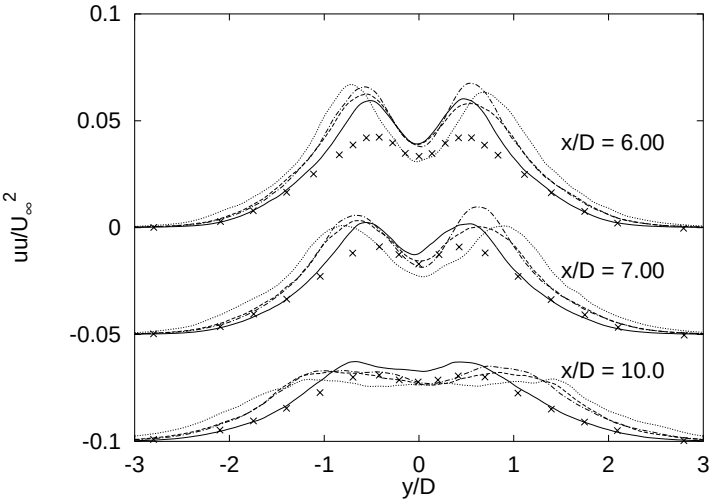

Fig. 4.19: Vertical profiles of the variance of the streamwise velocity fluctuations at $x/D = 6.00$, 7.00 and 10.0. Symbols as in Figure 4.10

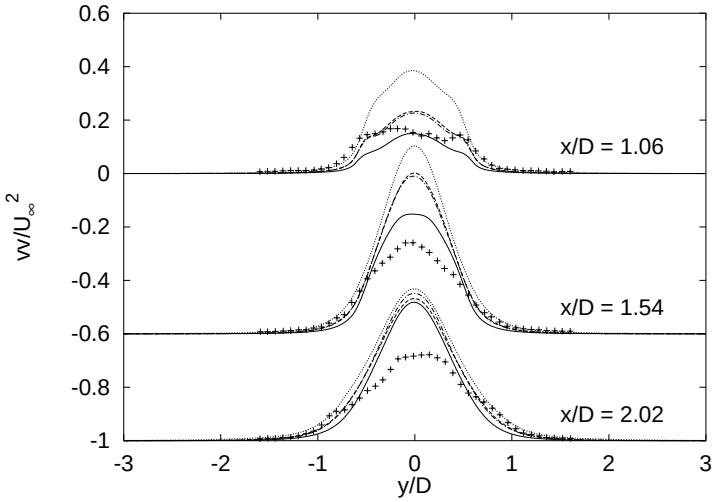

Fig. 4.20: Vertical profiles of the variance of the vertical velocity fluctuations at $x/D = 1.06$, 1.54 and 2.02. Symbols as in Figure 4.10

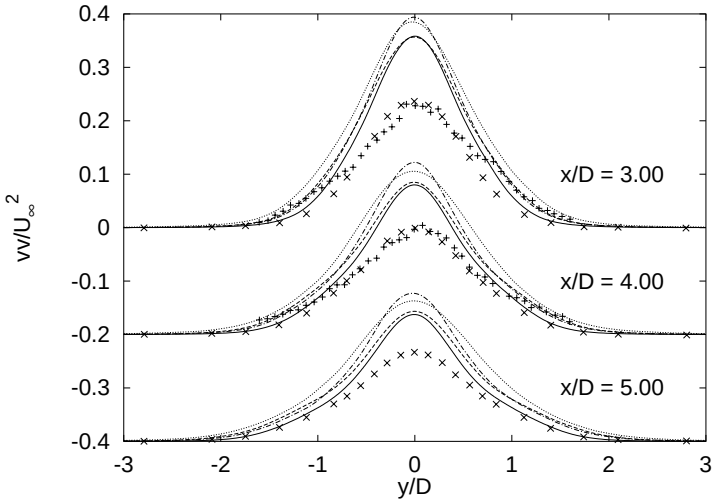

Fig. 4.21: Vertical profiles of the variance of the vertical velocity fluctuations at $x/D = 3.00$, 4.00 and 5.00. Symbols as in Figure 4.10

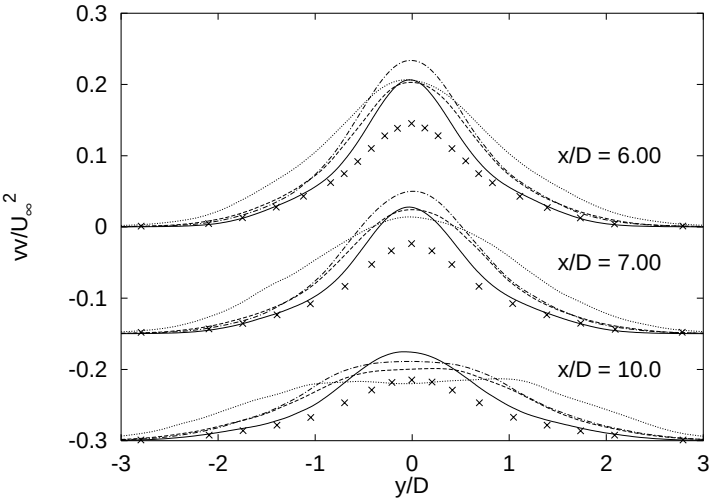

Fig. 4.22: Vertical profiles of the variance of the vertical velocity fluctuations at $x/D = 6.00$, 7.00 and 10.0. Symbols as in Figure 4.10

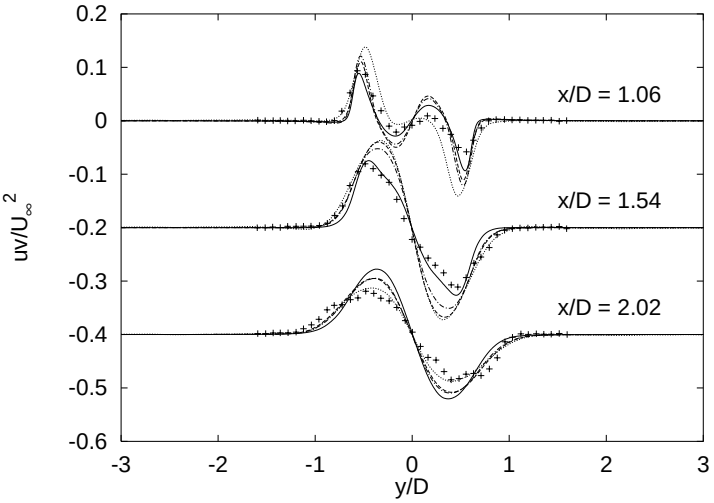

Fig. 4.23: Vertical profiles of the shear stress $\overline{uv}$ at $x/D = 1.06$, 1.54 and 2.02. Symbols as in Figure 4.10

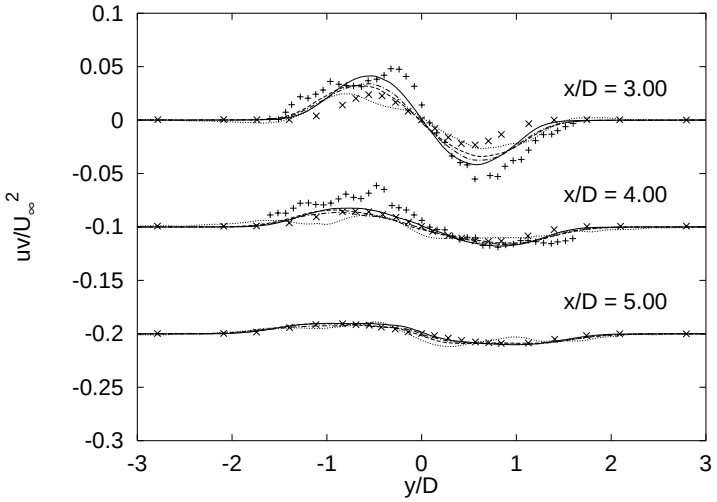

Fig. 4.24: Vertical profiles of the shear stress $\overline{uv}$ at $x/D = 3.00$, 4.00 and 5.00. Symbols as in Figure 4.10

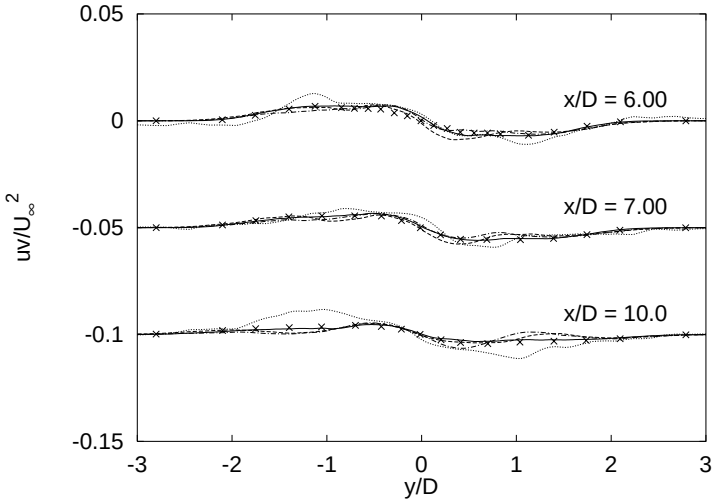

Fig. 4.25: Vertical profiles of the shear stress $\overline{uv}$ at $x/D = 6.00$, 7.00 and 10.0. Symbols as in Figure 4.10

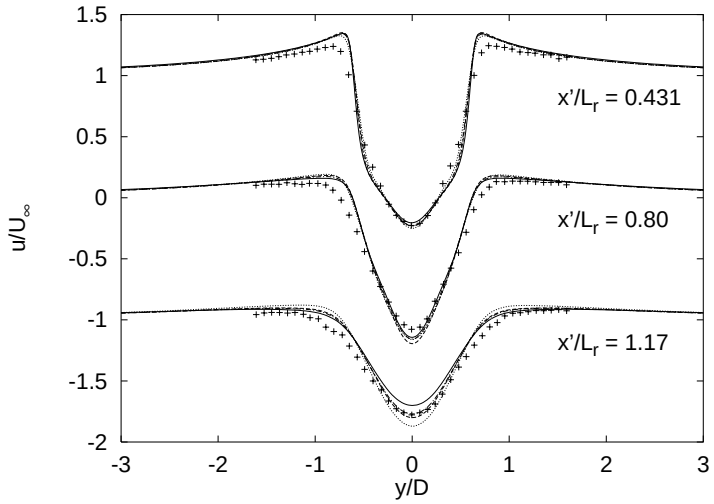

Fig. 4.26: Mean streamwise velocity profiles at three locations x'/L_r in the wake of the cylinder. The locations x/D vary from case to case according to the different recirculation lengths L_r. Symbols as in Figure 4.10

In order to demonstrate the importance of properly predicting the mean recirculation length L_r, we have plotted profiles of the mean streamwise velocity and its variance at locations which are the same when normalized with the corresponding L_r. Hence the location $x/D = 1.06$ e.g. corresponds to $x'/L_r = 0.431$ for the DNS, where x' is measured from the back of the cylinder while x starts from its center ($x' = x - D/2$). Figure 4.26 shows profiles of the mean streamwise velocity at three locations in the near wake. There is a surprising collapse of the computed results for the two first locations. While we observe the characteristic V-shape profile at $x'/L_r = 0.8$, in agreement with fully turbulent free shear layers and the experiment, such a shape does not perfectly appear in the numerical data at $x'/L_r = 0.431$. The streamwise velocity fluctuations in Figure 4.27 reflect a much better behavior compared to the experiment, when they are taken at equal locations x'/L_r.

4.4 One-dimensional power spectra

Figures 4.28 to 4.35 show one-dimensional frequency spectra at four downstream locations $x/D = 3.0$, 5.0, 7.0 and 10.0, along the centreline. Around 2500 samples were collected over a time-interval of about $tU_\infty/D = 50$ which corresponds to roughly 10 vortex shedding cycles. The frequency is normal-

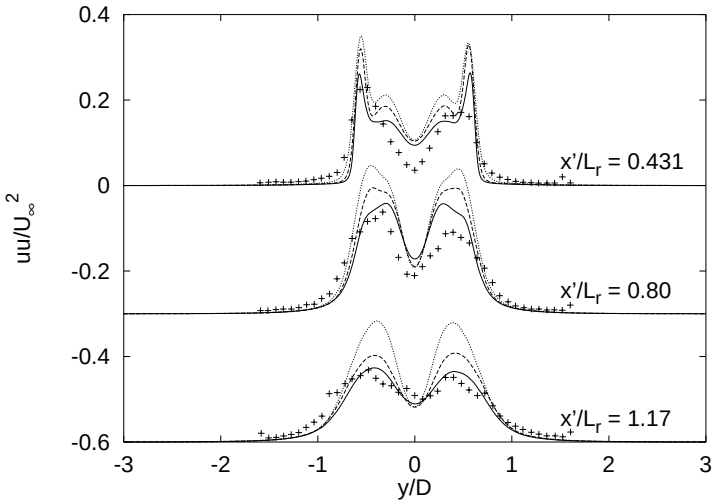

Fig. 4.27: Variance of streamwise velocity fluctuation at three locations x'/L_r in the wake of the cylinder. The locations x/D vary from case to case according to the different recirculation lengths L_r. Symbols as in Figure 4.10

ized with the Strouhal shedding frequency. This frequency is very pronounced and produces nice peaks in all the computations for the vertical velocity fluctuations and at twice this frequency for the streamwise velocity fluctuations. The vertical velocity fluctuations also exhibit a second peak like the experiment which is the higher harmonic of the Strouhal frequency. The LES also predicts an inertial range, but over a less extended frequency range as the DNS, due to the coarser grids used, especially in LES2 smago. LES1 dyn and LES1 smago provide practically identical results.

1D wavenumber spectra were computed in the homogeneous y-direction on the centreline at $x/D = 5$. In Figure 4.36, all the LES predict the energy content of the scales up to almost their respective cutoff wavenumber, in surprisingly good agreement with the DNS.

4.5 *U-shape vs V-shape of mean streamwise velocity profile in the near wake*

It has been discussed by Kravchenko and Moin [20] that the difference between a U-shape and a V-shape of the mean streamwise velocity profile in the near wake is mainly due to the shear layer dynamics which affect this region.

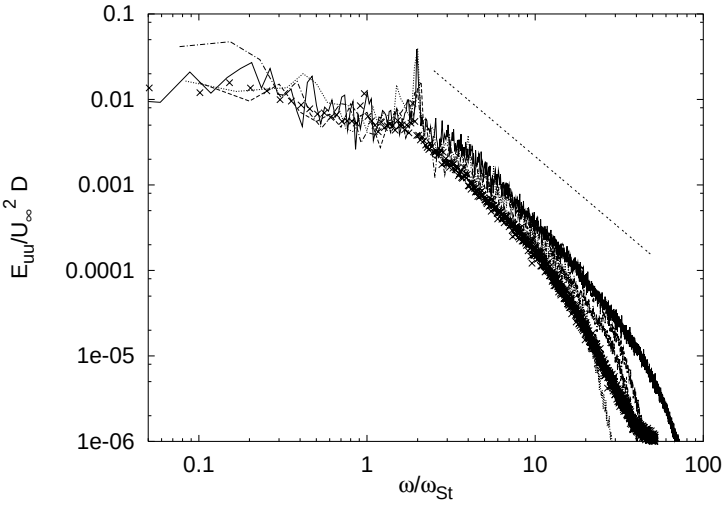

Fig. 4.28: Frequency spectra of the streamwise velocity fluctuations at $x/D = 3.00$. Symbols: —— DNS, — · — LES1 smago, – – – – LES1 dyn, ····· LES2 smago, x experiment of Ong and Wallace [35].

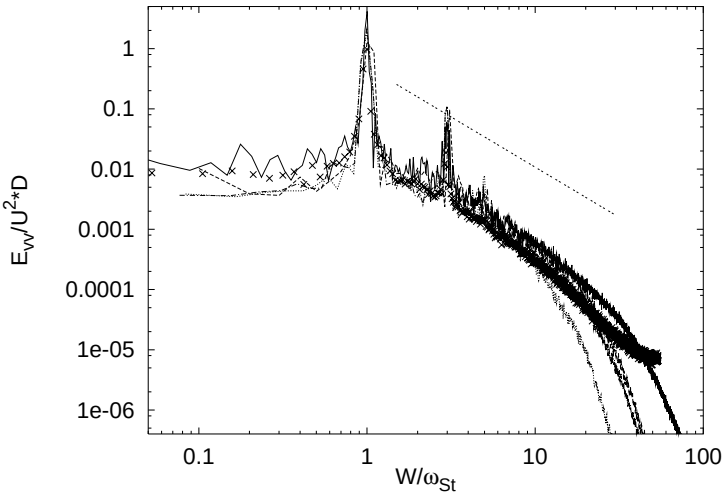

Fig. 4.29: Frequency spectra of the vertical velocity fluctuations at $x/D = 3.00$. Symbols as in Figure 4.28

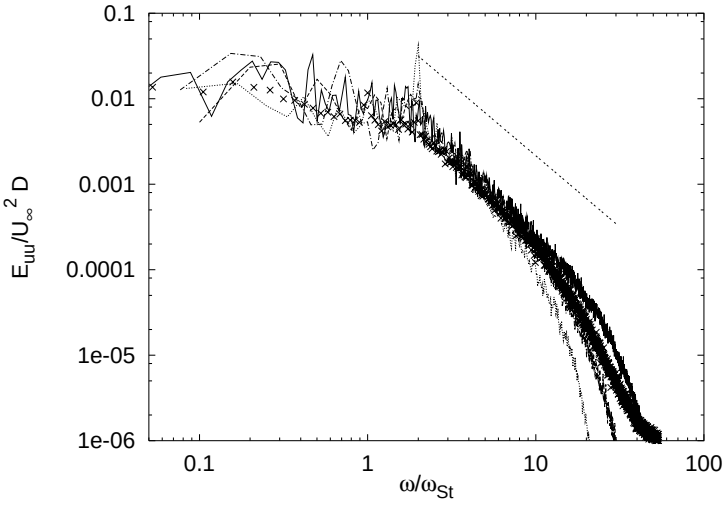

Fig. 4.30: Frequency spectra of the streamwise velocity fluctuations at $x/D = 5.00$. Symbols as in Figure 4.28

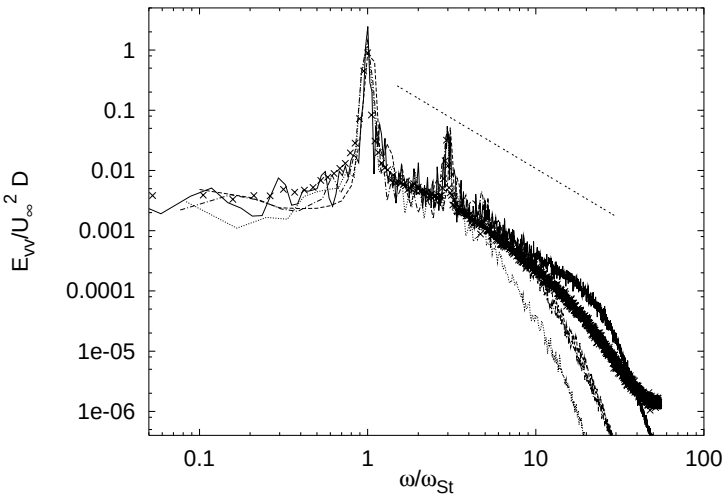

Fig. 4.31: Frequency spectra of the vertical velocity fluctuations at $x/D = 5.00$. Symbols as in Figure 4.28

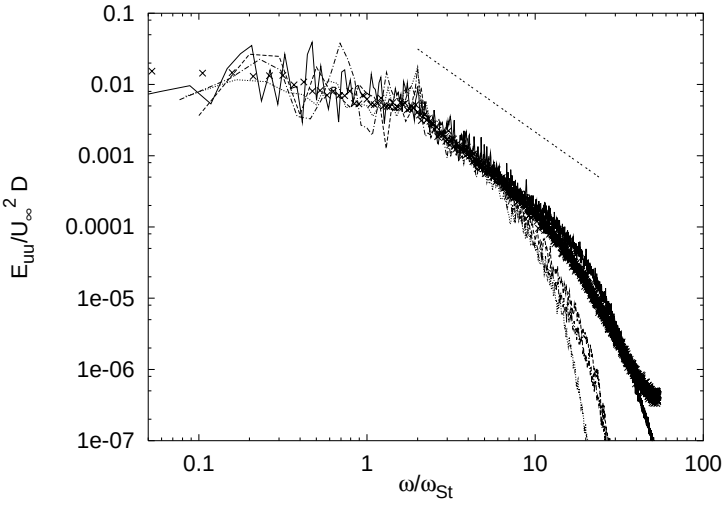

Fig. 4.32: Frequency spectra of the streamwise velocity fluctuations at $x/D = 7.00$. Symbols as in Figure 4.28

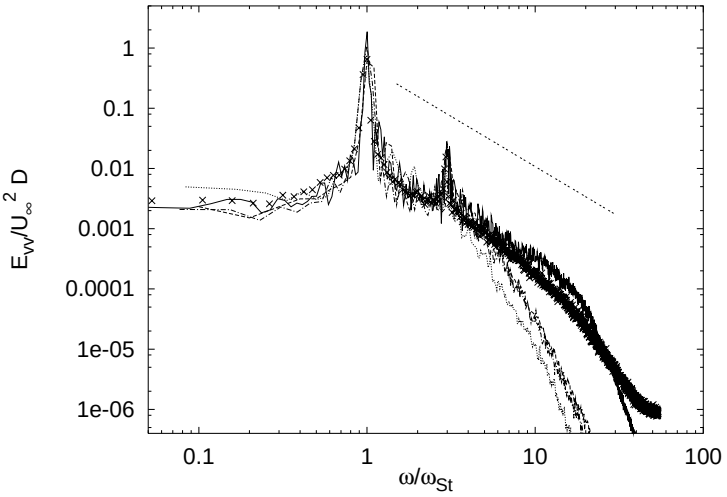

Fig. 4.33: Frequency spectra of the vertical velocity fluctuations at $x/D = 7.00$. Symbols as in Figure 4.28

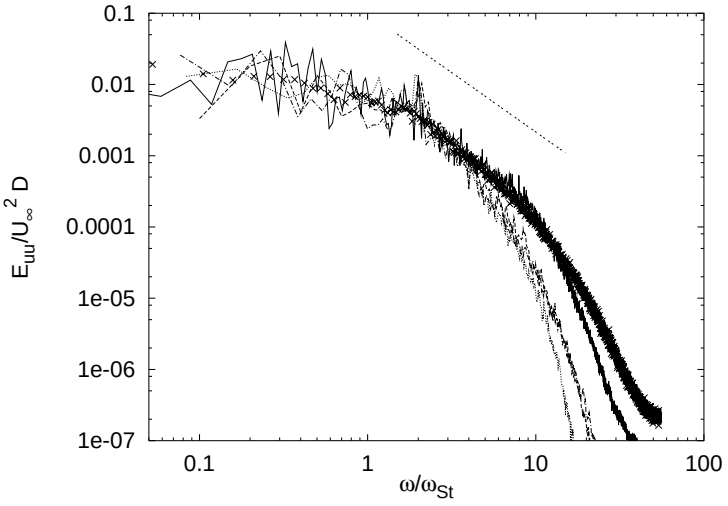

Fig. 4.34: Frequency spectra of the streamwise velocity fluctuations at $x/D = 10.0$. Symbols as in Figure 4.28

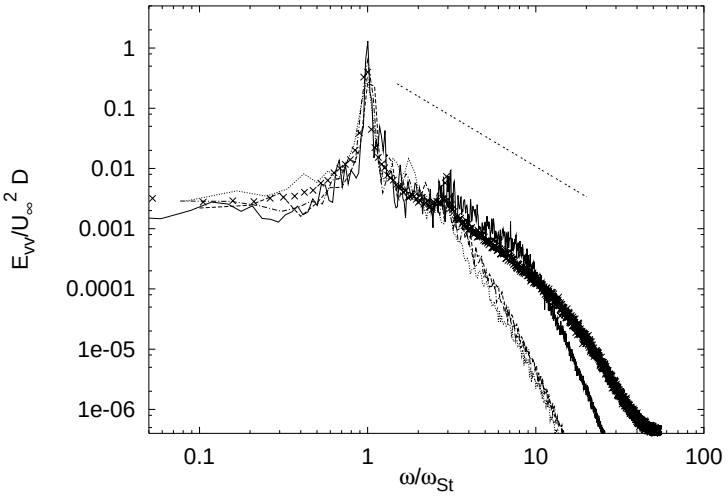

Fig. 4.35: Frequency spectra of the vertical velocity fluctuations at $x/D = 10.0$. Symbols as in Figure 4.28

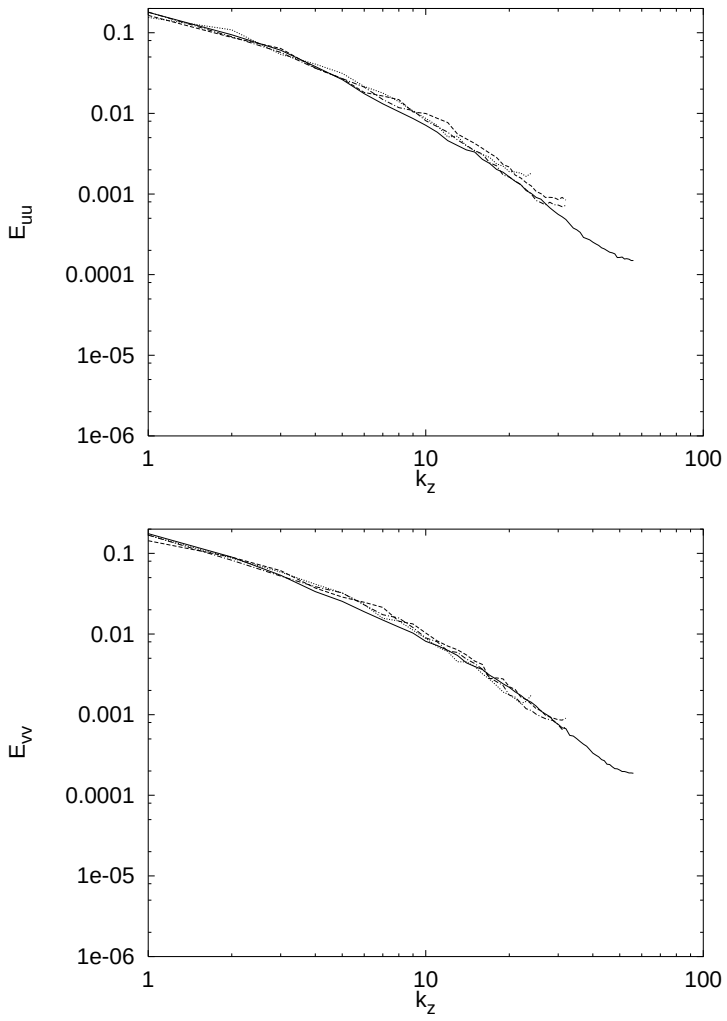

Fig. 4.36: 1D wavenumber spectra of the streamwise and vertical velocity fluctuations at $x/D = 5.00$, top and bottom respectively. Symbols: —— DNS, — · — LES1 smago, – – – – LES1 dyn, · · · · · · · LES2 smago

Shear layers are very sensitive to free-stream turbulence, to oscillations of the cylinder, acoustic forcing and aspect ratio for example. Any of these parameters can affect the recirculation bubble via a modification of the transition point to turbulence in the shear layer. The wide range of critical Reynolds numbers for the shear layer instability (350 to 3000 [37]) may reflect how the different experiments were affected by the aforementioned phenomena.

In a numerical experiment, the possibility to influence the shear layer dynamics comes through the spanwise domain size chosen, the boundary conditions enforced, the numerical errors inherent to the schemes used, the underlying grid and the sgs model. Kravchenko et al. [20] argued that the experiment of Lourenco and Shih [24] might have been contaminated by external disturbances which led to premature transition of the shear layers and thus to a shorter recirculation bubble. To demonstrate this point, they computed a case with insufficient radial and circumferential resolution and obtained results closer to the experiment. The numerical perturbations introduced by the use of a coarse grid were sufficient to trigger an earlier transition of the shear layers. In the spectral investigations of Ma et al. [26], a U-shape profile was obtained in a computation using a spanwise box size of πD, like most previous authors, while a V-shape profile was obtained for a box size of $2\pi D$. They then concluded that the U-shape profile observed in the numerical experiments resulted from too small a spanwise length or from the use of a high dissipation sgs model. This is obviously not generally true for all the numerical simulations since in our DNS and LES, V-shape profiles were obtained in conjunction with high values of the variance of the streamwise velocity fluctuations. Our computations had a spanwise domain size of πD.

In the initial phase of our DNS computation, statistical sampling was started after about $tU_\infty/D = 75$, a time at which the flow, started from a uniform velocity in the whole domain, had established a stable vortex shedding cycle and was turbulent in the wake as judged from visual inspection of the flow field. Statistics were then gathered for about $tU_\infty/D = 50$ or roughly 10 vortex shedding cycles. In Figures 4.37 to 4.39 we compare the statistics obtained after this short period of time to the one presented earlier which gathered statistics for about $tU_\infty/D = 300$. The results of Kravchenko et al. [21] are also included for comparison. They correspond to approximately 7 shedding cycles. Figure 4.37 shows the mean streamwise velocity along the centreline. We note that for the computation with the smaller averaging period, the recirculation length is greater than the one for the long period with fully converged statistics. We match fairly well the profiles obtained by Kravchenko [21], although the recirculation bubble is slightly larger in our case. The larger recirculation length is responsible for the more pronounced

U-shape observed in Figure 4.38 in the case of short statistical averaging period, while the converged statistics show more a V-shape type of profile. The data of Kravchenko [21] lie in between. In Figure 4.39, the variance of the streamwise velocity fluctuations show typical low values associated with late transition in the short averaging period case and in the data of Kravchenko [21], while the long averaging period case shows high values achieved in earlier transition of the shear layers.

We suspect that in addition to the previously mentioned possible explanations for the U-shape and V-shape velocity profiles obtained by different authors there might be an additional one. It seems from our data that the establishment of a stable statistical state for the cylinder flow at $Re = 3900$ can take a considerable amount of time. This means that care should be taken when performing a numerical experiment so that a sufficient sampling time is used and that the statistics are fully converged in the end. Prasad at al. [37] presented time traces of the velocity in the detached shear layer behind a cylinder at $Re = 4000$. They noted intermittency in the time traces. They conjectured that the intermittency observed was caused by the random displacement upstream and downstream of the region of instability of the shear layer. In [37], at $x/D = 1$, strong periods of intermittency in which the variations of the velocity are much larger than the ones caused at the Strouhal frequency, appear quasi-periodically. Their duration is of the order of 10 shedding cycles. The period of time between two consecutive occurences is also of the order of 10 shedding cycles. In order to include a few of these occurences in a statistical sampling, a period of time of about 50 vortex sheddings seems necessary in accordance with the findings presented in Prasad et al. [37].

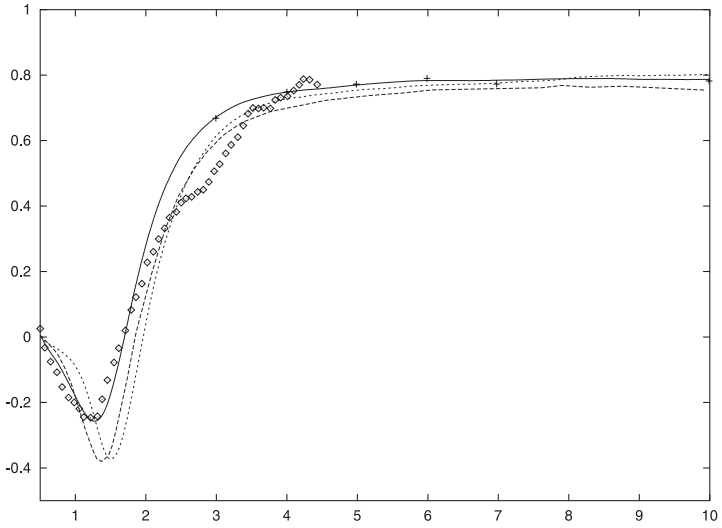

Fig. 4.37: Mean streamwise velocity along the centreline. Solid line : DNS after a sampling period of $tU_\infty/D = 300$, short dash: DNS after a sampling period of $tU_\infty/D = 50$, long dash: Kravchenko et al. [20]

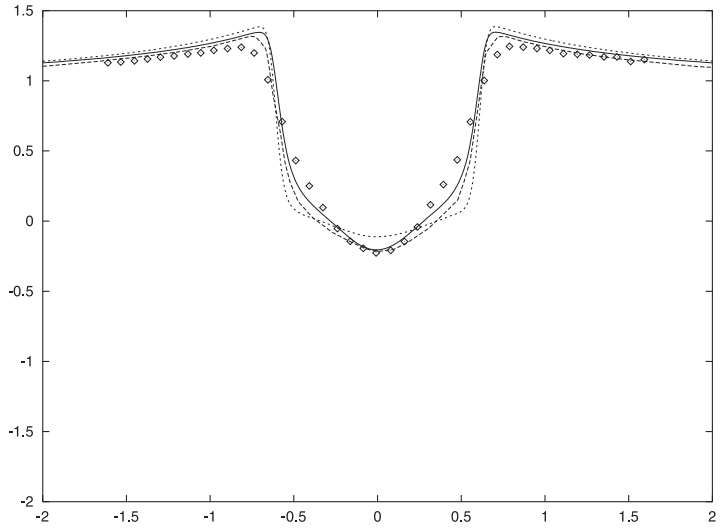

Fig. 4.38: Mean streamwise velocity at $x/D = 1.06$. Solid line : DNS after a sampling period of $tU_\infty/D = 300$, short dash: DNS after a sampling period of $tU_\infty/D = 50$, long dash: Kravchenko et al. [20]

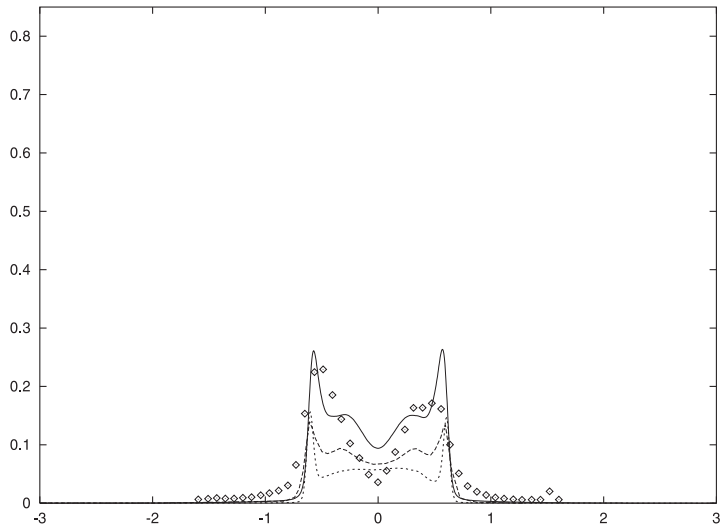

Fig. 4.39: Variance of streamwise velocity fluctuations at $x/D = 1.06$. Solid line : DNS after a sampling period of $tU_\infty/D = 300$, short dash: DNS after a sampling period of $tU_\infty/D = 50$, long dash: Kravchenko et al. [20]

5. LES of the flow around a circular cylinder at Re = 140000

In this chapter, results of LES computations of the flow around a circular cylinder at $Re = 140000$ are presented and compared to the experiment of Cantwell and Coles [7] and to numerical experiments performed by other authors.

5.1 Description of the computed cases

The flow around a circular cylinder at a high subcritical number ($Re = 140000$) is computed. The effect of the grid resolution is investigated. Both the studies of Travin et al. [45] and of Breuer [5] show that grid refinement does not automatically lead to better results when compared to the experimental data. Our first two computations were performed on those grids which were used at lower Reynolds number (3900), namely the finest grid of our LES at $Re = 3900$ (LES1), and the one used for the DNS. These computations will demonstrate the effect of a severe underresolution of the boundary layer at the surface of the cylinder and of the detached shear layers. It is well known that the current limitation of applying LES to engineering problems lies in the tremendous number of grid points needed to properly resolve the thin boundary layers found at high Reynolds numbers. The recent DES published in [45] proposed to use RANS modeling for the boundary layers and LES in the separated flow regions, thus raising hope to extend flow prediction to very high Reynolds numbers. Unfortunately, the results published in [45] at $Re = 140000$ are not very convincing, with predictions of the mean recirculation length between 2 to 3 times larger than the one measured in the experiment of Cantwell and Coles [7]. Predicting accurately the recirculating flow region is of prime importance in order to grant any credibility to the computed drag and back pressure coefficients and also to any statistics in the wake. The early stage of development of DES techniques is probably responsible for such a discrepancy.

A third computation is performed on a grid which resolves the boundary layer at the surface of the cylinder and has a finer grid spacing in the spanwise direction when compared to the grids used by Breuer [5]. This computation was carried out in order to enhance the resolution study published in [5] by providing a simulation with higher spanwise resolution and smaller grid spacings in the very near wake.

5.2 Computational details

The first two grids were described in details in chapters 3 and 4. They are named hereafter LESH1 for the grid used in LES1, and LESH2 for the grid used in the DNS at $Re = 3900$.

The computational details of LESH3 are the following: the computational domain is 18 diameters D long in the streamwise x-direction, with the center of the cylinder being $3D$ downstream of the inflow plane. In the normal y-direction, the domain size is $10D$. The spanwise extent of the domain was chosen to be $L_z = 1D$. The boundary conditions prescribed in the present simulations are a uniform, unperturbed inflow velocity and periodic velocity components in the normal and spanwise directions. A zero-gradient outflow condition holds at $x = 15D$. The total number of cells N_x, N_y, N_z in (x,y,z)-directions is 816x656x128. In the attached boundary layer along the cylinder, a minimum grid spacing of $0.00133D$ was used to ensure a proper resolution. In the square DxD which contains the cylinder 440x406 cells were used in the streamwise and the normal directions, respectively. The time step was set to $\Delta t U_\infty / D = 0.0003$ which ensured that the maximum Courant number is about 0.25.

After an initial transient period of time of about $TU_\infty/D = 75$, statistics were gathered for about $\Delta T U_\infty / D = 200$. The spanwise direction was used to enhance our statistical sampling. The Smagorinsky SGS model with $C_s = 0.1$ and no wall damping was applied in all our computations.

All the simulations were performed on the Hitachi SR8000-F1 located at the LRZ in Munich. The code MGLET had to be adapted to the new architecture of the computer. The SR8000-F1 introduces a new intermediate level of parallelism to the fine and coarse levels implemented for architectures like the Fujitsu VPP 700 for example (see Chapter 3). Each node of the SR8000-F1 is composed of 9 processors which share memory. 8 are available for the executable code and one is for internal administrative tasks. At the intermediate level of optimization, the recursive references of variables are removed from

one of the code's loops. The best performance is achieved when the most inner loops are vectorized and the most outer loops are divided among the 8 intra-node processors. The most time-consuming tasks in an incompressible Navier-Stokes solver are the time advancement of the momentum equations and the solution of the Poisson equation for the pressure. The explicit nature of our time stepping algorithm removes all recursion of the variables within the loops. The optimization is thus efficient and easily implemented. In the case of our Poisson solver, recursive references were removed at the most outer loop by the use of a red-black algorithm. Two loop levels now have red-black properties (the inner one is for vectorization) in the Poisson solver. This has an effect on the convergence rate of the pressure variable which was small and without negative consequences in the simulations.

For case LESH3, as a typical example, we use 16 nodes of the computer. Domain decomposition is applied among the different nodes. A total mean performance of about 32 Gflops, or 2 Gflops per node, is achieved. It takes roughly 5 seconds to make one time step. Around 20 GBytes of memory in total are necessary, a level much lower than the 128 GBytes available. The difference could be used to perform more detailed statistical analysis of turbulent flows for example.

920000 time steps were needed in order to perform the entire simulation LESH3 ($T = 275D/U_\infty$). A total number of about 163000 CPU hours, all processors combined, or 53 computing days in wall clock time were necessary.

5.3 Instantaneous flow field

Figure 5.1 highlights the presence of the Kelvin-Helmholtz vortices in the detached shear layers. At this instant in time, they are easily identified in the regions of low pressure on the top side of the cylinder. They are also noted in Figure 5.2, which shows the crossflow velocity component in the very near wake. Near the back of the cylinder, surprisingly high values of crossflow velocity are found, of the order of U_∞. In Figure 5.3, the instantaneous spanwise velocity component is shown. Again, high values are noted in this component, also of the order of U_∞. We observe the presence of streamwise vortices both in the separated top shear layer and in the wake, illustrated by pairs of elongated regions of high spanwise velocity of opposite sign. The Kelvin-Helmholtz vortices in the detached shear layers can be also observed in Figures 5.4 to 5.6. We note that three-dimensionality of these vortices appears rapidly after separation (see Figure 5.5). The Kármán vortex street remains quasi two-dimensional downstream of the cylinder, see Figure 5.4.

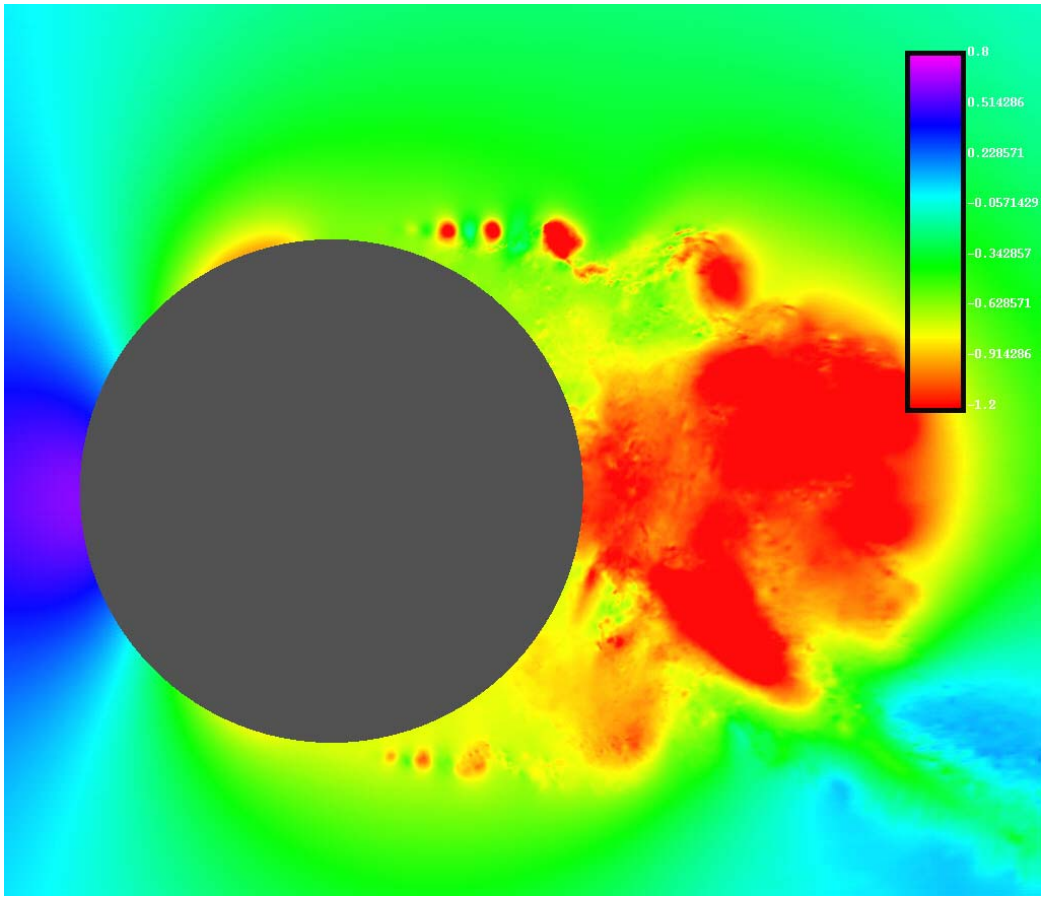

Fig. 5.1: Instantaneous pressure distribution in the very near wake.

Streamwise vortices linking the Kármán vortices are also present. They can attain a long streamwise extent, as seen in Figure 5.6.

5.4 *Integral parameters and statistics of first and second order*

Table 5.1 presents the drag and back pressure coefficients, the mean recirculation length and separation angle obtained in our simulations. We compare our results to those of [5] and [45] and also to the experiment of Cantwell and Coles [7]. The predominant feature of LESH2 is the overprediction of the mean recirculation length, a feature comparable to that of the DES of [45]. In fact, all the parameters of LESH2 lie within the incorrect range defined by DES data, with the exception of the mean separation angle which seems

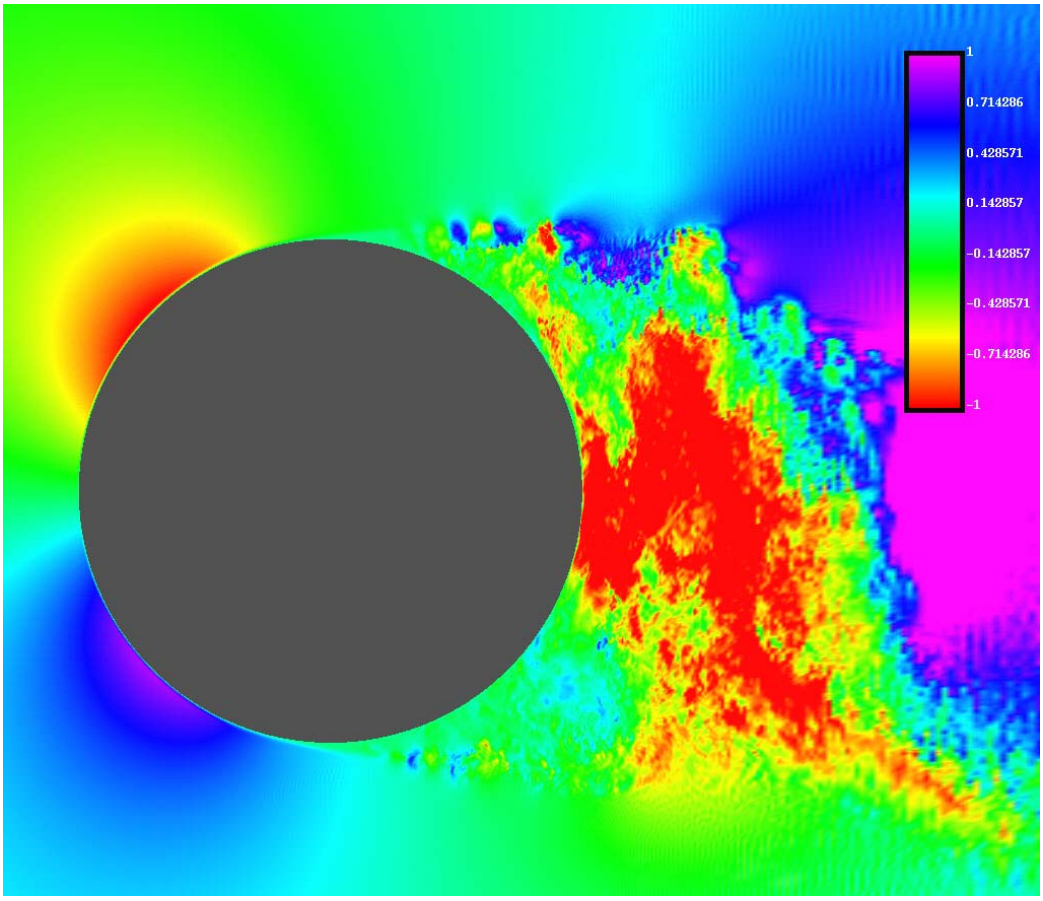

Fig. 5.2: Instantaneous crossflow velocity distribution in the very near wake.

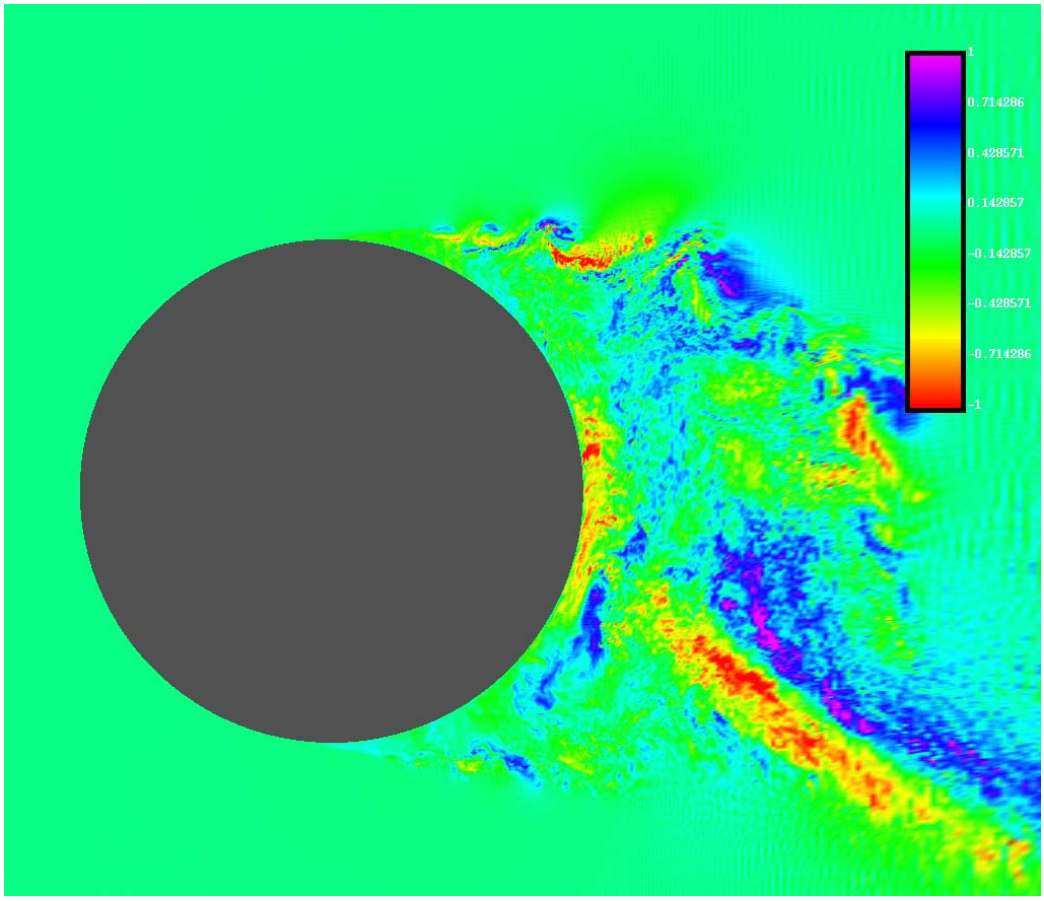

Fig. 5.3: Instantaneous spanwise velocity distribution in the very near wake.

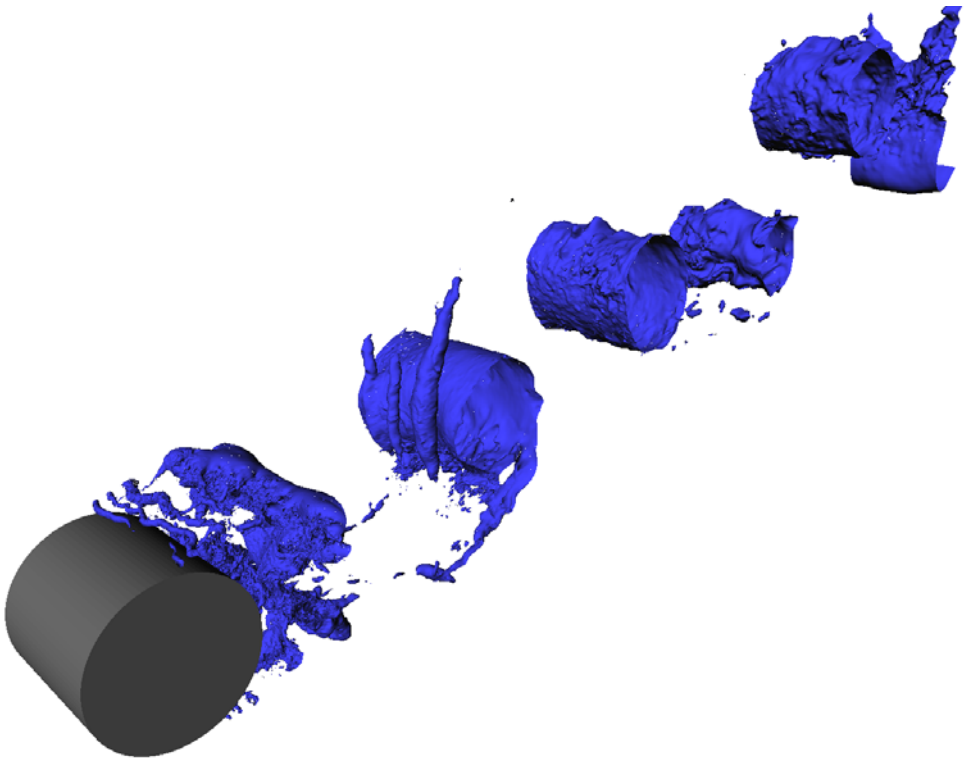

Fig. 5.4: Isosurfaces of pressure fluctuations $P'/\frac{1}{2}\rho U_\infty^2 = -0.5$, perspective view.

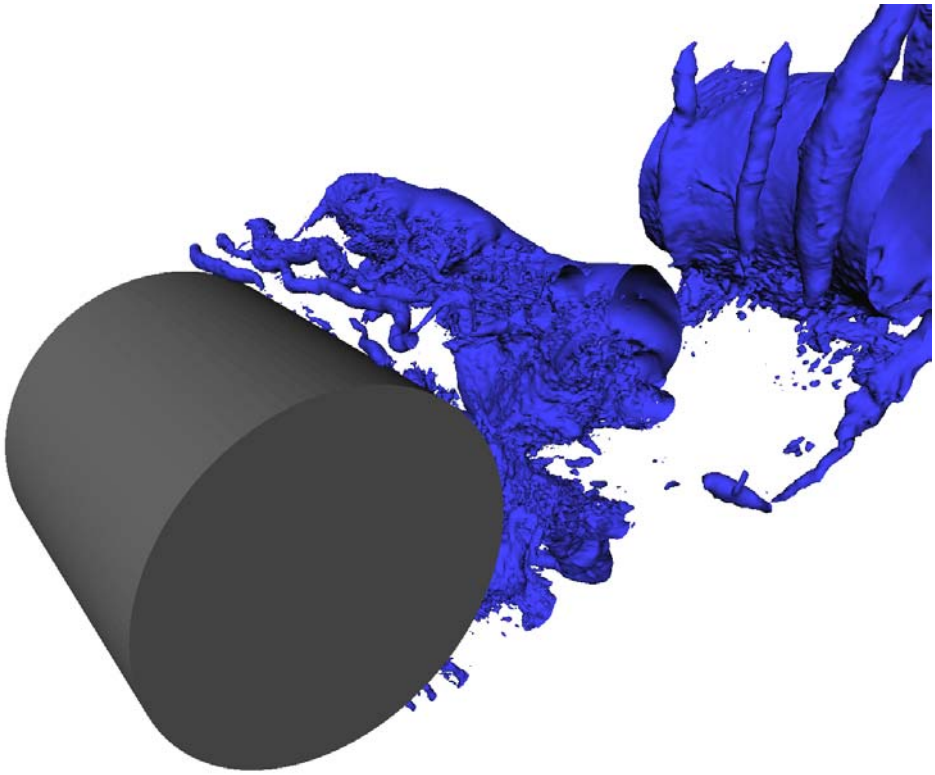

Fig. 5.5: Isosurfaces of pressure fluctuations $P'/\frac{1}{2}\rho U_\infty^2 = -0.5$, enlarged perspective view.

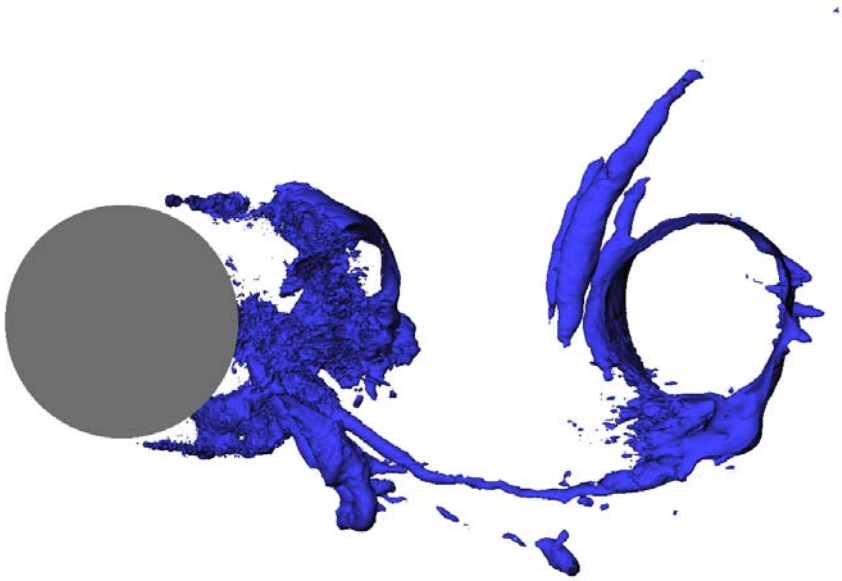

Fig. 5.6: Isosurfaces of pressure fluctuations $P'/\frac{1}{2}\rho U_\infty^2 = -0.5$, side view.

to be more precisely predicted in the DES. In [7], the mean separation angle was obtained from the inflexion point of the pressure distribution along the surface of the cylinder which in fact is different from the actual separation point. Separation occurs in reality at some distance downstream, after the boundary layer has encountered sufficient adverse pressure gradient. The fact that the coarser grid used in LESH1 provides better agreement with the experiment than the finer grid of LESH2 is most probably due to fortuitous error compensations. In the DES of [45], better agreement with the experiment was obtained with the finer grid at this Reynolds number, but at a lower Reynolds number, namely $Re = 5000$, a similar effect was observed in the sense that this time the coarser grid showed better agreement with accepted experimental values. In all cases (DES, LESH1 and LESH2), the primary vortex formation process is obviously highly deficient. We recall here that the mean recirculation length which is intimately related to the formation length of the primary Kármán vortex, depends on the transition scenario to turbulence in the separated shear layers. After the separation from the surface of the cylinder, the shear layer has a thickness which is of the same order of magnitude as that of the attached boundary layer. This means that both in DES or in underresolved LES like LESH1 and LESH2, the dynamics of the separating shear layers is not properly predicted. This is especially true in the upper subcritical range where transition to turbulence happens in the shear layers shortly after separation. The underresolution of the boundary layer and of the detached shear layer leads to a vortex formation length that is too long as noted. An erroneous prediction of L_r is sufficient to query the reliability of any other quantity computed. In contrast, LESH3 predicts the mean recirculation length very well and all the parameters lie within the range computed by [5], and are also in globally reasonable agreement with [7]. The back pressure coefficient shows a departure from the experiment of [7] by about 20%. This difference remains unexplained so far. The separation angle also differs substantially. The angle at which the flow separates has a direct impact on the back pressure coefficient, as reflected in Table 5.1. The experiments available in the literature suggest a highly non-linear relationship between the separation angle and the Reynolds number in the high subcritical regime as pointed out in [5]. This could mean that the separation point is very sensitive to the boundary conditions like for example the level of turbulence in the inflow. In the numerical computations, we have a perfectly uniform and laminar inflow, which can never be the case in the experiments. Another possible explanation is that the use of eddy-viscosity based SGS models has a stabilizing effect even in the laminar flow region, retarding separation.

Data from	C_D	C_{Pb}	Θ_{sep}	L_r/D
exp [7]	1.237	-1.21	77	0.44
DES [45]	0.87,1.08	-0.81,-1.04	77,78	1.1,1.5
LES [5]	1.22,1.45	-1.40,-1.76	92.6,96.4	0.34,0.57
LESH1	1.134	-1.22	90	0.98
LESH2	0.937	-0.980	90	1.47
LESH3	1.27	-1.45	96.7	0.44

Tab. 5.1: Mean flow parameters from DES, LES and experiments.

Figure 5.7 shows the profile of the mean tangential velocity taken along a vertical coordinate at the apex of the cylinder ($\Theta = 90$ degrees). We compare LESH1 to LESH3. The effect of boundary layer underresolution is clearly seen. The gradient of the tangential velocity is reduced, the boundary layer is too thick near the wall and the flow accelerates less as it passes near the cylinder. This probably causes the separated shear layers to be more stable, thus retarding the primary vortex formation.

The mean streamwise velocity along the centreline of the cylinder is presented in Figure 5.8. LESH1 and LESH2 strongly overpredict the recirculation length while LESH3, in Figure 5.9, shows good agreement with the experiment of [7]. The streamlines of the mean flow of LESH3 are shown in Figure 5.10. We note the symmetry of the recirculating region and conclude that sufficient statistical samples were taken. No secondary recirculation is noted. Vertical profiles of the mean streamwise velocity at $X/D = 1.0$ and $X/D = 3.0$ are shown in Figures 5.11 and 5.12, respectively. We note a good agreement with the experiment although a slight blockage effect is present in our simulation, due to the small computational domain.

The mean crossflow velocity profile at $X/D = 1.0$ is shown in Figure 5.13. Excellent agreement with the experiment is noted.

The Reynolds shear stress $\overline{u'v'}$ profile at $X/D = 1.0$ is presented in Figure 5.14. We observe higher peaks in our simulation when compared to the experiment. The width of the wake, measured by the position at which the shear stress falls close to zero, is very well captured by our simulation.

RMS values of streamwise and crossflow velocity fluctuations along the centreline of the cylinder are shown in Figures 5.15 and 5.16, respectively. We note a fair agreement of u' with the experiment while v' shows a significant departure from the measurements of [7]. Such a discrepancy was also noted by Breuer [5] in his fine grid simulations. The higher peak in v' reflects a

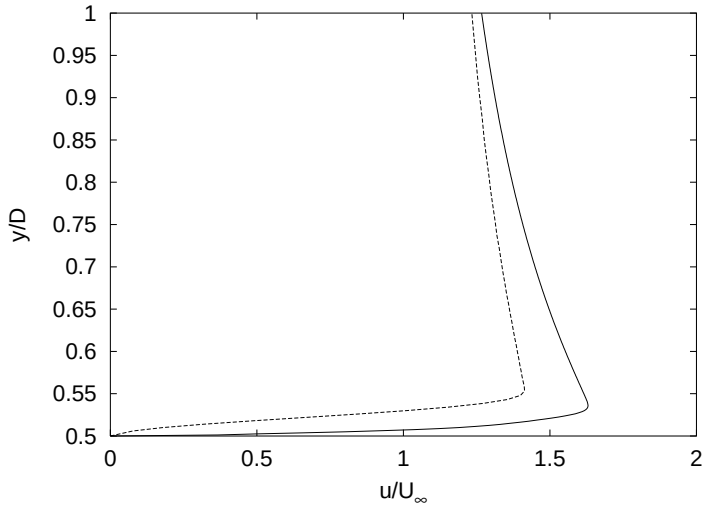

Fig. 5.7: Vertical profile of tangential velocity at $\Theta = 90$. —— LESH3, – – – – LESH1

behavior of the very near wake that is different from the experiment, causing also the lower back pressure coefficient that we obtained in our simulation. There is no clear explanation for this discrepancy, more numerical experiments are needed. We nevertheless point out that both in Breuer's and in our numerical experiments, the short spanwise length or an insufficient resolution in this direction may inhibit the transfer of energy to the third velocity component.

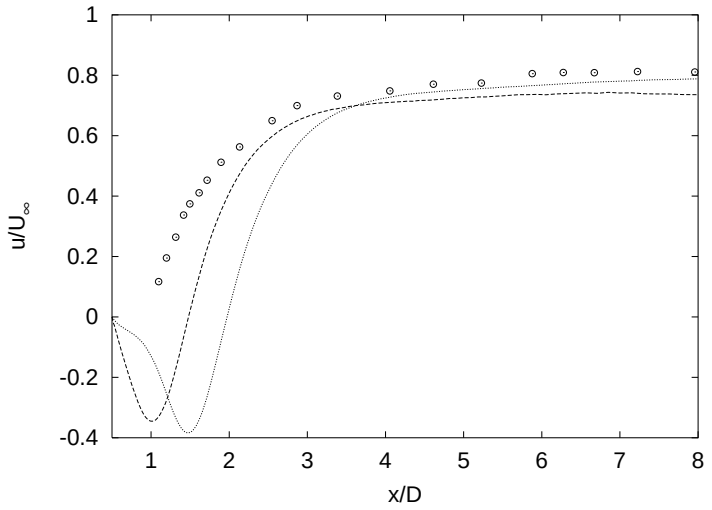

Fig. 5.8: Mean streamwise velocity along the centreline of the cylinder. – – – – LESH1, · · · · · · · LESH2, Circles Experiment [7]

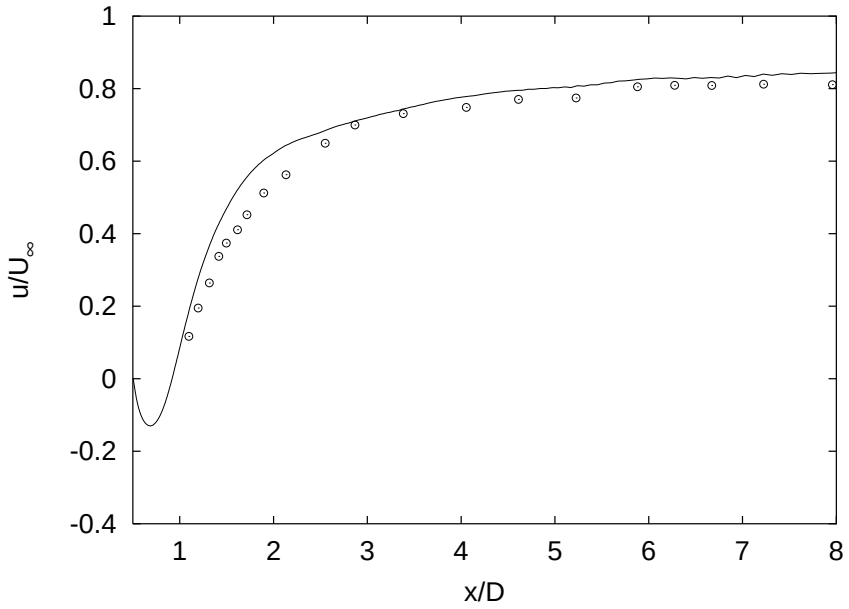

Fig. 5.9: Mean streamwise velocity along the centreline of the cylinder. —— LESH3, Circles Experiment [7]

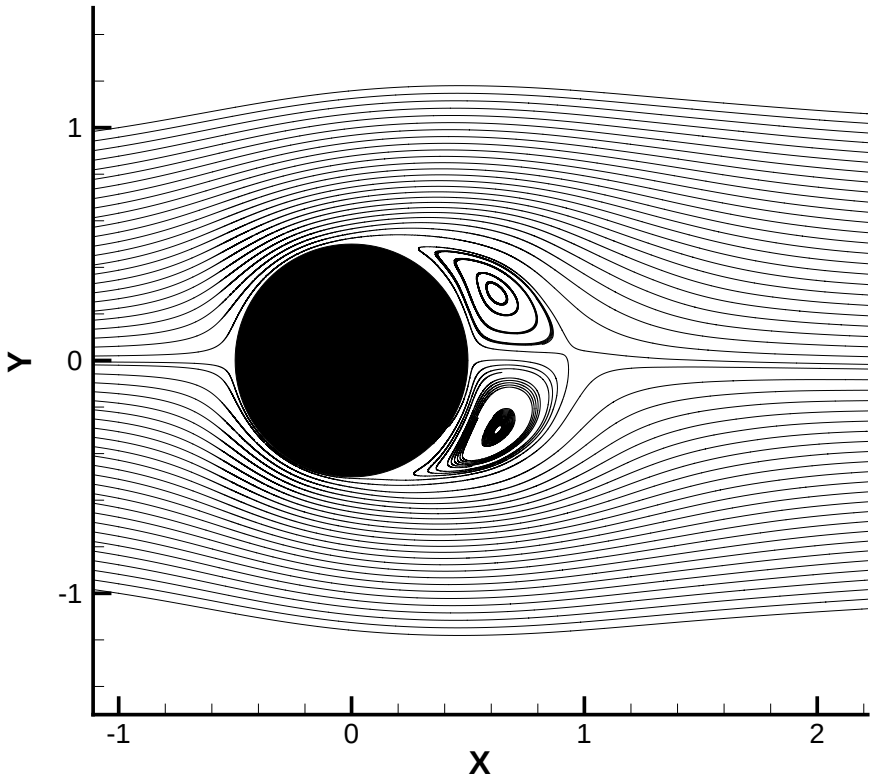

Fig. 5.10: Mean streamlines of LESH3 in the near wake.

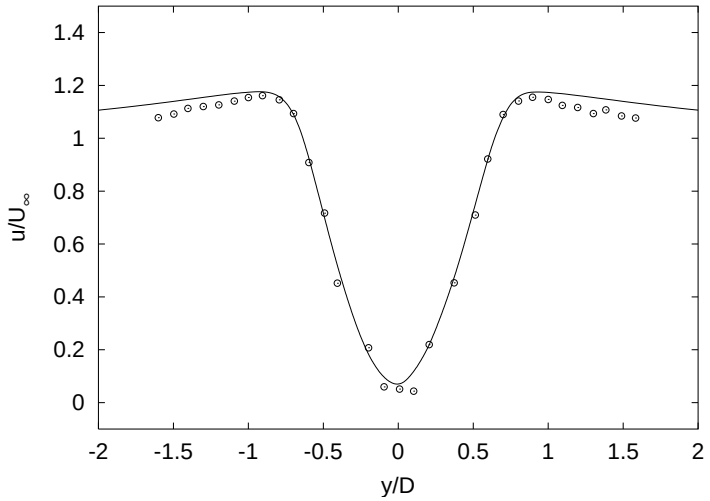

Fig. 5.11: Vertical profile of mean streamwise velocity at $x/D = 1.0$. —— LESH3, Circles Experiment [7]

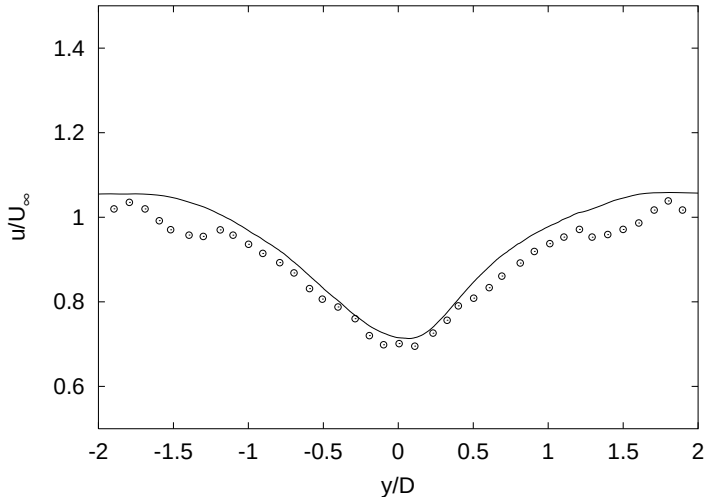

Fig. 5.12: Vertical profile of mean streamwise velocity at $x/D = 3.0$. —— LESH3, Circles Experiment [7]

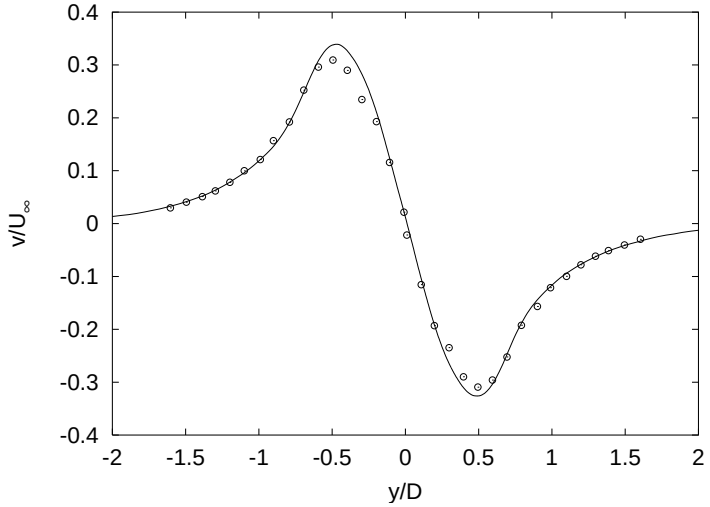

Fig. 5.13: Vertical profile of mean crossflow velocity at $x/D = 1.0$. —— LESH3, Circles Experiment [7]

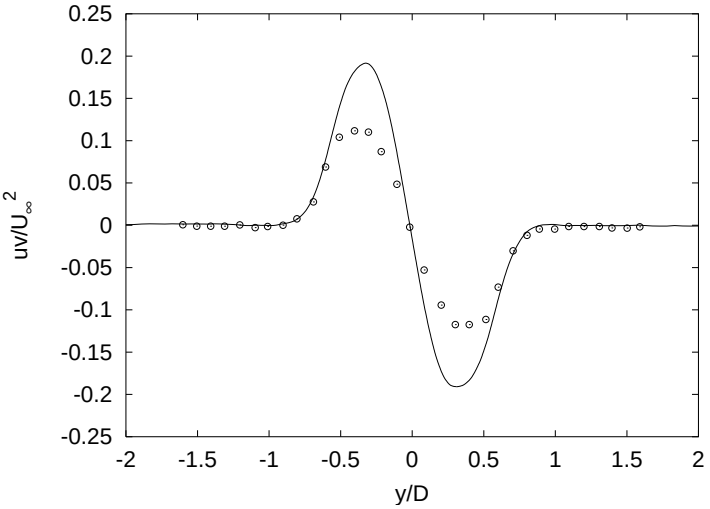

Fig. 5.14: Vertical profile of Reynolds shear stress at $x/D = 1.0$. —— LESH3, Circles Experiment [7]

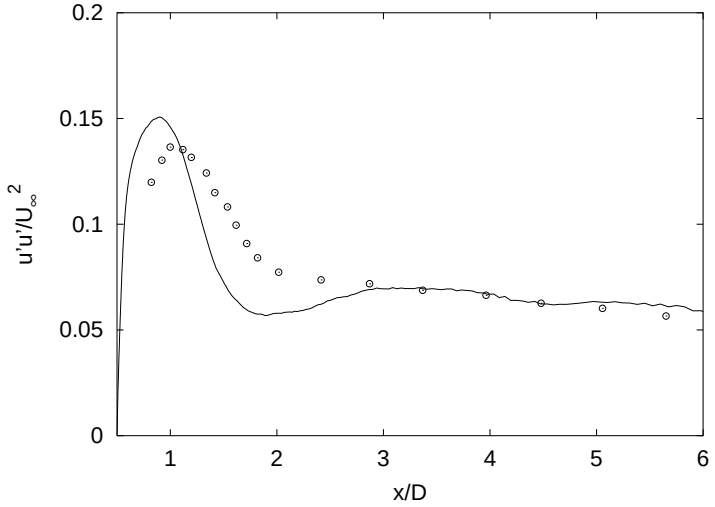

Fig. 5.15: RMS value of streamwise velocity fluctuation along the centreline of the cylinder. —— LESH3, Circles Experiment [7]

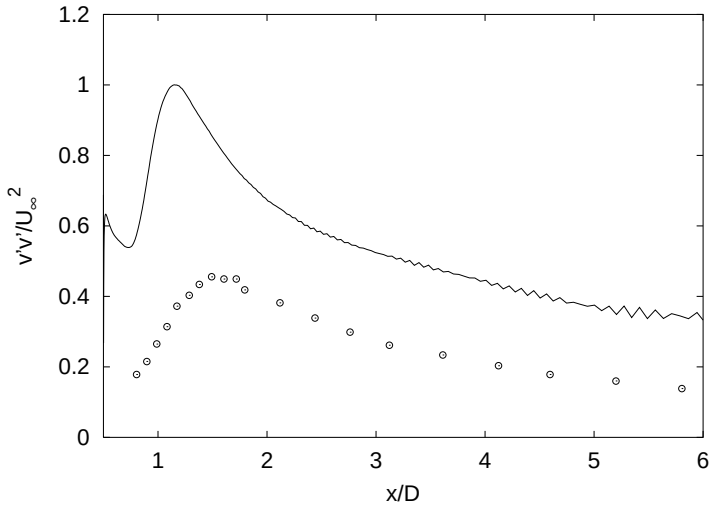

Fig. 5.16: RMS value of crossflow velocity fluctuation along the centreline of the cylinder. —— LESH3, Circles Experiment [7]

6. Conclusions and recommendations for future work

The novel immersed boundary technique developed and implemented in the code MGLET has proven to be a valuable tool for computations of flow around bodies with arbitrary shape. It provides results comparable in accuracy to those obtained with other numerical schemes employing body-fitted computational grids, given that the resolution of the cartesian grids is sufficient to resolve the relevent physical phenomena of the flow considered.

Successful DNS and LES investigations of the flow past a circular cylinder in the subcritical Reynolds number range have been conducted. They have demonstrated that the formation length of the Kármán vortex street in the very near wake intimately depends on where transition to turbulence occurs in the detached shear layers. The instability of the detached shear layers is mostly a 2D phenomenon [3] and is highly sensible to all perturbations, irrespective of whether they result from the experimental setup or from numerical contamination in the simulations. Adequate resolution of the attached boundary layer along the surface of the cylinder and of the free shear layers after separation is needed in order to predict the dynamics of the very near wake exactly. The spanwise resolution also plays a predominant role in obtaining accurate simulations of the wake. 2D simulations [2] of the flow past a circular cylinder in this range of Reynolds numbers lead to totally erroneous solutions. The initial spanwise instability of the Kármán vortex initiates to formation of self-sustained streamwise vortices that scale with the diameter of the cylinder, consistent with B-mode instability [55].

At $Re = 3900$, resolving a few occurences of these streamwise vortices, at least 3 in our case, seems sufficient to accurately represent the most important physical features involved in shear layer transition and their rolling up into the Kármán vortex street. This leads to reliable predictions of the mean recirculation region, base pressure coefficient and Strouhal number. It is, however, clear that a small spanwise extent of the computational domain, of the order of πD, does not allow for the formation of dislocations in the Kármán vortex street. Such dislocations occur between regions of the vortex street which exhibit a phase shift. They can occur naturally or may be provoked by end effects in the experiments. Dislocations are thought to play

a further important role in the transition to turbulence of the wake. We conducted a numerical experiment, not reported in the previous chapters, in which we computed a flow based on the grid LES2, but with a spanwise extent of $16\pi D$ and 768 grid points in this direction. After a period of time $T = 200D/U\infty$, although weak inhomogeneity of the Kármán vortex street in the spanwise direction was noted, no dislocations appeared. The plateau in the mean streamwise velocity reported by the experiments [24], [37] did not show up. The short duration of the simulation compared to the experimental time scale was probably not sufficient for dislocations to develop. Future work should aim at provoking dislocations artificially, or at least important phase shifts along the span of the cylinder in order to confirm whether the dislocations are partly reponsible for the appearence of the aforementioned plateau.

The LES conducted at $Re = 3900$ gave acceptable results when the grids were fine enough to resolve the important features of the flow. The effects of using different SGS models were much smaller than those obtained by grid refinement. This is in accordance with numerical experiments of previous authors.

At $Re = 140000$, the importance of an adequate resolution of the attached boundary layer along the surface of the cylinder and of the detached shear layers was demonstrated. Without a proper resolution, the near wake dynamics of the flow is highly deficient and strong overprediction of the recirculation length is observed. Without a reliable prediction of the recirculation length, serious concerns arise about the value of the results. The simulation LESH3, which properly resolved the attached boundary layer along the surface of the cylinder and the detached shear layers provided much more adequate predictions of the near wake behavior. The first order statistics were in very good agreement with the experiment of Cantwell and Coles [7]. The most notable deviations were observed in the back pressure coefficient and the peak of crossflow velocity fluctuations. Similar tendencies were also observed by Breuer [5]. Although no clear explanation for these discrepancies can be given at the moment, we conjecture that the spanwise extent and resolution will be partly responsible for the deviation from the experiment. 2D simulations typically produce a back pressure coefficient that is too low. In our case, we used a spanwise extent of only $1D$. Although Breuer [5] computed cases with larger spanwise domains, namely $2D$ and πD, he used only 64 grid points in all cases which strongly underresolves three-dimensional phenomena. More detailed studies of the effects of spanwise extent and resolution are thus needed.

We now have sufficient confidence in our immersed boundary technique in order to apply it to a more complex geometries, e.g. an airfoil undergoing heavy separation [9]. The high computational efficiency and low memory consumption of the method is demonstrated by tackling "grand challenge" problems at a reasonable computational cost. Given the resources available today, we could even envisage a DNS of the flow past a circular cylinder at a Reynolds number of about 10000. Such a simulation would take approximately 80 computing days when using 32 nodes of the Hitachi SR8000-F1 for a total time duration of about $400D/U_\infty$.

At the end of this study which naturally has left open questions, four tasks appear that would be worthwhile studying in the future. They are discussed according to their order of importance.

Order of accuracy of the numerical scheme

It is well known that the use of second order central schemes leads to a coupling between numerical errors and effects of the sgs model. It would, therefore, be desirable to further develop the immersed boundary technique to a method of fourth order accuracy and to implement it into the corresponding fourth order version of MGLET.

Boundary conditions

Both inflow and crossflow boundary conditions used in the present simulations should be modified to investigate their impact on the dynamics of the near cylinder wake. Homogeneous inflow velocities should be replaced by potential flow velocities in one step and in another, various low levels of grid turbulence should be superimposed to mimic effects that eventually were present in the experiments. Since slight blockage effects had been noted in the present data, it would be useful to try different crossflow boundary conditions instead of periodic velocity boundary conditions, e.g. zero-flux von Neumann boundary conditions or pressure boundary conditions. Of course, the best remedy to the blockage effect would be the use of a computational domain much larger where the influence of the conditions prevailing at its boundary would be accordingly reduced.

Sgs models

Considerable progress achieved in recent years in the field of modeling the 'unresolved scales', see e.g. [11], prompts the replacement of eddy-viscosity based models by new ones. Not only scale-similarity and mixed models [6], but also approximate deconvolution models are promising alternatives.

Spanwise domain size and spatial resolution

The discovery of dislocations in the Kármán vortex street by Williamson [54] is likely to explain the appearance of the plateau in the mean streamwise velocity profile at $x/D \geq 3$ of the symmetry plane. Simulations of flow around a cylinder at $Re = 3900$ with wide spanwise domain of at least $16\pi D$ would be highly desirable to confirm the experimental findings and to understand the underlying modifications of the turbulence structure. This, however, will form a grand challenge problem on present day's high-performance computers, due to the high resolution requirement in the spanwise direction. A further problem of this kind forms the $Re = 140000$ case which should be repeated with a switched-off sgs model in the complete boundary layer, with improved spatial resolution of the boundary and free shear layers and in a considerably larger spanwise domain.

Bibliography

[1] P.H. Alfredson, A.V. Johansson, and Henningson D.S. In A. Hanifi, editor, *Transition, Turbulence and Combustion Modelling, Lectures from the* 2^{nd} *Summerschool, Stockholm, 10-16 June*. Kluwer Academic Publishers, 1998.

[2] P. Beaudan and P. Moin. Numerical experiments on the flow past a circular cylinder at sub-critical Reynolds number. Report No. TF-62, Thermosciences Division, Department of Mechanical Engineering, Stanford University, 1994.

[3] M. Braza, P. Chassaing, and H. Ha Minh. Prediction of large scale transition features in the wake of a circular cylinder. *Phys. Fluids A*, 2:1461, 1990.

[4] M. Breuer. Large eddy simulation of the subcritical flow past a circular cylinder: numerical and modeling aspects. *Int. J. Numer. Meth. Fluids*, 28:1281–1302, 1998.

[5] M. Breuer. A challenging test case for large eddy simulation: high Reynolds number circular cylinder flow. *Int. J. of Heat and Fluid Flow*, 21:648–654, 2000.

[6] Chr. Brun, R. Friedrich, C.B. da Silva, and D. Metais. A new mixed model based on the velocity structure function. *In [11]*, to appear 2001.

[7] B. Cantwell and D. Coles. An experimental study of entrainment and transport in the turbulent near wake of a circular cylinder. *Journal of Fluid Mechanics*, 136:321–374, 1983.

[8] A.J. Chorin. A numerical method for solving incompressible viscous flow problems. *J. Comp. Phys.*, 2:12, 1967.

[9] G. Evans, F. Tremblay, and R. Friedrich. LES of flow around a NACA 4415 airfoil at high angle of attack. In *Proceedings of the AGSTAB*

conference, University of Stuttgart, 15-17th November 2000 (full paper to appear). Springer, 2000.

[10] E.A. Fadlun, R. Verzicco, P. Orlandi, and J. Mohd-Yusoff. Combined immersed-boundary finite-difference methods for three-dimensional complex flow simulations. *J. Comp. Phys.*, 161:35–60, 2000.

[11] R. Friedrich and W. Rodi (Eds.). LES of complex transitional and turbulent flows. In *Proceedings of the EUROMECH Coll.412*, Dordrecht. Kluwer Academic Publishers (to appear 2001).

[12] J. Fröhlich, W. Rodi, Ph. Kessler, S. Parpais, J.P. Bertoglio, and D. Laurence. Large eddy simulation of flow around circular cylinders on structured and unstructured grids. In E.H. Hirschel, editor, *Notes on Numerical Fluid Mechanics*, pages 319–338. Vieweg-Verlag, 1998.

[13] M. Germano, U. Piomelli, P. Moin, and W.H. Cabot. A dynamic subgrid-scale eddy viscosity model. *Phys. Fluids A*, 3(7):1760–1765, July 1991.

[14] R. Glowinski, T.W. Pan, and J. Periaux. Fictitious domain methods for incompressible viscous flow around moving rigid bodies. In *Proceedings of MAFELAP, Brunnel University, UK, 25-28th June 1996*, 1996.

[15] J. Gullbrand, X.S. Bai, and L. Fuchs. High order cartesian grid method for calculation of incompressible turbulent flows. *Int. J. Numer. Meth. Fluids, to appear*, 2000.

[16] C.W. Hirt, B.D. Nichols, and N.C. Romero. Sola – a numerical solution algorithm for transient fluid flows. In *Los Alamos Sci. Lab.*, Los Alamos, 1975.

[17] J.C.R. Hunt, Wray A.A., and P. Moin. Eddies, streams and convergence zones in turbulent flows. Report CTR-S88, Center for Turbulence Research, 1988.

[18] T.J. Hüttl. *Direkte Numerische Simulation turbulenter Strömungen in gekrümmten und tordierten Rohren*. PhD thesis, TU München, 1999.

[19] G.E. Karniadakis and G.S. Triantafyllou. Three-dimensional dynamics and transition to turbulence in the wake of bluff objects. *J. Fluid Mech.*, 238:1–30, 1992.

[20] A. Kravchenko and P. Moin. B-spline methods and zonal grids for numerical simulations of turbulent flows. Report No. TF-73, Flow Physics and Computation Division, Department of Mechanical Engineering, Stanford University, 1998.

[21] A.G. Kravchenko and P. Moin. Numerical studies of flow around a circular cylinder at $Re_D = 3900$. *Phys. Fluids*, 12:403–417, 2000.

[22] M. Lesieur. *Turbulence in fluids.* Mechanics of fluids and transport processes. Kluwer Academic Publishers, Dordrecht, 1987.

[23] D.K. Lilly. A proposed modification of the Germano subgrid scale closure method. *Phys. Fluids A*, 4(3):633–635, 1992.

[24] L.M. Lourenco and C. Shih. Characteristics of the plane turbulent near wake of a circular cylinder, a particle image velocimetry study. 1993, published in [2], Data taken from [20].

[25] J.L. Lumley. *Computational modeling of turbulent flows*, volume 18. Academic Press, 1978.

[26] X. Ma, G-S. Karamanos, and G.E. Karniadakis. Dynamics and low-dimensionality of a turbulent near wake. *J. Fluid Mech.*, 410:29–65, 2000.

[27] M. Manhart, G.B. Deng, T.J. Hüttl, F. Tremblay, A. Segal, R. Friedrich, J. Piquet, and P. Wesseling. The minimal turbulent flow unit as a test case for three different computer codes. In E.H. Hirschel, editor, *Vol. 66, Notes on numerical fluid mechanics*, pages 365–381. Vieweg-Verlag, Braunschweig, 1998.

[28] M. Manhart, F. Tremblay, and R. Friedrich. MGLET: a parallel code for efficient DNS and LES of complex geome tries. In *Proceedings of the Parallel CFD 2000*, Trondheim, Norway, May 22-25, 2000. NTNU.

[29] M. Manhart and H. Wengle. Large-eddy simulation of turbulent boundary layer flow over a hemisphere. In Voke P.R., L. Kleiser, and J-P. Chollet, editors, *Direct and Large-Eddy Simulation I*, pages 299–310, Dordrecht, March 27-30, 1994. ERCOFTAC, Kluwer Academic Publishers.

[30] R. Mittal and P. Moin. Suitability of upwind-biased finite difference schemes for large eddy simulation of turbulent flows. *AIAA Journal*, 35:1415, 1997.

[31] J. Mohd-Yusof. Combined immersed-boundary/b-spline methods for simulations of flow in complex geometries. In *Annual Research Briefs - 1997*, pages 317–327. Center for Turbulence Research, Stanford, 1997.

[32] P.A. Monkewitz. The absolute and convective nature of instability in two-dimensional wakes at low Reynolds numbers. *Phys. Fluids*, 31:999, 1988.

[33] C. Moulinec, M.J.B.M. Pourquié, B.J. Boersma, and F.T.M. Nieuwstadt. Diagonal cartesian method on staggered grids for a DNS in a tube bundle. In *Proceedings of the 4th Int. Workshop on Direct and Large-Eddy Simulation, Univ. of Twente, The Netherlands*, July 18-20, 2001.

[34] C. Norberg. Pressure forces on a circular cylinder in cross flow. In H. Eckelmann, J.M.R. Graham, P. Huerre, and P.A. Monkewitz, editors, *Proceedings of IUTAM Symposium on Bluff-Body Wakes, Dynamics and Instabilities*, pages 275–278, Berlin, 1993. IUTAM-Symposium, Göttingen, Germany, September 7-11, 1992, Springer-Verlag.

[35] J. Ong, L. & Wallace. The velocity field of the turbulent very near wake of a circular cylinder. *Experiments in Fluids*, 20:441–453, 1996.

[36] A.E. Perry, M.S. Chong, and T.T. Lim. The vortex-shedding process behind two-dimensional bluff bodies. *J. Fluid Mech.*, 116:77–90, 1982.

[37] D. Prasad and C.H.K Williamson. The instability of the shear layer separating from a bluff body. *J. Fluid Mech.*, 333:375–402, 1997.

[38] W.H. Press, S.A. Teukolsky, W.T. Vetterling, and B.P. Flannery. *Numerical Recipes*. Cambridge University Press, 1992.

[39] P. Sagaut. In *Large eddy simulation for incompressible flows*. Springer, Berlin, 2001.

[40] M. Schäfer and S. Turek. Benchmark computations of laminar flow around a cylinder. In E.H. Hirschel, editor, *Notes on Numerical Fluid Mechanics*, pages 547–566. Vieweg-Verlag, 1996.

[41] G. Schewe. Sensitivity of transition phenomena to small perturbations in the flow around a circular cylinder. *J. Fluid Mech.*, 172:33–46, 1986.

[42] J. Smagorinsky. General circulation experiments with the primitive equations. *Monthly Weather Rev.*, 91:99–164, 1963.

[43] P.R. Spalart. Strategies for turbulence modelling and simulations. In W. Rodi and D. Laurence, editors, *Engineering Turbulence Modelling and Experiment 4*, pages 3–17, Amsterdam, 1999. Elsevier Science Publishers.

[44] M. Thompson, M. Hourigan, and J. Sheridan. Three-dimensional instabilities in the wake of circular cylinder. *Exper. Thermal Fluid Sci.*, 12(2):190–196, 1996.

[45] A. Travin, M. Shur, M. Strelets, and P. Spalart. Detached-eddy simulations past a circular cylinder. *Flow, Turbulence and Combustion*, 63:293–313, 1999.

[46] F. Tremblay and R. Friedrich. An algorithm to treat flows bounded by arbitrarily shaped surfaces with cartesian meshes. In *Proceedings of the AGSTAB conference, University of Stuttgart, 15-17th November 2000 (full paper to appear)*. Springer, 2000.

[47] F. Tremblay, M. Manhart, and R. Friedrich. LES of flow around a circular cylinder at a subcritical Reynolds number with cartesian grids. In *Proceedings of the EUROMECH Colloquium 412 on LES of complex transitional and turbulent flows, Munich University of Technology, 4-6th October 2000 (full paper to appear)*. Kluwer Academic, 2001.

[48] F. Tremblay, M. Manhart, and R. Friedrich. DNS of flow around a circular cylinder at a subcritical Reynolds number with cartesian grids. In *Proceedings of the 8th European Turbulence Conference, EUROMECH, Barcelona, Spain*, pages 659–662. CIMNE, 27-30th June 2000.

[49] F. Tremblay, M. Manhart, and R. Friedrich. LES of flow around a circular cylinder at a high subcritical Reynolds number with cartesian grids. In *Proceedings of the 4th Int. Workshop on Direct and Large-Eddy Simulation, Univ. of Twente, The Netherlands*, July 18-20, 2001.

[50] D.J. Tritton. *Physical fluid dynamics*. Oxford University Press, 1988.

[51] G. Wang, P.G. Choudhuri, M.A. Bhandarkar, and S.P. Wanka. Large eddy simulations of bluff body wake on parallel computers. Report of CFD Laboratory, Department of Mechanical and Industrial Engineering, University of Illinois, 1996.

[52] H. Werner. *Grobstruktursimulation der turbulenten Strömung über eine querliegende Rippe in einem Plattenkanal bei hoher Reynoldszahl*. PhD thesis, Technische Universität München, München, 1991.

[53] H. Werner and H. Wengle. Large-eddy simulation of turbulent flow over a square rib in a channel. In H.H. Fernholz and H.E. Fiedler, editors, *Advances in Turbulence*, volume 2, pages 418–423. Springer-Verlag, Berlin, 1989.

[54] C.H.K. Williamson. The natural and forced formation of spot-like vortex dislocations in the transition of a wake. *J. Fluid Mech.*, 243:393–441, 1992.

[55] C.H.K. Williamson. Vortex dynamics in the cylinder wake. *Annu. Rev. Fluid Mech.*, 28:477–539, 1996.

[56] G. Yang, D.M. Causon, and D.M. Ingram. Cartesian cut-cell method for axisymmetric separating body flows. *AIAA Journal*, 37(8):905–911, 1999.